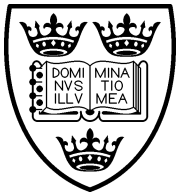
# Disorder in an exactly solvable quantum spin liquid




Adam Willans

Balliol College

University of Oxford

A thesis submitted for the degree of

*Doctor of Philosophy*

Trinity Term 2010

# Acknowledgements

This thesis would not have been possible without the patient guidance and support of my two supervisors: John Chalker at the University of Oxford and Roderich Moessner at the Max Planck Institute for the physics of complex systems, Dresden. Their ability as physicists continues to astound me and to them both I give many thanks.

There are numerous people who have made an invaluable, indirect contribution to this thesis and I thank them all: my colleagues in Oxford and Dresden; my friends and family, who keep my eyes open to a world outside of physics; and Anna, who has brought endless joy and happiness to all of my days in Oxford.

I would also like to thank the department of Theoretical physics at the University of Oxford for an EPSRC studentship and the Max Planck Institute for many long and useful visits to Dresden.

# Contents


**1 Introduction** **1**

1.1 Mott insulators and spin Hamiltonians . . . . . 2

1.2 Disorder in strongly correlated systems . . . . . 4

1.2.1 Spin-$\frac{1}{2}$ Heisenberg antiferromagnetic chain . . . . . 6

1.2.2 Spin-1 Heisenberg antiferromagnetic chain . . . . . 11

1.2.3 Two dimensional Heisenberg antiferromagnets . . . . . 13

1.2.4 The cuprates . . . . . 16

1.2.5 Graphene . . . . . 17

1.3 RVB, VBS and spin liquids . . . . . 21

1.4 Quantum computation . . . . . 24

**2 The model** **28**

2.1 Majorana fermions and spin Hamiltonians . . . . . 29

2.2 Exact solubility and projection . . . . . 30

2.3 Properties of the clean system . . . . . 37

2.4 Proposals for experiment . . . . . 41

2.5 Thesis outline . . . . . 43

**3 Site dilution in the gapped Phase** **44**

3.1 Flux binding . . . . . 44

3.2 Local moment formation . . . . . 49

3.3 Interaction of moments . . . . . 55

3.4 Finite density of vacancies . . . . . 60

3.4.1 Heat capacity . . . . . 64

**4 Site dilution in the Gapless Phase** **66**

4.1 Flux binding . . . . . 67

4.2 Local moment formation . . . . . 68

4.3 Magnetisation of two vacancies . . . . . 76

4.3.1 Two vacancies on opposite sublattices . . . 77
4.3.2 Two vacancies on the same sublattice . . . 80
4.3.3 Finite density of vacancies . . . 83
4.4 Finite size effects . . . 84
4.5 Summary . . . 85

**5 Disorder in exchange** **87**
5.1 Slowly varying, weak disorder . . . 87
5.2 Slowly varying, strong disorder . . . 90

**6 Summary and outlook** **91**
6.1 Summary . . . 91
6.2 Outlook . . . 92

**A Green function for the hexagonal lattice** **96**
A.1 Gapless phase . . . 96
A.2 Gapped phase . . . 99

**B Effective moment of a single vacancy in the gapless phase and flux free sector** **101**
B.1 $T = 0, \mathbf{h} = (0, 0, h), h \ll J$ . . . 101
B.2 Finite $T, \mathbf{h} = (0, 0, h), h \ll J$ . . . 102
B.2.1 Magnetisation for $z_{-1} \ll T$ . . . 103
B.2.2 Magnetisation for $T \ll z_{-1}$ . . . 104
B.3 $T = 0, \mathbf{h} = (h_x, h_y, h_z), h \ll J$ . . . 105

**C Effective moment of a single vacancy in the gapless phase and ground state flux sector** **108**
C.1 $T = 0, h = (0, 0, h), h \ll J$ . . . 108
C.2 Finite $T, h = (0, 0, h), h \ll J$ . . . 108

**D Calculation of the local density of states on a semi-infinite cylinder** **110**

**Bibliography** **112**

# List of symbols

This list of symbols does not contain those found in the introduction; rather, it lists those that feature prominently in the main text.

| | |
|---|---|
| $\alpha$ ..... | bond type $x, y$ or $z$ |
| $\alpha_{jk}$ ..... | bond type between sites $j$ and $k$ |
| $a_0$ ..... | amplitude of a vacancy zero mode $\Psi^{A(B)}(\mathbf{r})$ on a site adjacent to the vacancy |
| $a^\dagger$ $(a)$ ..... | complex fermion creation (annihilation) operator |
| $\mathbf{A}(\mathbf{r})$ ..... | two component random vector potential, $\mathbf{A}(\mathbf{r}) = (A_\mu(\mathbf{r}), A_\nu(\mathbf{r}))$ |
| $b^x, b^y, b^z, c$ ..... | Majorana operators |
| $B$ ..... | magnetic field associated with the random vector potential $\mathbf{A}(\mathbf{r})$ |
| $C$ ..... | heat capacity |
| $\mathbf{d}$ ..... | separation of the unit cells occupied by two vacancies |
| $\mathbf{d}^{\alpha\beta}$ ..... | separation of two vacancy sites on the $\alpha$ and $\beta$ sublattices |
| $D$ ..... | $D = \prod_j D_j$ |
| $D_j$ ..... | $D_j = b_j^x b_j^y b_j^z c_j$ |
| $\Delta$ ..... | gap to matter fermion excitations |
| $\Delta_k$ ..... | exchange disorder strength |
| $\Delta_W$ ..... | gap to changing the flux sector our of the ground state |
| $\epsilon$ ..... | a positive infinitesimal |
| $\epsilon_\alpha(\mathbf{r})$ ..... | quenched exchange disorder: $J_\alpha(\mathbf{r}) = J(1 + \epsilon_\alpha(\mathbf{r}))$ |
| $\mathcal{E}(h)$ ..... | Change in ground state energy as a function of field for the Kitaev model with vacancies and a field compared to its zero field value |
| $\mathcal{E}(z, h)$ ..... | intermediary variable used in the calculation of $\mathcal{E}(h)$ |
| $E$ ..... | energy (real) |
| $E_0$ ..... | ground state energy of $H_0$: $E_0 = -J_z N$ |
| $E^\alpha(\mathbf{r})$ ..... | local bond energy $E^\alpha(\mathbf{r}) = \sigma_j^{\alpha_{jk}} \sigma_k^{\alpha_{jk}}$ |
| $\mathcal{F}(x)$ ..... | a slowly varying, logarithmic function of its argument |
| $f^\dagger$ $(f)$ ..... | complex matter fermion creation (annihilation) operators |
| $f(E)$ ..... | the Fermi function |
| $g$ ..... | g-tensor for an effective vacancy moment |
| $g(z)$ ..... | site diagonal Green function element on a site adjacent to a vacancy |
| $G_0(\mathbf{r}, \mathbf{r}')$ ..... | Green function for the undiluted hexagonal lattice $H_0$ |
| $G(h, \mathbf{r}, \mathbf{r}')$ ..... | Green function for the tight binding model associated with the Kitaev Hamiltonian with projected Zeeman energy and vacancies and in the flux free sector |

| | |
|---|---|
| $G_F(h, \mathbf{r}, \mathbf{r}')$ ..... | Green function for the tight binding model associated with the Kitaev Hamiltonian with projected Zeeman energy and vacancies and in the ground state flux sector |
| $G_F(\mathbf{r}, \mathbf{r}')$ ..... | Green function for the tight binding model associated with $H_F$ |
| $G_F^{AA}, G_F^{BB}, G_F^{BA}$. | Matrix of Green function elements evaluated between sites where vacancies will be placed, such that the model will be in the correct ground state flux sector once vacancies are introduced |
| $\mathbf{h} = (h_x, h_y, h_z)$. | magnetic field |
| $\widetilde{H}$ ..... | Kitaev Hamiltonian |
| $\widetilde{H}_0$ ..... | Kitaev Hamiltonian with $J_x = J_y = 0$ |
| $\widetilde{H}_{\text{eff}}$ ..... | effective flux Hamiltonian |
| $H_{\text{eff spin}}$ ..... | effective spin Hamiltonian describing the properties of the effective vacancy moments |
| $H_F$ ..... | Kitaev Hamiltonian with fixed bond fermion number and fluxes on one plaquette adjacent to each site where a vacancy will be placed, such that inclusion of vacancies leaves the model in the ground state flux sector |
| $H_{\hat{u}}$ ..... | Kitaev Hamiltonian in Majorana space |
| $H_u$ ..... | Kitaev Hamiltonian with fixed bond fermion number |
| $\widetilde{H}_Z$ ..... | the leading order term in the Zeeman energy projected onto the ground state flux sector |
| $\eta(j)$ ..... | variable used to introduce fluxes in the calculation of the LDOS |
| IPR ..... | inverse participation ratio |
| $j_\alpha$ ..... | $j_\alpha = J_\alpha / J_z$ for $\alpha = x, y$ |
| $J_{\alpha_{jk}}$ ..... | exchange coupling between sites $j$ and $k$ |
| $\Lambda^{\pm}(z, \mathbf{q})$ ..... | variable used in the calculation of the LDOS in the presence of fluxes |
| $L$ ..... | lattice size |
| LDOS ..... | local density of states |
| $m(h)$ ..... | vacancy magnetisation as a function of field at zero temperature |
| $m(h, T)$ ..... | vacancy magnetisation as a function of field and temperature |
| $m(E, h)$ ..... | combined vacancy magnetisation for two vacancies in the gapped sector, as a function of their interaction energy $E$ and field $h$ |
| $M$ ..... | an $N \times N$ matrix with entries $M_{jk} = J_{\alpha_{jk}} u_{jk}$ and singular value decomposition $M = USV^{\mathrm{T}}$ |
| $\mathbf{n}_1, \mathbf{n}_2$ ..... | lattice vectors |
| $N$ ..... | number of unit cells |
| $N_A$ ..... | number of vacancies on the $A$ sublattice |
| $N_B$ ..... | number of vacancies on the $B$ sublattice |
| $N_f$ ..... | matter fermion number operator |
| $N_\chi$ ..... | bond fermion number operator |

| | |
|---|---|
| $\xi$ | length scale in the gapped phase |
| $\mathcal{P}$ | projection operator onto physical states |
| $\mathcal{P}'$ | $\mathcal{P} = \mathcal{P}'(1+D)/2$ |
| $\phi(\mathbf{r})$ | solution to a Dirac Hamiltonian with a random vector potential |
| $\|\Phi\rangle$ | eigenstate of Majorana Hamiltonian $H_{\hat{u}}$ |
| $\|\Phi_{\mathcal{P}}\rangle$ | projected, physical state: $\|\Phi_{\mathcal{P}}\rangle = \mathcal{P}\|\Phi\rangle$ |
| $\psi(\mathbf{r})$ | solution to the tight binding model on a hexagonal lattice with slowly varying, weak disorder in hopping strengths |
| $\Psi^{A(B)}(\mathbf{r})$ | vacancy zero mode for a vacancy on the A(B) sublattice |
| $\mathbf{p}$ | two component momentum $\mathbf{p} = (p_\mu, p_\nu)$ |
| $\Pi$ | projection onto ground states of $\widetilde{H}_0$ |
| $\widetilde{O}$ | operator in spin space: with tilde |
| $O$ | operator in the space of Majorana fermions: without tilde |
| $\sigma$ | Pauli matrix |
| $\mathbf{Q}$ | momentum at one of the Dirac points: $\mathbf{Q} = (\frac{2\pi}{3}, -\frac{2\pi}{3})$ |
| $\rho(E)$ | density of states |
| RVB | resonating valence bond |
| $S_m$ | singular values of $M$ |
| $S(\mathbf{q})$ | singular values of the Fourier transform of $M$ |
| $S_R(\mathbf{q}), S_I(\mathbf{q})$ | real and imaginary parts of $S(\mathbf{q})$ |
| $\tau$ | Pauli matrix |
| $T$ | variably, a perturbative T-matrix or temperature |
| $\theta$ | angle between $\mathbf{d}$ and the x axis |
| $\hat{u}_{jk}$ | bond operator determining flux sector and gauge |
| $U$ | variably, part of the singular value decomposition of $M$ or the physical part of $\mathbf{A}(\mathbf{r})$ |
| $V$ | variably, a perturbation or part of the singular value decomposition of $M$ or the gauge part of $\mathbf{A}(\mathbf{r})$ |
| $\widetilde{V}_h$ | Zeeman energy |
| VBS | valence bond solid |
| $W_{-1}$ | the -1 branch of the Lambert W function, evaluated with argument $-h^2\mu^2\nu^2/\lambda$ |
| $\widetilde{W}_p$ | flux operator through a plaquette $p$ |
| $\widetilde{W}_{\hexagon}, \widetilde{W}_{\hexagon}, \widetilde{W}_{\hexagon}$ | three types of plaquette and fluxes found in the Kitaev model with isolated vacancies |
| $\chi^\dagger$ $(\chi)$ | complex bond fermion creation (annihilation) operators |
| $\chi(h)$ | vacancy susceptibility as a function of field |
| $\chi(T)$ | vacancy susceptibility as a function of temperature |
| $\mathcal{Z}$ | partition function |
| $z$ | variably, complex energy $z = E - i\epsilon$ or bond type |

# Chapter 1

# Introduction

Disorder is ubiquitous in condensed matter physics. In areas that require very pure crystals, for example in turbine blades[37], it is something to be avoided but it can also be something useful: disorder can be used to change the properties of a material in a desirable way and can even be used as a probe of a system, providing information about the properties of the material without disorder. Indeed, we are well acquainted with the former process as we have been controlling and using disorder to our advantage for hundreds of years in the form of stained glass. It is the interactions of disorder with light that causes the beautiful hues that are commonplace in churches around the world. Another common example of using disorder in this way is that of doping a semiconductor. This can be thought of as a type of substitutional disorder that allows fine control over a semiconductor's electronic properties. And of course, it is this ability to manipulate their characteristics that means that semiconductors are used in almost every electronic device.

The use of disorder as a probe is less familiar but equally valuable, particularly in condensed matter physics. In most circumstances, the electronic properties of metals are successfully described by Fermi liquid theory, where electron interactions are considered a perturbation on an otherwise free electron gas. There are, however, many phases of matter and physical phenomena that are not well described by such a theory. For example, such disparate systems as Mott insulators, high temperature superconductors, spin liquids, valence bond solids and valence bond liquids all fall under this category. They are collectively termed strongly correlated electron systems and all of them require a new and often intricate theory for their explanation. Most of the parent Hamiltonians describing these systems are not solvable and even their detection can be difficult as many of them lack conventional signatures. For example, as we discuss in section 1.3, a spin liquid does not break any spin rotational or translational symmetry. By way of contrast, the familiar, second order phase transition of a cubic Heisenberg ferromagnet to the ordered phase is accompanied by the

development of a measurable, non-zero, spontaneous magnetisation. However, the interaction of disorder with a strongly correlated electron system can often reveal correlation functions, order parameters and susceptibilities that are otherwise elusive to experiment and which may be used to characterise the system. This thesis demonstrates the effects of certain types of disorder on a strongly correlated system that is a quantum spin liquid, is exactly solvable and contains the necessary elements for a quantum computer: the Kitaev honeycomb model.

This introduction comes in two chapters. The first provides a review of the experiments and theory relating to disorder and its use as a probe in a few well studied models. Also, the physics of both spin liquids and quantum computation are pertinent to understanding the Kitaev honeycomb model and a brief outline of some of their features is included. The second is an extensive introduction to the model itself, describing properties of the clean system and previewing the remainder of this thesis.

## 1.1 Mott insulators and spin Hamiltonians

To embark on an investigation into strongly correlated electron systems, one must first create a Hamiltonian that generates the essential physics of interactions whilst still being simple enough to be susceptible to analytic investigation. One model of choice for over 40 years has been the Hubbard model, originally composed to describe magnetism and the metal-insulator transition in narrow band transition metals[48]. Consider a description of an electron band in terms of a Wannier basis centered around lattice sites at $\mathbf{R}_j$. If the band is narrow, there is little overlap between the single atomic orbitals of each ion, and the Wannier orbitals will be well approximated by these single atomic orbitals. This is the regime of validity of the so called tight binding model where each electron is tightly bound to an ion but can hop between nearest neighbours. Furthermore, the Coulombic interaction between electrons is considered only non-negligible when they are on the same lattice site. With electron creation operators $a^\dagger_{j,\sigma}$ for a Wannier state on site $\mathbf{R}_j$, the Hubbard model is

$$H_{\text{Hubb}} = \sum_{\langle jk\rangle,\sigma} -(t_{jk}a^\dagger_{j,\sigma}a_{k,\sigma} + \text{H.c.}) + U\sum_j n_{j,\uparrow}n_{j,\downarrow}. \tag{1.1}$$

Here, $t_{jk}$ is a kinetic energy term permitting electron hopping and $U$ represents the Coulomb repulsion, approximated as an onsite potential. A broader band implies less tightly bound electrons and that further neighbour hopping terms may be important. Longer range Coulombic interactions can also be considered. $U > 0$ represents a repulsive interaction between electrons, whilst $U < 0$ is an effective attraction between electrons, which may

be generated through, for example, electron-phonon coupling, as in conventional superconductivity. Multiple bands can also be considered, with appropriate inter-band hopping and interaction terms.

In the non-interacting limit $U/t = 0$ the Hubbard model describes a system of non-interacting electrons and the eigenstates are the single particle states. The spectrum may be found by Fourier transform and states are filled according to the Fermi factor and the Pauli principle. This leads to the band theory of metals, semiconductors and insulators. In the ground state, if the highest occupied level lies at the top of a band and there is a gap to the next available level, the system is said to have a band gap and to be a band insulator. At finite temperature some electrons are thermally excited across the band gap, leading to a finite conductivity. If this gap is comparable to $k_B T$ the system is termed a semiconductor. If there is no gap to the next band, if the gap is very much less than $k_B T$, or if a band is only partially filled, the system is a metal.

In the opposite, atomic, limit $t/U = 0$ each site is uncoupled and the energy levels are macroscopically degenerate, with gaps $U$ between them. The energy is dictated solely by the site occupancy. With one electron per site and with $2N$ sites this leads to a degeneracy of $2^{2N}$ since electrons on each site can be in one of two spin orientations. If the system is half filled, so that there is one electron per site, Coulombic interaction between electrons prevents hopping and it is said to be a Mott insulator. This is qualitatively different to the insulating properties of a band insulator. Doping a Mott insulator will lead to fractional filling and conductivity as the electrons or holes can move without energy cost.

By changing the parameter $t/U$ one can tune between these two limits and investigate properties of the insulator - metal transition and by further allowing a sign change in $U$ and variable filling fraction, one discovers a wide variety of phases including ferromagnetism, antiferromagnetism and superconductivity. The stable phase is typically dependent on both the temperature and dimensionality of the system.

In the strong coupling limit $t/U \ll 1$ the degeneracy of the atomic limit mentioned above is broken by finite coupling $t$. In this limit, double occupancy is energetically unfavourable and perturbation theory can be performed using $t/U \ll 1$ as a small parameter. Electrons can perform only virtual hops onto neighbouring sites, where the allowed virtual hopping processes are determined by energetics and the Pauli principle. This leads to a kinetic energy term and an effective spin interaction:

$$H_{t-J} = \sum_{\langle jk \rangle, \sigma} -(t_{jk} a^{\dagger}_{j,\sigma} a_{k,\sigma} + \text{H.c.}) + J \sum_{\langle jk \rangle} (\mathbf{S}_j \cdot \mathbf{S}_k - \tfrac{1}{4} n_j n_k). \tag{1.2}$$

At half filling, i.e. with one electron per site, the kinetic energy must be zero and Eq. (1.2) reduces to the familiar Heisenberg antiferromagnetic (HAF) Hamiltonian:

$$H_{Heis} = J \sum_{\langle jk \rangle} (\mathbf{S}_j \cdot \mathbf{S}_k - \tfrac{1}{4}), \tag{1.3}$$

where, of course, the constant is unimportant. In the ground state manifold of $t/U \to 0$ states, one electron must be maintained on every site, so only exchange processes can occur. The constant $J = 4t^2/U$ is therefore referred to as an exchange coupling.

The above Hamiltonian was obtained by considering hopping between electron orbitals that could accommodate two electrons (spin $\uparrow$ and spin $\downarrow$). However, if the outer shell of the ion can accommodate more electrons, as is the case for the rare earths or transition metals, then the energetically favourable spin configurations can lead to an effective Hamiltonian of spins of larger magnitude, (spin $\frac{1}{2}$, 1, $\frac{3}{2}$, 2, ...) or with exchange coupling of negative sign (ferromagnetic). Also, super-exchange, where the electron hopping is mediated by an additional ion, spatial anisotropy in interactions and spin-orbit coupling can lead to more exotic spin Hamiltonians (e.g. Ising, XXZ, quantum compass model or the Kitaev honeycomb model). Later we shall see in more detail how the Kitaev honeycomb model may be generated in this way.

Although greatly simplified, the HAF Hamiltonian is generically not solvable in spatial dimensions greater than one: usually a scheme must be used where the low energy degrees of freedom are approximated by an effective field theory that is hoped to display the characteristics of the spin system at low temperatures. The inclusion of disorder in exchange couplings or substitution of ions leads to yet more difficulties. However, there has been much progress, particularly in one dimension, with both the theory and experiments and in the remainder of this chapter we review some elements of that progress and elucidate on the uses of disorder.

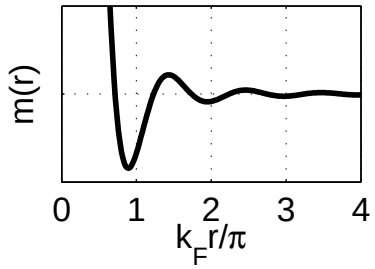
## 1.2 Disorder in strongly correlated systems

In common metals, even though the interactions between electrons can be larger than the kinetic energy, most transport properties are well described by Fermi liquid theory: the elementary excitations are electron quasi-particles that, to a good approximation, can be considered non-interacting. Fermi liquid theory is successful at describing the properties of metals governed by excitations within order $k_B T$ of the Fermi energy, such as conductivity, but does not account for properties involving electron levels far from the Fermi surface, such as photoelectric emission or optical absorption. Even in these simple metals, disorder

can have dramatic effects. We illustrate this point with two examples: the Ruderman, Kittel, Kasuya, Yosida (RKKY) interaction and the Kondo effect. There is a tremendous amount of literature on both subjects and we merely make a sketch of the theory.

The RKKY interaction describes the response of a non-interacting electron gas to a local magnetic field. A perturbation of this type could be achieved, for instance, by the introduction of a magnetic ion into an otherwise non-magnetic metal. In this case the potential may be approximated by a delta function in real space, which implies a uniform perturbing field in $\mathbf{q}$-space: $h_{\mathbf{q}} = h$. The particular form of the response results from the wavevector $\mathbf{q}$-dependent susceptibility $\chi_{\mathbf{q}}$ that is smoothly cut off above the Fermi wavevector $k_F$. If the unperturbed electron gas has Pauli paramagnetism $\chi_p$, then the real space magnetisation of the electron gas in response to this delta function perturbation is

$$\begin{aligned} m(r) = & \frac{h}{(2\pi)^3}\int_{q=0}^{\infty}\chi_{\mathbf{q}}e^{i\mathbf{q}.\mathbf{r}}d^3\mathbf{q} \\ = & \frac{2k_F^3\chi_p h}{\pi}\left(\frac{-2k_F r\cos(2k_F r)+\sin(2k_F r)}{(2k_F r)^4}\right) \end{aligned}$$




A plot of $m(r)$ is shown on the right. Since the Fermi wavevector is finite, the electron gas does not have high enough frequency components to respond completely to the perturbation and the cut off in momentum space implies the oscillating behaviour seen in real space. Two immobile magnetic impurities in a metal will both generate a magnetisation of the above form and will interact either ferromagnetically or antiferromagnetically dependent on their separation. A similar result can be derived for the response of the electron gas to a charge impurity and leads to Friedel oscillations.

The Kondo effect describes the response of the electrons to an impurity of the above type. Above some critical temperature $T_K$ the impurity behaves as though it was a free paramagnetic impurity. Below $T_K$, the electrons close to the impurity align with opposite magnetisation, screening it and generating a composite object with spin zero. This has two major consequences: the first is that the susceptibility falls below a Curie response for temperatures below $T_K$; secondly, since the impurity is interacting strongly with the conduction electrons, impurity scattering is enhanced and at low temperatures the resistivity actually increases as $\rho \propto \ln(1/T)$. At the lowest of temperatures this will be cut off at a finite value dependent on the concentration of impurities. Contrast this to a metal with non-magnetic impurities, where the resistivity decreases monotonically with decreasing $T$ to a constant term, also dependent on the concentration of impurities.

It is clear that even for common metals, not only can disorder have dramatic effects but it can also provide information about the pure system: the RKKY interaction gives us an idea that a Fermi surface exists and its oscillations are a measure of the size of the Fermi wavevector $k_F$. Disorder continues to be a useful probe of strongly correlated electron systems and below we review some of the advances that have been made in both the theory and experiment of low dimensional quantum spin systems. We will see that, like for common metals, it can both generate new physics and also tell us about the properties of the clean system. We focus on the Heisenberg antiferromagnets in one and two dimensions, the cuprates and graphene.

### 1.2.1 Spin-$\frac{1}{2}$ Heisenberg antiferromagnetic chain

One dimensional systems are attractive from a theoretical viewpoint as they are in some cases exactly solvable. Of these, the spin-$\frac{1}{2}$ HAF chain, Eq. (1.3) in 1D, is the prototypical example of a critical spin liquid and the effects of both substitutional disorder and disorder in exchange interactions in this system have been studied in detail. We provide a review of both the theory and experiments below.

For a translationally invariant chain, the Marshall and Lieb-Schultz-Mattis theorem shows that the ground state has total $S^z = 0$ and is non degenerate with gapless excitations [55]. In addition, the ground state and spectrum of a finite length chain may be found exactly by the Bethe ansatz[13, 24] and the results can be extended to give information about the thermodynamic limit. Using the Bethe ansatz one can find the ground state energy and show that the ground state has no long range magnetic order[12]. Furthermore, at zero temperature the magnetic susceptibility is a constant $1/J\pi^2$[41]. In fact, the spin-$\frac{1}{2}$ Heisenberg chain with open boundaries is completely solvable using the Bethe ansatz, so that many quantities, such as thermodynamic properties, can be found exactly in the ground state[9, 30, 33, 34].

A physical picture of the ground state is a superposition of states in which spins are paired into singlets, with those pairings occurring on all length scales. This ground state can be described as a critical resonating valence bond (RVB) liquid state. Excitations above the ground state consist of pairs of spin-$\frac{1}{2}$ spinons that may propagate almost independently[24]. This is an example of fractionalisation, as can be seen in the following manner. The HAF Hamiltonian is rotationally invariant and its eigenstates may therefore be characterised by the quantum numbers of total spin $S_T$ and total spin in the z-direction $S_T^z$. Excitations above the ground state change $S_T^z$ by one. However, this spin-1 excitation is fractionalised into two spin-$\frac{1}{2}$ degrees of freedom. This is in addition to the fact that existance of a purely spin excitation already involves spin-charge separation of the electrons. A pictorial

example example of fractionalisation can be seen in Figure 1.1, where we draw a cartoon of soliton propagation in a spin-$\frac{1}{2}$ Ising antiferromagnetic chain.

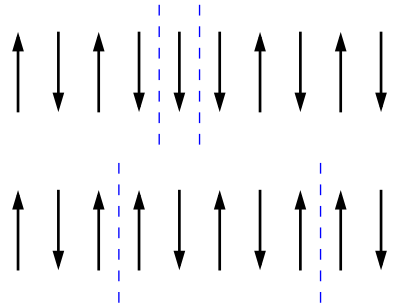


Figure 1.1: Cartoon of soliton propagation in a spin-$\frac{1}{2}$ Ising antiferromagnetic chain $H = J\sum_{\langle jk\rangle} S_j^z S_k^z$. Each blue, dashed line (bottom) represents a spin-$\frac{1}{2}$ soliton fractionalised from a spin-1 elementary excitation (top).

The correlation functions can be calculated at zero temperature[2, 55, 61, 82]

$$\langle S_x^z S_0^z\rangle = C_1\frac{1}{x^2} + C_2(-1)^x\left(\frac{1}{x}\right)\ln x^{1/2} \tag{1.4}$$

and can also be found at small, non-zero temperatures. The fluctuation-dissipation theorem allows the magnetic susceptibility in a uniform field to be calculated from the spin correlations[28]

$$\chi(T) \equiv \frac{1}{T}\sum_j \langle S_j^z S_0^z\rangle = \frac{1}{J\pi^2}\left(1 + \frac{1}{2\ln(T_0/T)}\right) \qquad \text{for } T_0 \simeq 7.7J. \tag{1.5}$$

In particular, notice that the susceptibility is finite for the pure chain at low $T$. This is characteristic of a gapless system with a divergent correlation length at low $T$. The correlation length is given by[40, 70]

$$\xi_{1D} \sim \frac{1}{T}\left(\frac{1}{2 - [\ln(J/0.3733T)]^{-1}}\right). \tag{1.6}$$

Experimentally, $Sr_2CuO_{3+\delta}$ is an almost ideal example of a spin-$\frac{1}{2}$ HAF chain. It has nearest neighbour exchange coupling $J \sim 2200$K and a low Néel temperature $T_N \sim 5$K $\sim 0.002J$[6, 67]. The 1D chains are composed of magnetic copper ions coupled via superexchange through oxygen ions. The interchain coupling $J_\perp$ is small, with $J_\perp/J \sim 10^{-5}$, which gives rise to the low Néel temperature. At temperatures $T < T_N$ interchain coupling becomes important and long range antiferromagnetic order appears. The crystal structure of $Sr_2CuO_3$ is shown in Figure 1.2(a).

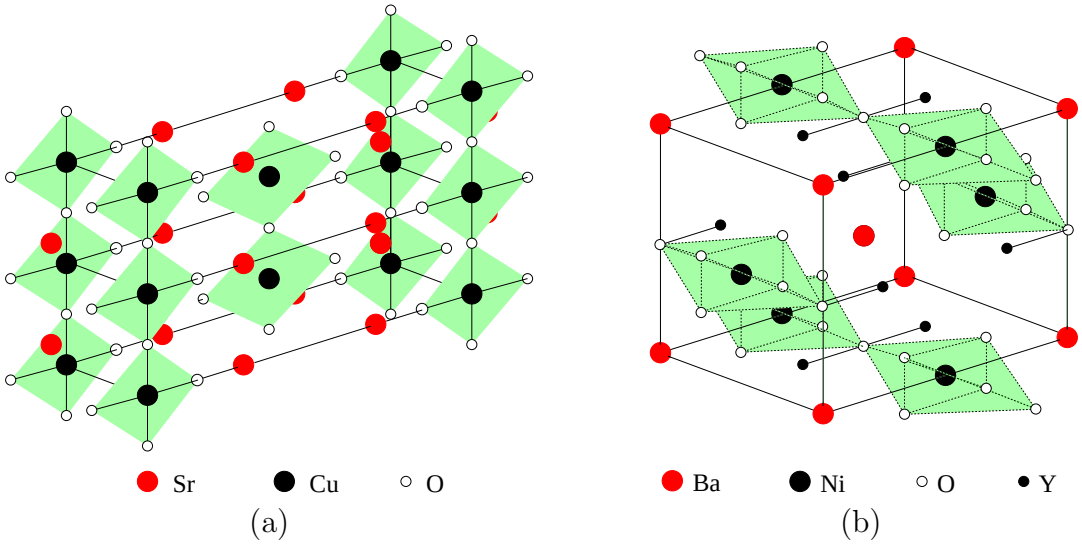



Figure 1.2: a) Spin $\frac{1}{2}$ HAF chains: two conventional unit cells of $Sr_2CuO_3$. b) Spin 1 HAF chains: one conventional unit cell of $Y_2BaNiO_5$. In both figures 1D Heisenberg chains are shown in green, where copper or nickel ions interact via super exchange with the oxygen ions.

Measurements on this material showed a Curie contribution to the magnetic susceptibility that could be significantly reduced by annealing[6, 67]. This was attributed to an excess of oxygen, which could then be reduced by the annealing. In this case the excess oxygen is expected to be in an $O^{2-}$ ionization state and lie in an interstitial site, doping the sample with two holes[83]. If these holes are immobile they can result in a break in the chains, or can even magnetically isolate a $Cu^{2+}$ ion from the chains, giving rise to a paramagnetic ion and hence the observed Curie contribution to the susceptibility. It has also been suggested that the Curie term may be instead due to a decomposition of $Sr_2CuO_3$ to paramagnetic $Sr_2Cu(OH)_6$ on the surface when the sample is exposed to air[44]. Further experiments have been performed on $Sr_2Cu_{1-x}Pd_xO_{3+\delta}$[53], where an almost Curie contribution was found that depended on the concentration of substituted palladium and that was not reduced by annealing. Palladium is a non magnetic ion that effectively cuts the $CuO_2$ chains and so it was concluded that there is an almost Curie contribution coming from the HAF chains themselves with the cause being that some were now of finite length. The Curie contribution of finite chains has been well documented in the theory and we present some of the results below.

Consider a chain of length $N$. The low-lying energy states have a linear dispersion[24] with finite energy gap out of the ground state of $O(J/N)$. Therefore, at the lowest of temperatures $T/J \ll 1/N$ the system will be in its ground state. For even length chains, this is

an RVB singlet as described above, with exponentially small susceptability as $T \to 0$. For odd length chains, the system is a spin-$\frac{1}{2}$ doublet and thus exhibits a Curie susceptibility. In the opposite regime, where $1/N \ll T/J$, the susceptibility can be split into a bulk and boundary contributions[83] and the boundary spin susceptibility $\chi_B$ calculated as[35]

$$\chi_B = \frac{1}{12NT\ln(T_0/T)}\left(1 - \frac{\ln\ln(T_0/T)}{2\ln(T_0/T)} + \dots\right) , \tag{1.7}$$

where $T_0 = \sqrt{\pi/2}\exp(1/4+\gamma)$, with $\gamma$ the Euler constant. At zero temperature, one finds a boundary spin susceptibility for a small field $h$ [35]

$$\chi_B(T=0) = \frac{1}{4Nh[\ln(2\pi T_0/h)]^2}\left(1 - \frac{\ln\ln(2\pi T_0/h)}{\ln(2\pi T_0/h)} + \cdots\right) . \tag{1.8}$$

It is also possible to interpolate smoothly between the two regimes $T/J \ll 1/N$ and $1/N \ll T/J$ [83]. The form of the magnetisation that accompanies the divergent boundary susceptibility can be seen as follows. Define the staggered and uniform susceptibilities through the total susceptibility on site $j$ as $\chi_j = \chi_{u,j} + (-1)^j\chi_{s,j}$. It can be shown that for a half-infinite chain in a finite field the staggered magnetisation $M_s$ initially *increases* with distance $x$ from the chain end before decaying[26]:

$$M_{\rm s} = h(-1)^x\frac{1.16}{\pi}\frac{x}{\sqrt{(J/2T)\sinh(4Tx/J)}}. \tag{1.9}$$

As the temperature is lowered, the envelope of this staggered magnetisation extends across the whole chain length[27].

One can thus observe Curie and almost Curie behaviour over two energy scales, with the higher temperature Curie 'constant' in Eq. (1.7), having a logarithmic temperature dependence. The physical intuition for the above behaviour is the following: since the boundary breaks translational invariance, momentum is no longer a good quantum number. This means that the long range alternating part of the spin correlations in Eq. (1.4), will have an effect on both the staggered and uniform susceptibility and lead to the observed Curie contribution from the chain ends. This boundary susceptibility predicts well the observed Curie like behaviour of $Sr_2Cu_{1-x}Pd_xO_{3+\delta}$[53].

We have seen that the theory and experiment of finite length spin-$\frac{1}{2}$ HAF chains agree well. Since the agreement was dependent on having a correct understanding of correlation functions in the clean system, the controlled introduction of impurities has provided a useful test of these functions through the form of the boundary susceptibility and staggered magnetisation envelope. This concludes the first of several examples in this introduction where disorder is used as a probe of a strongly correlated electron system.

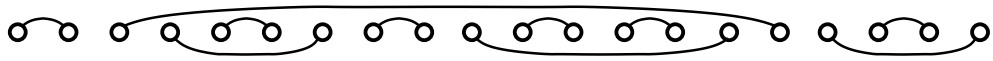


Figure 1.3: From Ref. [32], a schematic of the random singlet phase. Spins are most likely to pair with another nearby spin but via the RG procedure some spin pairs occur over arbitrarily large distances. Note that the RG procedure does not generate any bonds that cross each other.

So far we have only considered substitutional disorder but disorder in exchange coupling is also common. This could result, for instance, from some non-uniform strain being exerted on the crystal either by external forces or from the random strains imposed on the lattice by the random substitution of ions of different sizes. The strain can alter the overlap of the Wannier orbitals that permit virtual hopping in the Mott insulator. In turn, this will alter the exchange coupling as $J = 4t^2/U$, see Eq. (1.3). As for substitutional impurities that break the chains, this type of disorder has remarkable effects on the susceptibility and below we demonstrate that it also leads to an almost Curie divergence at low $T$.

Given an initial broad distribution of exchange couplings, the density of states and a picture of the low lying states of such a disordered HAF chain can be found via a real space renormalisation group (RG) technique. This proceeds in the following manner. First, find the largest coupling in the system and pair these spins into a singlet. Since the distribution of bare couplings is broad, this coupling will typically be much larger than the couplings of other sites to those in the bound pair. The other couplings can therefore be treated as a perturbation, the bound pair decimated out and renormalised couplings found. This procedure can be iterated, removing the high energy degrees of freedom, which are irrelevant at small $T$, but without changing the nature of the low lying states. Crucially it is found that the distribution of couplings actually broadens under the RG, making the procedure asymptotically exact at low energies. Since these couplings can occur on all length scales, the low energy states of the system have been described as a 'random-singlet phase'[14]. A schematic of the random-singlet ground state is shown in Figure 1.3.

Disorder of this type leads to a divergent density of states at low energies[32], from which the susceptibility may be found in the following way. Let the RG procedure be iterated until the largest energy scale in the system is $\Omega$. If $T \ll \Omega$, the excitations of pairs already decimated out will only be weakly excited by thermal fluctuations. On the other hand, when $\Omega \ll T$, one would expect all spins not yet decimated out to be essentially free and lead to a Curie like contribution to the susceptibility. A more detailed analysis confirms this heuristic picture, with the susceptibility found to be[32]

$$\chi \sim \frac{1}{T[\ln(T_0/T)]^2} \ . \tag{1.10}$$

### 1.2.2 Spin-1 Heisenberg antiferromagnetic chain

A spin-1 chain is qualitatively very different from the spin-$\frac{1}{2}$ case and unlike the spin-$\frac{1}{2}$ case cannot be solved exactly by the Bethe ansatz. Despite its differences, a finite spin-1 chain also has a Curie contribution to the susceptibility. Before describing the finite chain, first we examine the properties of the infinite chain. A picture of the ground states and elementary excitations were obtained by Affleck, Kennedy, Lieb and Tasaki[3]. Their approach was to consider a so called *valence bond solid* (VBS) state and then find a Hamiltonian for which it was the unique ground state. It can then be shown that this Hamiltonian resembles closely that of the spin-1 HAF chain. The concept of 'closeness' for a Hamiltonian we shall make more precise later. The VBS state for a spin-1 chain can be defined using the Schwinger bosons representation of spins. Here, the spin operators are represented using two boson operators $a$ and $b$

$$\begin{aligned} S^x + iS^y &= a^\dagger b, \\ S^x - iS^y &= b^\dagger a, \\ S^z &= \tfrac{1}{2}(a^\dagger a - b^\dagger b). \end{aligned} \tag{1.11}$$

The physical subspace for spin $S$ is defined through the condition that $a^\dagger a + b^\dagger b - 2S = 0$. The spin states of a single spin are given by

$$|S, S^z\rangle = \frac{(a^\dagger)^{S+S^z}}{\sqrt{(S+S^z)!}} \frac{(b^\dagger)^{S-S^z}}{\sqrt{(S-S^z)!}} |0\rangle, \tag{1.12}$$

where $S$ and $S^z$ as usual label the eigenvalues for the $\mathbf{S}^2$ and $S^z$ operators. Two spin-$\frac{1}{2}$ states are given by $|\uparrow\rangle = a^\dagger|0\rangle$ and $|\downarrow\rangle = b^\dagger|0\rangle$. The VBS state for a spin-1 chain is then given by[10]

$$|\Psi^{\mathrm{VBS}}\rangle = \prod_{\langle jk \rangle} \left( a_j^\dagger b_k^\dagger - b_j^\dagger a_k^\dagger \right) |0\rangle \tag{1.13}$$

In the above state, each spin-1 degree of freedom should be viewed as being decomposed into two spin-$\frac{1}{2}$ degrees of freedom that then form singlet bonds with neighbouring sites, as shown in Figure 1.4(top). Define a projection operator $\mathcal{P}_J(jk)$, that projects the bond spin $\mathbf{J}_{jk} = \mathbf{S}_j + \mathbf{S}_k$ onto the subspace with total spin quantum number $J$. Two neighbouring sites are decomposed into four spin half degrees of freedom, two of which are locked into a singlet. Thus, the maximal spin of any bond in this VBS state is 1 and it is therefore a ground state of the following Hamiltonian

$$H^{\mathrm{AKLT}} = K \sum_{\langle jk \rangle} \mathcal{P}_2(jk), \tag{1.14}$$

where $K$ is a positive constant. In fact, one dimensional, rotationally and translationally invariant, integer spin Hamiltonians have a unique ground state with a gap to excitations[42,

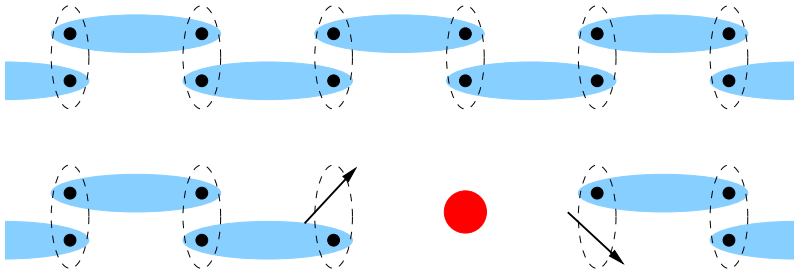


Figure 1.4: Top: Illustration of the VBS state for a spin-1 HAF chain. Each spin-1 is split into two spin-$\frac{1}{2}$ degrees of freedom, represented by black dots. Blue ellipses represent valence bonds between two spin-$\frac{1}{2}$ variables. Bottom: A non magnetic impurity cuts the chains, leaving two effective, free, spin-$\frac{1}{2}$ degrees of freedom at the chain ends.

43]. $H^{\mathrm{AKLT}}$ satisfies these conditions and therefore the VBS state is the unique ground state. Furthermore, this Hamiltonian is equivalent to a spin Hamiltonian

$$H^{\mathrm{AKLT}} = K \sum_{\langle jk \rangle} \left[ \frac{1}{2} \mathbf{S}_j \cdot \mathbf{S}_k + \frac{1}{6} \left( \mathbf{S}_j \cdot \mathbf{S}_k \right)^2 + \frac{1}{3} \right], \tag{1.15}$$

which itself has a ground state and excitations that are similar to those predicted by other means for the spin-1 HAF chain. In this sense, we say that this Hamiltonian is close to the spin-1 HAF chain and that the VBS state presented here will be a good approximation to the true ground state of that chain. Early work by Haldane showed that there is a gap $\Delta_{Hal}$ to excitations, which correspond to breaking a singlet bond and forming a spin-1 triplet[42, 43]. This VBS state has no long range magnetic order and spin correlations that decay as

$$\langle \mathbf{S}_0 \cdot \mathbf{S}_n \rangle = (-1)^n (S+1)^2 e^{-\kappa |n|}, \qquad 0 < n, \qquad \kappa = \ln \left( 1 + \frac{2}{S} \right) . \tag{1.16}$$

By different methods, the correlation functions and susceptibility of the spin-1 HAF chain can be found in the low temperature limit[1, 21, 38].

$$\langle \mathbf{S}_x \cdot \mathbf{S}_0 \rangle \sim (-1)^x \frac{e^{-|x|/\xi}}{\sqrt{|x|}} \qquad \chi(T) \sim \frac{e^{-\Delta_{Hal}/T}}{\sqrt{T}} \tag{1.17}$$

The correlation length $\xi$ is finite and as $T \to 0$, $\xi \sim 6$. A given experimental realisation of a spin-1 Heisenberg chain will have a correlation length in units of the interatomic spacing that is dependent on microscopic parameters.

### Experiment

Experimentally, $Y_2BaNiO_5$ provides a good instance of a HAF spin-1 chain. The crystal structure is shown in Figure 1.2(b). It has a gap $\Delta_{Hal} = 100$K, intra-chain coupling

$J = 285$K and inter-chain coupling $|J_\perp/J| < 5 \times 10^{-4}$, see Ref.[22] and references therein.

As in the case of spin-$\frac{1}{2}$ HAF chains, finite chain lengths may be created by substitution of non-magnetic ions or doping with excess oxygen. A chain break leaves two unpaired effective spin-$\frac{1}{2}$ variables on the sites adjacent to the impurity as demonstrated in Figure 1.4(bottom). These will then give a Curie like contribution to the susceptibility. Experiments where non-magnetic zinc is substituted into the crystal indeed show a Curie contribution corresponding to about two paramagnetic spin-$\frac{1}{2}$ per zinc atom as expected, see Ref.[22] and references therein.

At the chain end, quantum Monte Carlo simulations on a chain of length $L$ show that the magnetisation oscillates with an exponential decay envelope given by[4]:

$$\langle S_j^z \rangle \propto e^{-(j-1)/\xi} + e^{-(L-j-1)/\xi} \tag{1.18}$$

Crucially, the correlation length here is that of the pure system. Thus if one could measure this oscillating magnetisation, it would be a direct measurement of the correlation function in the clean system. This form has been confirmed in $Y^{89}$ NMR experiments, where the frequency shift of magnetic resonance of the yttrium atoms is directly proportional to the local magnetisation of the adjacent nickel atoms. The yttrium therefore probes the magnetisation on a site by site basis. Since the magnetisation alternates, one would expect the frequency shift in NMR experiments to be alternating positive and negative and this is indeed what is seen in experiments on doped $Y_2BaNi_{1-x}A_xO_5$ [22, 84]. Here, A is Mg, Cu or Zn and causes chain breaks, leading to finite length Haldane chains. Furthermore, these experiments observe a staggered magnetisation that has a decay length $\xi$ with a temperature dependence in excellent agreement with the correlation length of the pure system found using quantum Monte Carlo calculations on undoped $Y_2BaNiO_5$ [50].

### 1.2.3 Two dimensional Heisenberg antiferromagnets

We have seen that in one dimension impurities can have a startling affect on the thermodynamic properties of a system. Furthermore, because they are exactly or quasi-exactly solvable by several methods, one dimensional systems afford an opportunity to compare the theory with experiment and the two are seen to align well. Two dimensional systems generally do not accede to analytic interrogation and an approximate theory must be established. The quantum non-linear sigma model is the simplest continuum theory that correctly reproduces the long wavelength spin-wave spectrum and spin-wave interactions of the 2D HAF and has met much success in predicting its properties both in the clean system and with impurities. Earlier attempts using linear spin-wave theory also had some success,

correctly reproducing the qualitative features of pure and disordered 2D HAF. Computational modelling using Quantum Monte Carlo has been widely used in corroborating the theoretical predictions, which are also consistent with experimental observations.

Before looking at true two dimensional systems one can gain an intuition of their properties by an investigation into quasi-one dimensional systems: ladders with a number of legs $M$. Properties of these ladders for arbitrary $M$ can be determined using the non-linear sigma model. For spin-$\frac{1}{2}$ ladders with an even $M$ there is a gap to excitations that decreases exponentially with the number of legs $\Delta_{\text{lad}} \sim \exp[-(\pi/2)M]$ and which accompanies a finite correlation length at zero temperature $\xi_{\text{lad}} \sim \Delta_{\text{lad}}^{-1}$ [23, 40]. Odd leg ladders lead to gapless excitations and algebraic correlations. Extending these results to $M \to \infty$, we would expect that a true, two dimensional HAF would have gapless excitations and divergent correlation length as $T \to 0$ and we will see that this is indeed the case.

Studying two dimensional HAF's is not merely a theoretical exercise: the $CuO_2$ planes in $La_2CuO_4$ form a HAF and are believed to be responsible for its high temperature superconducting properties. Doping $La_2CuO_4$ with, for example, strontium leads to the substitution of $Sr^{2+}$ ions for $La^{3+}$ ions and the injection of a hole into the $CuO_2$ planes. Doping with excess oxygen on sites out of the $CuO_2$ planes has a similar effect, drawing an electron out from those planes and it is this doping which ultimately leads to superconductivity over some particular doping and temperature range. In section 1.2.4 we provide a brief discussion of some generic features of the family of cuprate compounds and at this stage only draw the reader's attention to a schematic of their phase diagram in Figure 1.6.

According to the Mermin-Wagner theroem, the pure 2D HAF cannot be ordered at any finite temperature, as this would involve breaking a continuous symmetry. It does, however, form a Néel ordered state strictly at $T = 0$. In reality, deviations from true 2D HAF will cause the system to order below some finite temperature $T_N$. This may be weak inter-plane coupling or an easy axis asymmetry that destroys the rotational invariance of the Hamiltonian. Nevertheless, even for a pure 2D HAF, as the temperature decreases, algebraic spin correlations develop and it is these correlations that largely control the behaviour when impurities are added. For the square lattice, spin-wave velocity $c$, spin stiffness $\rho_s$ and at low temperatures, the antiferromagnetic correlation length is observed to increase exponentially with temperature[39]:

$$\frac{\xi}{a} = \frac{e}{8}\frac{c}{2\pi\rho_s a} e^{2\pi\rho_s/T}\left[1 - \frac{1}{2}\left(\frac{T}{2\pi\rho_s}\right) + O\left(\frac{T}{2\pi\rho_s}\right)^2\right]. \tag{1.19}$$

The pure system has finite susceptibility as $T \to 0$ but introduction of an impurity of

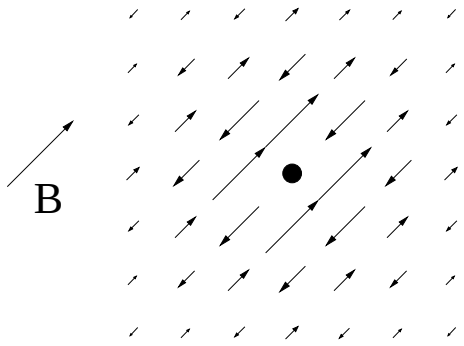



Figure 1.5: Illustration of the staggered magnetisation with Curie divergent susceptibility that forms around a non magnetic impurity in a 2D HAF.

spin $S_i$ into the system results in an impurity susceptibility[16, 45, 80]

$$\chi^z_{\text{imp}} = \frac{S_i^2}{3T}\left[1 + \frac{T}{\pi\rho_s}\ln\left(\frac{C_1\rho_s}{T}\right) - \frac{T^2}{2\pi^2\rho_s^2}\ln\left(\frac{C_2\rho_s}{T}\right) + O\left(\frac{T}{\rho_s}\right)^3\right] . \tag{1.20}$$

A heuristic picture of the leading order Curie contribution can be made by considering a classical Ising antiferromagnet[8]. For a system of 2N spins, removal of one of the spins will lead to an effective spin of size $NS$ on one sublattice and $NS-1$ on the other. The difference leading to an effective spin-$\frac{1}{2}$ object, which is free to orientate itself in either direction along the Ising axis, thus leading to a Curie contribution. Of course, the 2D HAF is not Ising nor classical and in fact the development of algebraic order can account for only about 60% of the Curie behaviour[81]. The other 40% can be attributed to the generation of a local moment[8]. The impurity moment takes the form of a staggered magnetisation centered on the impurity, with the non-trivial spatial extent of this magnetisation leading to the subleading terms in Eq. (1.20). An illustrative picture of the impurity moment is shown in Figure 1.5.

In one dimension, the introduction of impurities cuts the chains, giving an edge to the system. One would expect that this would enhance spin fluctuations and lead to an increase in the susceptibility and indeed, this is what is observed in both experiment and theory. In two dimensions boundaries are not created by impurities but by the physical limits of the system. Furthermore, some nanoscale devices are of a size where edge physics may be significant and even dominant. We therefore briefly comment on the observed edge behaviour of 2D HAF.

For a system with $a$ free edges, size $L \times L$ and susceptibility $\chi_a$, the edge susceptibility $\chi_E$ can be defined as

$$\chi_E = (\chi_a - \chi_0)/aL , \tag{1.21}$$

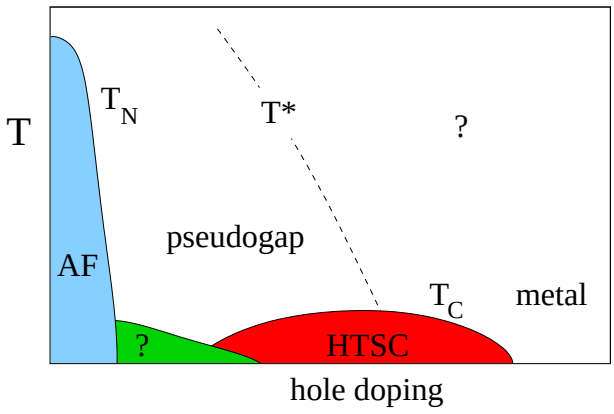



Figure 1.6: A schematic of the phase diagram for a generic HTSC.

where $\chi_0$ is the susceptibility of a periodic system, also of size $L \times L$. Contrary to one's normal intuition, the edge susceptibility for a smooth edge diverges logarithmically but is *smaller* than the bulk $\chi_E \propto -\ln(J/T)$. This can be attributed to enhanced singlet formation near the edges. In contrast to this, a rough edge shows a logarithmically *greater* susceptibility than the bulk $\chi_E \propto \ln(J/T)$. Here, singlet formation is impeded due to local sublattice imbalance[46].

### 1.2.4 The cuprates

There is a tremendous amount of literature on the cuprates and we do not undertake a review of the subject. Instead we provide a brief explanation of their relation to the 2D HAF already discussed and look at the use of non-magnetic impurities to reveal the d-wave symmetry of the superconducting order parameter. For a review of the effects of disorder across the phase diagram of the cuprates and high temperature superconductors (HTSC) in general, see e.g. Ref. [5].

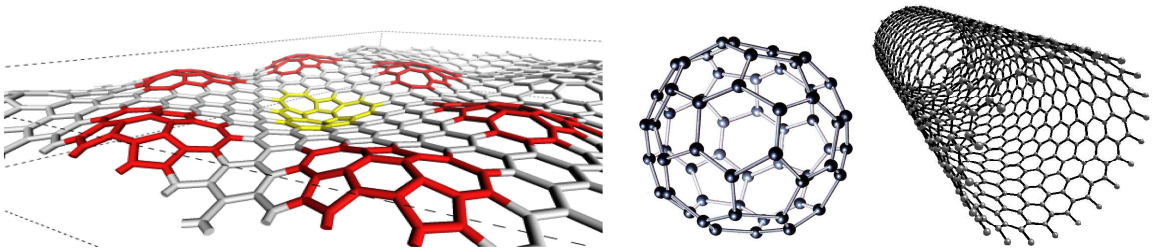
The crystal structure of the cuprates consists of planes of copper oxide $CuO_2$ separated by non-magnetic spacer layer of atoms such as lanthanum ($La_2CuO_4$) or yttrium and barium ($YBa_2Cu_3O_6$). The undoped crystals are good Mott insulators and the $CuO_2$ planes are candidates for the formation of a 2D HAF as they have a large Heisenberg exchange $J \simeq 1500$ K [59]. Of course, the $CuO_2$ planes are not isolated but have small inter-plane couplings that cause long range AF correlations to develop below a Néel temperature $T_N$. Long range correlations may be caused also by an in-plane deviation from an ideal 2D HAF, for example exchange anisotropy, and in fact this may even be the controlling mechanism for determining $T_N$ [62]. A schematic of the familiar, yet unresolved, phase diagram is shown in Figure 1.6. At low temperatures, hole doping the $CuO_2$ layers eventually destroys

the antiferromagnetic order and one enters a high temperature superconducting (HTSC) regime via an intermediary phase. This intermediary phase is somewhat material specific and, for example, may be a striped or spin glass phase. Further doping, beyond the HTSC, causes a phase transition to a metal described by Fermi liquid theory. Above the HTSC phase there is the pseudo-gap region, so termed because as the HTSC phase is approached from above in $T$, there is a drop in the magnetic susceptibility, as if a gap were opening up. In fact, at $T_C$ there is still some small density of states at the Fermi energy, hence the notation pseudo-gap. Increased doping in the pseudo-gap regime causes a cross over to a 'strange metal' that is not well described by Fermi-liquid theory. This brief description of the phase diagram is a heavy simplification and as advertised, there is a wealth of theory and experiments that go a long way to describing these phases in depth. Nevertheless, many of them are still widely debated.

The superconducting gap in reciprocal space $\Delta_{\mathbf{k}}$ (the order parameter) is a measure of the off diagonal long range order: $\Delta_{\mathbf{k}} = -\sum_{\mathbf{q}} V_{\mathbf{kq}} \langle c_{-\mathbf{q},\downarrow} c_{\mathbf{q},\uparrow} \rangle$, where $c_{\mathbf{q},\sigma}$ is an annihilation operator for an electron in momentum state $\mathbf{q}$ and spin $\sigma$, and $V_{\mathbf{kq}}$ is the interaction strength between two such electrons with momenta $\mathbf{k}$ and $\mathbf{q}$. It can be shown experimentally that the superconducting gap is not uniform in $\mathbf{k}$ space. In fact, it is maximal along the direction of the CuO bonds, with nodes on the diagonals and is hence termed a d-wave superconductor, with $\Delta_{\mathbf{k}} = \Delta_0(\cos k_x a - \cos k_y a)$ [85]. The addition of non-magnetic Zn impurities into the $CuO_2$ layers generates localised areas at the impurity sites where superconductivity is almost completely destroyed. This is accompanied by in increase in the local density of states (LDOS) that in turn is associated with the formation of a bound impurity state in the gap. Furthermore, this LDOS has a four-fold symmetry that exactly aligns with the superconducting order parameter[73]. All of these experimental results had been theoretically predicted by the introduction of unitary scatterers into a d-wave superconductor. In this case a unitary scatterer is one that has s-wave scattering, with a phase shift of $\pi/2$. Thus, the introduction of non-magnetic impurities has proved an invaluable tool for observing the order parameter of a d-wave superconductor.

### 1.2.5 Graphene

It has long been known that graphite is composed of stacked layers of graphene, weakly bound together by Van de Waals forces. Of course, it is this weak bonding that enables us write with a pencil, where layers of graphite peel off and are left on the page. It was not until quite recently, however, that stable, single layers of graphene could be isolated and identified[71]. Later it will be apparent that certain features of the Kitaev model involve



(a) (b) (c)

Figure 1.7: a) Pentagons and heptagons cause local warping of graphene. b) Graphene formed into a rounded fullerene. c) Graphene wrapped into a carbon nanotube. Figure (a) from Ref. [17]

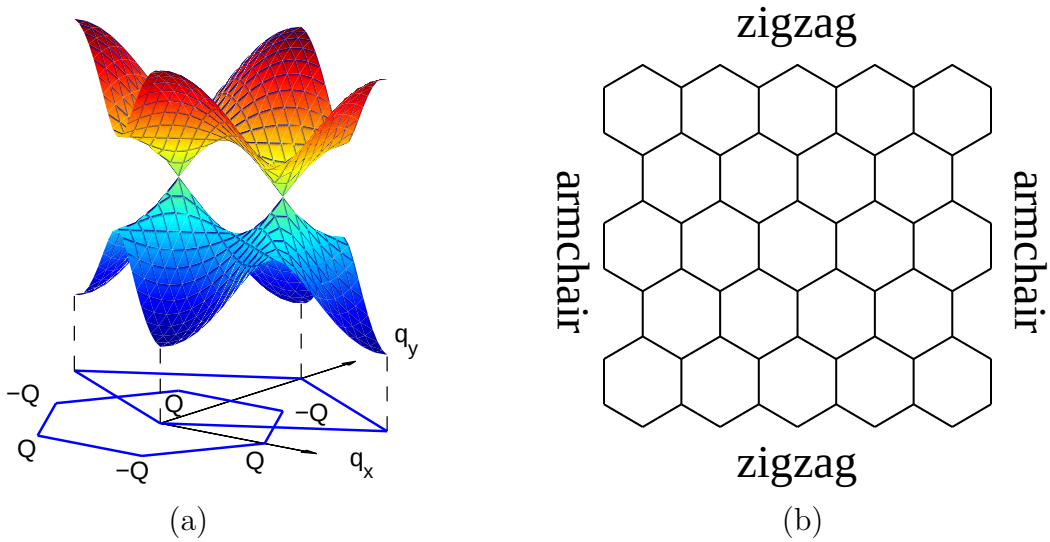
similar calculations to those used in the analysis of graphene. We therefore present an introduction to graphene both in the clean system and with disorder.

Graphene consists of a single layer of carbon atoms covalently bonded in a hexagonal lattice with $sp_2$ hybridised orbitals. These bonds are strong and form a deep, filled valence band. The remaining p orbitals lie out of the plane and covalently bond, forming a $\pi$ band. This band has a single electron per atom and so is half filled. Introduction of pentagons or heptagons into the hexagonal lattice leads to a local curvature and with an appropriate number of pentagons graphene can even be wrapped into a ball, as in the fullerenes. Graphene can also be wrapped to form a carbon nanotube. These effects are illustrated in Figure1.7 (a), (b) and (c) respectively.

An investigation into the electronic properties of graphene may use as its starting point a tight binding model in the non-interacting limit, where electrons simply hop between nearest neighbour atoms. Let $a^\dagger_{j,\sigma}$ ($a_{j,\sigma}$) be the creation (annihilation) operators for an electron with spin $\sigma$ on site $j$. The tight binding Hamiltonian is

$$H = -t \sum_{\langle jk \rangle, \sigma} \left( a^\dagger_{j,\sigma} a_{k,\sigma} + \text{h.c.} \right). \tag{1.22}$$

The sites of the hexagonal lattice may be identified with one of two sublattices: A or B. The nearest neighbour hopping in Eq. (1.22) only connects sites on opposite sublattices and is hence termed bipartite. We note an key feature of bipartite tight binding models that will be important in our discussion of the Kitaev honeycomb model: their eigenstates are particle-hole symmetric, with eigen-energies occurring in $\pm E$ pairs. Furthermore, the tight binding model of graphene has two zero energy points in the first Brillouin zone at




(a) (b)

Figure 1.8: a) The spectrum, 1st Brillouin zone of the tight binding Hamiltonian that represents electron hopping in graphene. There are two in-equivalent Dirac points in the 1st Brillouin zone at $\pm\mathbf{Q}$. b) Two types of edge in graphene: zigzag and armchair.

$\pm\mathbf{Q}$, as shown in Figure 1.8(a). Around these points the spectrum is asymptotically linear, with a vanishing density of states. The zero energy points at are thus termed Dirac points and the elementary excitations take on a valley index to indicate which of the two Dirac points they refer to. Fermions with a linear spectrum are termed Dirac fermions; the low energy excitations are chiral since they are derived from a parent state with momentum $\pm\mathbf{Q}$ and will therefore have a momentum approximately equal to $\pm\mathbf{Q}$; and there is no gap to excitations. The low energy excitations are thus termed massless, chiral, Dirac fermions.

Many interesting features emerge from this primitive description of graphene. For instance, the low energy physics of graphene bears many similarities to that of massless fermions in quantum electrodynamics, albeit with fermions that move at a speed about 300 times smaller than the speed of light. Since the band is half filled, the Fermi level lies exactly at the Dirac point, where the density of states vanishes, and the system is termed a semi-metal. The chirality within each valley inhibits back scattering. In fact, a chiral fermion that approaches a potential barrier perpendicularly has a 100% transmission probability, even if the transmission is classically forbidden. This is a termed Klein transmission. For back scattering to occur, the approach angle must be non-perpendicular or the scattering potential must have non-zero matrix elements between eigenstates of different

valley indices.

With its deep valence band, the crystallographic stability of graphene means that it is relatively easy to obtain very pure samples, with little substitutional disorder. This is one of the reasons behind the very long mean free path of its electrons, which can be up to micrometers in present samples. Disorder is not absent however. Indeed, the Mermin-Wagner theorem informs us that there can be no long range order in isolated graphene as it is a truly two dimensional structure. In fact, graphene is susceptible to many topological deformations at finite temperature such as voids, cracks and pentagonal and square plaquettes. Charges on top of graphene and absorbed impurity atoms can also affect the electronic properties. Furthermore, the two dimensional surface formed by graphene has low stiffness and ripples and warping of the lattice are thus common. The electron hopping is governed by the overlap of the out-of-plane $\pi$ orbitals, which will be affected by changes in the real space surface of graphene. In turn, this will cause some position dependent disorder of the hopping parameter $t$ in Eq. (1.22).

Broad review articles covering the effects of the disorder in graphene can be found in Ref. [75, 76]. However, the properties of graphene with site dilution will be most relevent to the discussion in chapters 3 and 4 and it is on this that we now focus. In general, any sublattice imbalance will lead to zero energy states. For a lattice initially with equal numbers of sites on the A and B sublattice, let the number of atoms removed from the $A(B)$ sublattice be $N_{A(B)}$. The number of exact zero energy states of the tight binding model (1.22) will then be $|N_A - N_B|$. This has particular consequences for the edges of a finite sample. In Figure 1.8(b), we display two types of edge in graphene: zigzag and armchair. Armchair edges have no sublattice imbalance and do not lead to edge states. In contrast to this, zigzag edges have a sublattice imbalance and lead to zero energy edge states. The wavefunctions of these edge states decay with distance away from the edge, so that in a sample of finite size, states from opposite edges may hybridise, forming states with a non-zero energy.

In bulk graphene, introduction of a single vacancy leads a quasi-localised state at zero energy[74]. It has the three-fold symmetry of the lattice and the wavefunction amplitude decays as $1/r$ at large distances. Two vacancies, one on each sublattice, lead to two quasi-localised states of the above form that interact and form a hybridised state at finite energy. A finite density of vacancies leads to an impurity band with a divergent density of states at low energies. We shall see that these ideas are pertinent to our study of the Kitaev model with vacancies and we shall explore them further in chapter 4.

The tight binding model (1.22) does not include electron interactions and therefore may be of questionable use in describing the electronic properties of graphene. For in-

stance, proton irradiated samples of graphite have been shown to have a ferromagnetic (or ferrimagnetic) response with a Curie temperature above room temperature[29]. This observation cannot be accounted for by considering Eq. (1.22) only. This magnetic behaviour is predicted however, if electron interactions are included in the Hubbard model:

$$H_{t-U} = -t \sum_{\langle jk \rangle, \sigma} \left( a^{\dagger}_{j,\sigma} b_{k,\sigma} + \text{h.c.} \right) + U \sum_{j} n_{j,\uparrow} n_{j,\downarrow}. \tag{1.23}$$

A theorem by Lieb[56] has far reaching consequences for this model. For *any* bipartite lattice (it need not be periodic or indeed have any symmetry in the hopping at all) let there be $|A|(|B|)$ sites on the A(B) sublattice, with $|B| \geq |A|$. Also let the number of electrons be $|A| + |B|$ so that the system is half filled. The ground state of $H$ is then unique and has spin $S = \frac{1}{2}(|B| - |A|)$. This immediately implies that when graphene is selectively diluted on one sublattice it will develop a spontaneous magnetisation if the electron interactions can be approximated as an on-site repulsion, as in Eq. (1.23). In fact, this was the first natural model to predict itinerant electron ferromagnetism. Further study found that even if the sublattice dimensions are globally equal, with $|A| = |B|$, then around all vacancies and larger voids there develops a local spin texture that corresponds to local ferromagnetic or ferrimagnetic order depending on the spatial qualities of the void[72].

As for the Heisenberg antiferromagnets, we have seen that disorder can have far reaching consequences for the properties of graphene. In particular, a finite density of vacancies causes a pile up in the density of states at low energies. This completely changes the character of the low energy physics since pure graphene is a semi-metal with vanishing density of states at the Fermi level. Also, we have seen yet another example where disorder generates a local moment that can be polarised by an applied magnetic field. This will continue to be a theme throughout this thesis.

## 1.3 RVB, VBS and spin liquids

In the discussion of spin-$\frac{1}{2}$ and spin-1 HAF chains the notion of a resonating valence bond (RVB) liquids and valence bond solid (VBS) states was introduced. In this section we clarify these ideas and discuss their relation to spin liquid physics and topological degeneracy. For review articles, see Ref. [54, 65, 86] and references therein.

Finite temperature second order phase transitions are usually described by Landau theory, where the transition is accompanied by the breaking of a symmetry that is in turn quantified by an order parameter. For example, upon lowering the temperature, a Heisenberg ferromagnet on a cubic lattice undergoes a second order phase transition from

a high temperature, disordered phase with spin rotational symmetry to a low temperature, ordered phase with spontaneous magnetisation and long range order. The order parameter here is the spontaneous magnetisation and the phase transition is characterised by a set of critical exponents that describe how the order parameter changes as the system is tuned through the phase transition.

There are, however, some phases that are not well described by Landau theory: two phases can be separated by a phase transition that can occur without the generation of *any* local order parameter, so that the two phases are not differentiated by the change of any symmetry. We consider here two phases that are *always* separated by a phase transition, as distinguished from the liquid-gas transition, where there is no change in symmetry but where the transition may be evaded entirely on a path going around the critical point.

Instead, there emerges a new kind of order that describes a state and that is topological in nature. For example, a fractional quantum hall state is of this type. We will review a particular Hamiltonian that has both VBS and RVB phases and which has the topological order here mentioned: the quantum hard core dimer model (QHCD) on the triangular lattice[66, 78, 79]. We have already introduced a number of terms, which we will now clarify. A valence bond state is one in which spins on a lattice are paired to form singlets. An RVB state is a superposition of such valence bond states. If the pairings are short ranged, such that spins may only pair with their nearest neighbours, the valence bond state may be encoded as a nearest neighbour, hard core dimer covering on the lattice. A short range RVB liquid is a superposition of such nearest neighbour, hard core dimer coverings such that the state breaks no spin rotational or translational symmetry and has only short range spin correlations. Taking these dimer coverings as a basis set, it is then possible to write down a QHCD Hamiltonian that acts within the space of dimer coverings.

The study of QHCD models was re-energised after Anderson's suggestion that the cuprates could be understood in terms of RVB physics[7]. This led Rokhsar and Kivelson to consider a Hamiltonian for which, with a particular choice of parameters, the ground state was a short range RVB liquid[79]. Note that, whilst an invaluable step in understanding RVB physics, the QHCD Hamiltonian they constructed is far abstracted from the original 2D HAF spin Hamiltonian that is believed to describe the cuprates: for instance the Hilbert space dimension of dimer coverings is much smaller than the Hilbert space dimension of spin states. In the following RK Hamiltonian on the triangular lattice a dimer is represented by a solid line:

$$\hat{H} = -t\hat{T} + v\hat{V} = \sum_{j=1}^{N} -t \sum_{\alpha=1}^{3} \left( |\,\rangle\langle\,| + \text{h.c.} \right) + v \sum_{\alpha=1}^{3} \left( |\,\rangle\langle\,| + |\,\rangle\langle\,| \right) \quad (1.24)$$

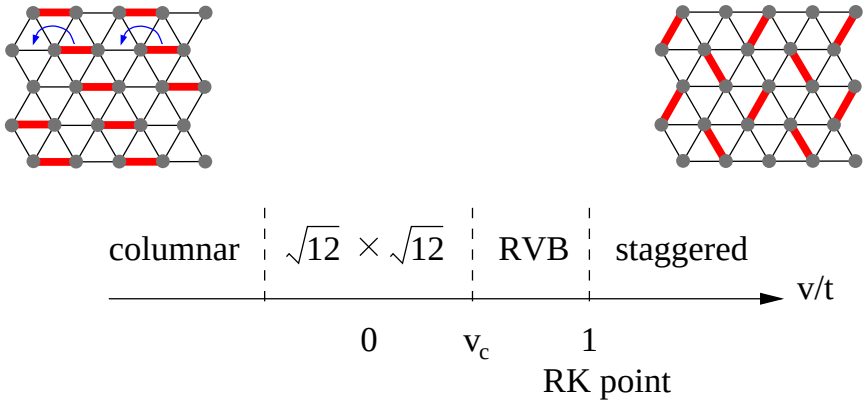



Figure 1.9: Phase diagram for the quantum hard core dimer model on the triangular lattice.

The sum on $j$ runs over the $N$ plaquettes of the lattice and the sum on $\alpha$ over the three orientations of the dimer plaquettes, i.e. △ rotated by 0° and ±60°. The Hamiltonian consists of a kinetic term $\hat{T}$ that flips plaquettes and a potential term $\hat{V}$. A plaquette is only flippable if it has parallel pairs of dimers, for which there is an energy cost $v$.

The dimer coverings on the triangular lattice form a linearly independent basis set $\{|c\rangle | c = 1, \ldots, N_c\}$, where $|c\rangle$ is one of $N_c$ hard-core dimer coverings on the triangular lattice. The number of flippable plaquettes $n_{fl}(c)$ in a particular covering is given by the eigenvalue of $\hat{V}$, so that $\hat{V}|c\rangle = n_{fl}(c)|c\rangle$. With periodic boundary conditions, two topologically distinct loops may be defined that traverse the system. A winding number can then be introduced that counts the number of dimers that cross each loop, with the parity determined by whether the winding is odd or even. The winding parity thus determines a topological sector. It can be checked easily that the Hamiltonian does not connect states of different parity as this involves rearrangements of $O(L)$ dimers, whereas the Hamiltonian (1.24) contains only local operations.

We now examine the phases that occur for different parameter regimes $v/t$, with the phase diagram shown in Figure 1.9. At the RK point $v/t = 1$ the Hamiltonian is exactly solvable[79] and the ground states $|RK\rangle$ are given by an equal weight superposition of all dimer coverings in a particular topological sector $|RK\rangle = N_c^{-1/2} \sum_{c=1}^{N_c} |c\rangle$. The ground state thus has a four fold topological degeneracy on a torus. That $|RK\rangle$ is a ground state of (1.24) can be demonstrated in the following manner. The Hamiltonian annihilates a non-flippable plaquette, whereas a flippable plaquette has, at best, energy $v - t$. The ground state energy is then $E_0 \geq min\{0, N(v-t)\}$. The state $|RK\rangle$ has energy $\langle RK|\hat{H}|RK\rangle = (v-t)\langle n_{fl}\rangle$. At the RK point this is clearly zero and so satisfies the lower bound for the ground state energy.

There are many definitions of what is termed a 'spin liquid', however, throughout this thesis, when referring to a spin liquid we shall mean a state that breaks no rotational or translational symmetry and has only short range spin correlations. At temperatures much greater than the exchange coupling, all spin systems will be in a thermal average of states that satisfy the above conditions but normally one would not refer to these as being a spin liquid, rather, one would call them paramagnets. In the opposite limit, where temperature is much less than exchange, typically a system will be in some (anti)ferromagnetically ordered state. Spin liquids on the other hand do not order at any temperature.

The above ground states $|RK\rangle$ break no spin rotational symmetry, have short range spin correlations and exponentially decaying dimer correlations and are therefore RVB spin liquids. In fact, for $v_c \leq v \leq t$ the ground state is an RVB liquid[77].

For $v/t > 1$ the lower bound above is satisfied by the staggered states with no flippable plaquettes, which are thus degenerate ground states in this parameter space. For each state, spin correlations are still short range, although there is now a long range singlet order parameter. This state is an example of a valence bond solid.

In the limit $v/t = -\infty$ the kinetic term $\hat{T}$ is insignificant and the energy is minimised by states that maximise the number of flippable plaquettes. These are the columnar states, their symmetry related counter parts and those states reached by, for example, moves shown in Figure 1.9, where all valence bonds on one row are moved to the left (or right) as indicated. For large but finite $v/t \ll -1$ a quantum order by disorder transition occurs and the columnar state as drawn is the ground state configuration. At $v = 0$ a crystalline ground state emerges with a 12 site unit cell, which is expected to be stable in some region around $v = 0$.

## 1.4 Quantum computation

Much of the body of work on the Kitaev Honeycomb model has been focused on its use as a quantum computer. The work in this thesis is instead centered around its behaviour as an exactly solvable spin liquid. However, as some of the results we present have ramifications for quantum computations, we give a *very* brief introduction into the basics of topological quantum computation. For a review, see Ref. [69] and references therein.

In (3+1)D there is only one topologically distinct way to exchange two indistinguishable particles twice and performing this double exchange is equivalent to doing nothing (the identity operator). See Figure 1.10 for a graphical illustration. If we define an exchange operator $\sigma$ that swaps two particles clockwise, this implies that $\sigma^2 = 1$ and the only eigenvalues of $\sigma$ must be $\pm 1$ corresponding to bosons and fermions. Note that this already

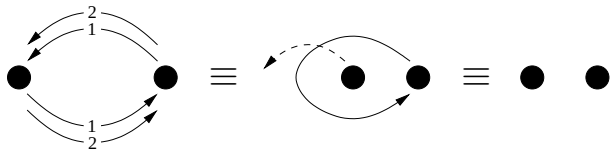



Figure 1.10: Double exchange of indistinguishable particles in (3+1)D is topologically the same as doing nothing, leading to Bose and Fermi statistics for particles in (3+1)D.

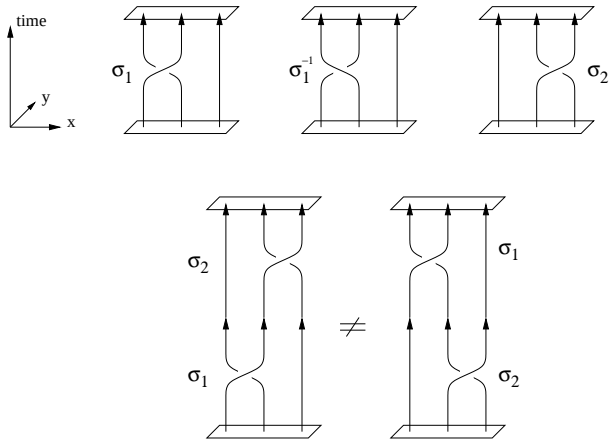



Figure 1.11: Top: Two elementary braid group elements on three particles, $\sigma_1$ and $\sigma_2$. The inverse operation of $\sigma_1$ is also shown. Bottom: The braid group is non-abelian as demonstrated here by showing $\sigma_1\sigma_2 \neq \sigma_2\sigma_1$.

produces such remarkable effects as the Pauli principle for fermions and condensation into a superfluid for bosons. In (1+1)D particle statistics are undefined and hardcore bosons are equivalent to fermions.

In (2+1)D particle statistics are more complex. Specifically, moving one indistinguishable particle around another cannot be adiabatically transformed into the identity operator. Therefore, upon single exchange, particles can pick up an arbitrary phase:

$$\psi(\mathbf{r}_1, \mathbf{r}_2) \rightarrow e^{i\theta}\psi(\mathbf{r}_1, \mathbf{r}_2). \tag{1.25}$$

If $\theta$ does not equal 0 (bosons) or $\pi$ (fermions) the particles are termed 'anyons'. Consider a set of $N$ particles at sites $\mathbf{R}_1, \mathbf{R}_2, \ldots, \mathbf{R}_N$ and perform a series of two particle exchanges such that the particles end up back at sites $\mathbf{R}_1, \mathbf{R}_2, \ldots, \mathbf{R}_N$, the different topological classes of trajectories are in one to one correspondence with the braid group $\mathcal{B}_N$. Exchanging two particles is implemented by acting on the state with the corresponding element of the braid group. An example is shown in Figure 1.11

The correct representation of the braid group must be chosen to implement the statistics of the particles. Operations on abelian anyons are implemented with the one dimensional

representation of the braid group, so that exchanging two particles changes the phase of the state by an amount $\theta$ whose only constraint is to be a rational fraction of $2\pi$. Non-abelian statistics are implemented with a higher dimensional representation of the braid group: unitary matrices, which are generically non-abelian. Non-abelain anyons can occur if a system has a degenerate set of $g$ states with particles at fixed positions $\mathbf{R}_1, \mathbf{R}_2, \ldots, \mathbf{R}_N$. Defining an orthonormal basis $\psi_\alpha, \alpha = 1, 2, \ldots, g$, of these states, an element of the braid group $\sigma_i$ is represented by a $g \times g$ matrix $\rho(\sigma_i)$ that performs a non-trivial rotation on a particular state

$$\psi_\alpha \to [\rho(\sigma_i)]_{\alpha\beta}\psi_\beta \tag{1.26}$$

Anyons are best considered a kind of topological defect that can only be annihilated by fusion with another anyon. An analogy would be vortices in the order parameter of a classical x-y model, the Kosterlitz-Thouless phase. Even if fluctuations disrupt the local order parameter, the topology remains and a vortex can only be annihilated with an anti-vortex. In fact, it is only topological operations that have non-zero matrix elements within the degenerate $g$ dimensional subspace: they are the braid group elements already discussed. All non-trivial local operators have matrix elements equal to zero within this space. This includes operators that usually cause decoherence in quantum computers, such as phonon coupling and it is this resistance to error that makes topological quantum computation so attractive.

To describe anyons in this way the system must necessarily be gapped, so that correlations decay exponentially and it must also have a topologically degenerate ground state. If it is not gapped, then quasi particles may not be localised and braiding operations are not well defined. Quantum computation requires the following three steps: initialisation, computation and measurement. We address each in turn.

Initialisation: A particular state can be initialised by pulling particle, antiparticle pairs from the vacuum. They must have conjugate quantum numbers since the total quantum number must be the same as the vacuum. This gives a known initial state on which computations can be performed.

Computation: If the braid group is rich enough, then any quantum gate can be implemented with the correct sequence of braid group operations, which are themselves performed by physically dragging the quasi particles around. This must be done adiabatically, so that the system remains in the $g$ dimensional ground state manifold.

Measurement: The final state of the system must then be measured to find the result of the quantum computation. This can be done either by bringing the quasi particles together and measuring the energy change, which is dependent on the state, or by using a quantum analog of a Fabry-Perot interferometer. In the latter, a beam of quasi-particles is split, one

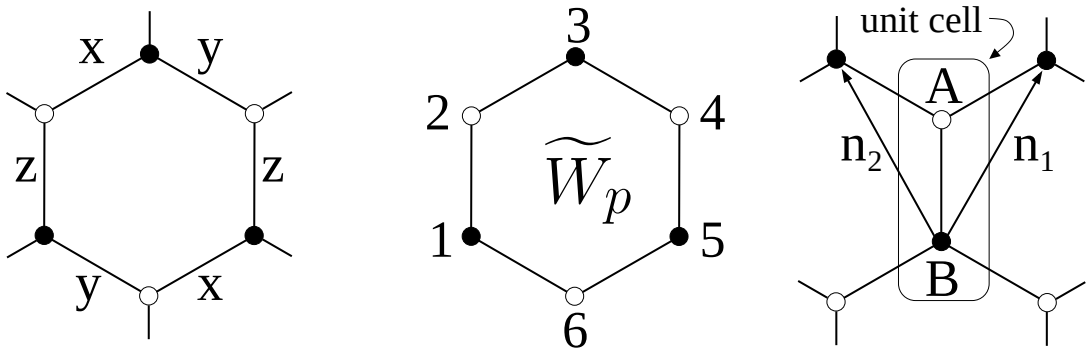
sent around the group of test particles and then re-interfered with the other. The resulting interference pattern is dependent on the quantum numbers of the test particles and hence can be used as a readout of the computation.

To date the only evidence, even indirect, for anyonic states has been those of the fractional quantum Hall effect. In the next chapter we shall see that the Kitaev honeycomb model is a system that can be tuned to have both abelian or non-abelian anyons and has thus attracted much interest in this field, particularly as there are now several proposals for an experimental realisation.

# Chapter 2

# The model

Having seen some examples of how disorder can affect the properties of strongly correlated electron systems, we leave the general introduction behind and now turn to the subject of this thesis: the Kitaev honeycomb model. This chapter comes in three parts. The first is a review and expansion of Kitaev's work, describing the model and the technical details leading to its exact solvability. The second is an exploration of the properties of the clean system and proposals for experimental realisations of the Hamiltonian. Finally, we anticipate the remainder of this thesis and provide an outline of the types of disorder that we consider in the Kitaev model.




(a) (b) (c)

Figure 2.1: (a) Three types of bond in the honeycomb lattice. (b) The site labels used to define the non-dynamical observables $\widetilde{W}_p$. (c) Unit cell, primitive lattice vectors and sublattice convention used through this thesis.

The model was introduced in a seminal work by Kitaev[52], where he described in great detail many of its properties and particularly its use in topological quantum computation. In general we shall be concerned, however, with its spin liquid behaviour. The Kitaev

honeycomb model is a spin-$\frac{1}{2}$ Hamiltonian, where the spins lie on the sites of the honeycomb lattice and have nearest neighbour exchange interactions of Ising type. We represent a spin-$\frac{1}{2}$ by the Pauli matrices $\tilde{\sigma}^{\alpha}$, for $\alpha = x, y, z$. On the honeycomb lattice one can define three types of bond $x$, $y$ and $z$, as shown in Figure 2.1(a). The special feature of the Kitaev model is that the spin components are coupled by an exchange that depends on the bond type, such that the exchange coupling between sites $j$ and $k$ is given by $J_{\alpha_{jk}} \tilde{\sigma}_j^{\alpha_{jk}} \tilde{\sigma}_k^{\alpha_{jk}}$, where $\alpha_{jk} = x, y$ or $z$. The Hamiltonian is

$$\widetilde{H} = -J_x \sum_{\text{x-links}} \tilde{\sigma}_j^x \tilde{\sigma}_k^x - J_y \sum_{\text{y-links}} \tilde{\sigma}_j^y \tilde{\sigma}_k^y - J_z \sum_{\text{z-links}} \tilde{\sigma}_j^z \tilde{\sigma}_k^z \ . \tag{2.1}$$

It is very rare to find an exactly solvable, two dimensional spin Hamiltonian. However, Kitaev showed that there exist a set of non-dynamical, commuting observables defined on each plaquette that allow the Hamiltonian to be brought into block diagonal form. Remarkably, within each block the Hamiltonian can then be written as a bi-linear in fermion operators and solved exactly. Using the site labelling convention defined in Figure 2.1(b) the observables are $\widetilde{W}_p \equiv \tilde{\sigma}_1^x \tilde{\sigma}_2^y \tilde{\sigma}_3^z \tilde{\sigma}_4^x \tilde{\sigma}_5^y \tilde{\sigma}_6^z$. It is easy to show that $[\widetilde{W}_p, \widetilde{H}] = 0$ and to check that $[\widetilde{W}_p, \widetilde{W}_{p'}] = 0$. The Hilbert space of $\widetilde{H}$ can be separated into sectors $\mathcal{L}_{\{\widetilde{W}_p\}}$ corresponding to the set of eigenvalues of each $\widetilde{W}_p$, and the Hamiltonian may be diagonalised within the reduced Hilbert space of $\mathcal{L}_{\{\widetilde{W}_p\}}$. The total Hilbert space is then

$$\mathcal{L} = \bigoplus_{\{\widetilde{W}_p\}} \mathcal{L}_{\{\widetilde{W}_p\}}. \tag{2.2}$$

Since $\widetilde{W}_p^2 = 1$, the eigenvalues of $\widetilde{W}_p = \pm 1$. Later we shall see that it is appropriate to think of $\widetilde{W}_p$ as the $\mathbb{Z}_2$ flux through the plaquette. The choice $\{\widetilde{W}_p\}$ is therefore termed a flux sector. In a system with $N$ unit cells, as defined in Figure 2.1(c), and with periodic boundary conditions, there are $2N$ sites and $N$ plaquettes. Therefore the Hilbert space dimension within a particular sector is $\sim 2^{2N}/2^N \sim 2^N$. This is a dramatic reduction but nevertheless it is still exponentially large in system size. However, the nature of the interactions permits a further reduction to a free fermion problem that can then be solved exactly. There are a number of spin fractionalisation techniques that can be used to solve the Kitaev Hamiltonian, including Jordan Wigner transformation[31, 93] but we shall use that originally posed by Kitaev: a transformation to Majorana fermions.

## 2.1 Majorana fermions and spin Hamiltonians

In 1937 Ettore Majorana showed that a modified Dirac equation permits real solutions[60]: particles that have the curious property of being their own antiparticle. This is an unfamiliar concept. Nevertheless, there is strong theoretical evidence that neutrinos are Majorana

fermions[87] and in solid state physics Majoranas are widely believed to be a good hope for realising a quantum computer[52]. We will, however, be using Majoranas as a convenient mathematical tool that facilitates the exact solution of the Kitaev honeycomb model.

Majorana fermions $c_{2j-1}, c_{2j}$ may be thought of as the real and imaginary parts of a complex fermion $a_j^\dagger$, satisfying the following commutation relations

$$\begin{array}{cccc} c_{2j} = a_j + a_j^\dagger & & c_{2j-1} = i\left(a_j^\dagger - a_j\right) \\ c_j^2 = 1 & c_j c_k = -c_k c_j & j \neq k \ . \end{array} \tag{2.3}$$

For complex fermions one is able to define a vacuum state $|0\rangle$ such that $a_j|0\rangle = 0$ for all fermion annihilation operators $a_j$ in the system. This is not possible for Majorana fermions. Therefore, when evaluating matrix elements we will always transform back into the more familiar complex fermions.

There are two independent Majorana fermions per complex fermion, each with a notional Hilbert space dimension $\sqrt{2}$. A spin can be described by four Majorana fermions $b^x, b^y, b^z, c$ such that $\tilde{\sigma}_j^\alpha = i b_j^\alpha c_j$. This correctly reproduces the spin commutation relations $\left\{\tilde{\sigma}_j^\alpha, \tilde{\sigma}_j^\beta\right\} = 2\delta_{\alpha\beta}$ and $\left[\tilde{\sigma}_j^\alpha, \tilde{\sigma}_k^\beta\right] = 0$ for $j \neq k$ but since there are four Majorana fermions, the size of the Hilbert space per spin is doubled from two to $\sqrt{2}^4 = 4$. To emphasize this change in Hilbert space dimension we mark operators in the physical spin space with a tilde and those in the space of Majoranas without. A constraint must be introduced to define the allowed physical states. To this end, introduce a new operator $\widetilde{D_j} \equiv -i\tilde{\sigma}_j^x \tilde{\sigma}_j^y \tilde{\sigma}_j^z = 1$. When written in Majoranas it becomes $D_j = b_j^x b_j^y b_j^z c$. The operator $D_j^2 = 1$ so that $D_j$ has eigenvalues $\pm 1$. A physical eigenstate $|\Phi\rangle$ of a Majorana Hamiltonian therefore must have $D_j|\Phi\rangle = |\Phi\rangle$ for all $j$. A simple way to ensure this is to use a projection operator

$$\mathcal{P} = \prod_j \left(\frac{1 + D_j}{2}\right) \tag{2.4}$$

such that physical states of the system are given by $|\Phi_\mathcal{P}\rangle = \mathcal{P}|\Phi\rangle$. It is clear that $[D_i, D_j] = 0$. Therefore $D_j \mathcal{P}|\Phi\rangle = \mathcal{P}|\Phi\rangle$ for all $j$, so satisfying the condition on a physical state. The operators $D_j$ commute with $\sigma_j^\alpha$ and therefore with *all* spin Hamiltonians written in terms of Majoranas. We shall see that this procedure naturally leads to a degeneracy in the states $|\Phi\rangle$ and that there are many states that project onto the same physical state $|\Phi_\mathcal{P}\rangle$.

## 2.2 Exact solubility and projection

The above spin fractionalisation technique may now be applied directly to the Hamiltonian (2.1). As an example we show the formation of the Marjorana terms on an x-link, with the

terms on y and z links generated in an analogous manner:

$$-J_x\sigma_j^x\sigma_k^x = -J_x ib_j^x c_j ib_k^x c_k = J_x(ib_j^x b_k^x)ic_j c_k \equiv iJ_x\hat{u}_{jk}c_j c_k$$
$$H_{\hat{u}} = i\sum_{j\in A,k\in B,\langle jk\rangle} J_{\alpha_{jk}}\hat{u}_{jk}c_j c_k \ , \tag{2.5}$$

where $\hat{u}_{jk} \equiv ib_j^{\alpha_{jk}} b_k^{\alpha_{jk}}$ and the sum is over nearest neighbour sites $j$ on the $A$ sublattice and $k$ on the $B$ sublattice, as defined in Figure 2.1(c). It can be checked explicitly that all operators $D_j$ commute with $H_{\hat{u}}$. Since there are $2N$ sites, there are $2N$ operators $D_j$ and eigenstates of $H_{\hat{u}}$ are therefore $2^{2N}$-fold degenerate. The degenerate states are related by the action of operators $D_j$ on some reference state $|\Phi\rangle$ in the following manner. For any set $\{D_1, D_2, \ldots D_m\}$

$$|\Phi'\rangle = \left(\prod_{\{D_1,D_2,\ldots D_m\}} D_j\right)|\Phi\rangle \qquad |\Phi_{\mathcal{P}}\rangle = \mathcal{P}|\Phi'\rangle = \mathcal{P}|\Phi\rangle. \tag{2.6}$$

Each of these $2^{2N}$ related states project onto the same physical state.

The operators $\hat{u}_{jk}$ commute with each other and with the Hamiltonian $H_{\hat{u}}$. Since $\hat{u}_{jk}^2 = 1$, the eigenvalues of $\hat{u}_{jk} = \pm 1$. The original spin Hamiltonian was block diagonalisable into flux sectors and a similar procedure can be performed here, where the Hamiltonian is block diagonalisable into eigenspaces of the set $\{u_{jk}\}$. By choosing a particular set of $\{\hat{u}_{jk}\}$ and 'removing hats', setting $\{u_{jk}\} = \pm 1$, the Hamiltonian can be reduced to a bilinear in Majorana operators :

$$H_u = \frac{i}{2}\left(c_A^T c_B^T\right)\begin{pmatrix} 0 & M \\ -M^T & 0 \end{pmatrix}\begin{pmatrix} c_A \\ c_B \end{pmatrix}. \tag{2.7}$$

$M$ is an $N \times N$ matrix with elements $M_{jk} = J_{\alpha_{jk}}u_{jk}$ and $c_{A(B)}$ is a vector of length $N$ of Majorana operators on the $A(B)$ sublattice. The three Hamiltonians introduced so far $\widetilde{H}, H_{\hat{u}}$ and $H_u$ are related by non-trivial transformations, act in different Hilbert spaces and should not be confused. For instance their Hilbert space dimensions are $2^{2N}, 2^{4N}$ and $2^N$ respectively.

The Hamiltonian (2.7) can now be diagonalised and solved exactly. Quite generally, this can be done using a singular value decomposition $M = USV^T$, where $U$ and $V$ are $N \times N$ orthogonal matrices and $S$ is an $N \times N$ positive semidefinite diagonal matrix. With lattice vectors $\mathbf{n}_1, \mathbf{n}_2$ shown in Figure 2.1(c), label the unit cell by $\mathbf{r} = n_1\mathbf{n}_1 + n_2\mathbf{n}_2$ and the two Majorana fermions within it $c_{A,\mathbf{r}}$ and $c_{B,\mathbf{r}}$. Further define Majorana fermions $c'_{A,m} = \sum_{\mathbf{r}} U^T_{m,\mathbf{r}}\ c_{A,\mathbf{r}}$ and $c'_{B,m} = \sum_{\mathbf{r}} V^T_{m\mathbf{r}}\ c_{B,\mathbf{r}}$ and complex fermions $a_m^\dagger = \frac{1}{2}\left(c'_{A,m} - ic'_{B,m}\right)$

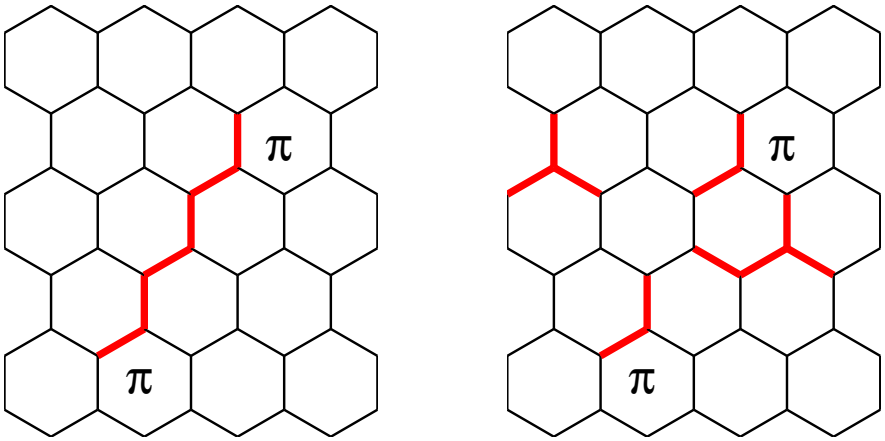



Figure 2.2: Two different gauge choices for $\{u_{ij}\}$ that lead to the same flux sector. $u_{ij} = +1$ shown in black, $u_{ij} = -1$ shown in red.

and $a_m = \frac{1}{2}\left(c'_{A,m} + ic'_{B,m}\right)$, giving

$$\begin{aligned} H_u &= \tfrac{i}{2}\left(c_A^T c_B^T\right)\begin{pmatrix} U & 0 \\ 0 & V \end{pmatrix}\begin{pmatrix} 0 & S \\ -S & 0 \end{pmatrix}\begin{pmatrix} U^T & 0 \\ 0 & V^T \end{pmatrix}\begin{pmatrix} c_A \\ c_B \end{pmatrix} \\ &= \tfrac{i}{2}\left(c_A'^T c_B'^T\right)\begin{pmatrix} 0 & S \\ -S & 0 \end{pmatrix}\begin{pmatrix} c'_A \\ c'_B \end{pmatrix} \\ &= i\sum_{m=1}^{N} S_m c'_{A,m} c'_{B,m} \\ &= \sum_{m=1}^{N} S_m\left(2a_m^\dagger a_m - 1\right). \end{aligned} \tag{2.8}$$

Using the site labelling in Figure 2.1(b) and in terms of Majorana operators, the flux through an elementary plaquette $W_p = u_{21}u_{23}u_{43}u_{45}u_{65}u_{61} = \pm 1$. It is now clear that $W_p$ is the flux through a plaquette in the Aharonov-Bohm sense that a particle traversing a loop going around the plaquette picks up a phase $\pm 1$, so that the flux through that plaquette is 0 or $\pi$. Physical properties of the system depend only on the flux sector but there are many distinct sets $\{u_{ij}\}$ that give rise to the same flux sector, with an example shown in Figure 2.2. This is a consequence of the transformation to Majorana operators, which has increased the size of the Hilbert space and led to the emergence of a $Z_2$ gauge degree of freedom at each lattice site in the Hamiltonian $H_u$. Using a variable $\theta_j = \pm 1$ on each lattice site, the gauge transformations are implemented as $c_j \to \theta_j c_j$ and $u_{jk} \to \theta_j u_{jk}\theta_k$. As expected for a $Z_2$ gauge theory, the gauge transformations do not change the flux sector.

To further our efforts in understanding the effects of the projection operator, it will be instructive to form complex fermions from the Majoranas $b^x, b^y, b^z, c$: with sites $j, k$ nearest

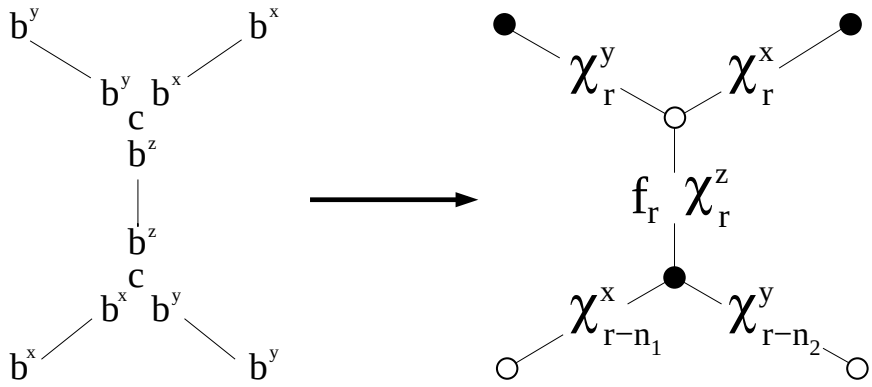



Figure 2.3: The re-fermionization of Majorana fermions to complex fermions. Variables $\chi^{\alpha}_{\mathbf{r}}$ are located on the bonds of the lattice and $f_{\mathbf{r}}$ in the unit cells.

neighbours and with site $j$ on sublattice $A$ in the unit cell at $\mathbf{r}$, define new variables[11, 93]

$$\begin{aligned} \chi^{\alpha}_{\mathbf{r}} &= \tfrac{1}{2}\left(b_j^{\alpha_{jk}} + i b_k^{\alpha_{jk}}\right) \qquad (\chi^{\alpha}_{\mathbf{r}})^{\dagger} = \tfrac{1}{2}\left(b_j^{\alpha_{jk}} - i b_k^{\alpha_{jk}}\right) \\ f_{\mathbf{r}} &= \tfrac{1}{2}\left(c_{A,\mathbf{r}} + i c_{B,\mathbf{r}}\right) \qquad f^{\dagger}_{\mathbf{r}} = \tfrac{1}{2}\left(c_{A,\mathbf{r}} - i c_{B,\mathbf{r}}\right). \end{aligned} \tag{2.9}$$

$\chi^{\alpha}_{\mathbf{r}}$ are located on the bonds of the lattice and $f_{\mathbf{r}}$ in the unit cells, as shown in Figure 2.3. In this notation $\hat{u}_{jk} \equiv i b_j^{\alpha_{jk}} b_k^{\alpha_{jk}} = 2\left(\chi^{\alpha}_{\mathbf{r}}\right)^{\dagger}\chi^{\alpha}_{\mathbf{r}} - 1$. Eigenstates of $H_{\hat{u}}$ (2.5) should be thought of as a direct product of gauge degrees of freedom $|\chi\rangle$ and a matter field $|f\rangle$: $|\Phi\rangle = |\chi\rangle \otimes |f\rangle$. The eigenvalues of $|\chi\rangle$ determine the flux sector and gauge, and $|f\rangle$ is an eigenstate of the Hamiltonian $H_u$ (2.7), which takes the following form:

$$H_u = \begin{pmatrix} f^{\dagger} & f \end{pmatrix} \begin{pmatrix} M_A & M_S \\ -M_S & -M_A \end{pmatrix} \begin{pmatrix} f^{\dagger} \\ f \end{pmatrix} \qquad \begin{aligned} M_A &= \tfrac{1}{2}(M^T - M) \\ M_S &= \tfrac{1}{2}(M^T + M)\ , \end{aligned} \tag{2.10}$$

where $f^{\dagger}$ and $f$ are $N$ component vectors of creation and annihilation operators $f^{\dagger}_{\mathbf{r}}$ and $f_{\mathbf{r}}$. They are related to the excitations $a^{\dagger}_m$ in Hamiltonian (2.8) thus

$$f^{\dagger}_{\mathbf{r}} = \frac{1}{2}\left(U_{\mathbf{r},m} + V_{\mathbf{r},m}\right) a^{\dagger}_m + \frac{1}{2}\left(U_{\mathbf{r},m} - V_{\mathbf{r},m}\right) a_m\ . \tag{2.11}$$

In terms of the complex fermions $\chi$ and $f$, the operators $D_j$ now take different forms on the $A$ and $B$ sublattices:

$$\begin{aligned} D_{A,\mathbf{r}} &= (\chi^{x\ \dagger}_{\mathbf{r}} + \chi^{x}_{\mathbf{r}})(\chi^{y\ \dagger}_{\mathbf{r}} + \chi^{y}_{\mathbf{r}})(\chi^{z\ \dagger}_{\mathbf{r}} + \chi^{z}_{\mathbf{r}})(f^{\dagger}_{\mathbf{r}} + f_{\mathbf{r}}) \\ D_{B,\mathbf{r}} &= (\chi^{x\ \dagger}_{\mathbf{r}-\mathbf{n}_1} - \chi^{x}_{\mathbf{r}-\mathbf{n}_1})(\chi^{y\ \dagger}_{\mathbf{r}-\mathbf{n}_2} - \chi^{y}_{\mathbf{r}-\mathbf{n}_2})(\chi^{z\ \dagger}_{\mathbf{r}} - \chi^{z}_{\mathbf{r}})(f^{\dagger}_{\mathbf{r}} - f_{\mathbf{r}})\ . \end{aligned} \tag{2.12}$$

The projection operator can also be re-written as

$$\mathcal{P} = \left[1 + \sum_{\mu,\mathbf{r}} D_{\mu,\mathbf{r}} + \sum_{\mu,\mathbf{r}<\nu,\mathbf{r}'} D_{\mu,\mathbf{r}} D_{\nu,\mathbf{r}'} + \cdots + \prod_{\mu,\mathbf{r}} D_{\mu,\mathbf{r}}\right] 2^{-2N} \tag{2.13}$$

The operator $D_{A(B),\mathbf{r}}$ changes the bond fermion number on the three bonds attached to site $\mathbf{r}_{A(B)}$ but does not change the flux sector. It also acts on the matter state $|f\rangle$. Notice, however, that acting with $D_j$ on every site does not change the bond fermion number. Defining $D = \prod_j D_j$ and $\mathcal{P}'$ as the sum of all operators in $\mathcal{P}$ that change the bond fermion number in an inequivalent way and normalised by $1/2^{2N-1}$ since there are $2^{2N-1}$ terms in $\mathcal{P}'$, the projection operator can then be re-written[93] as $\mathcal{P} = \mathcal{P}'(1+D)/2$, where $D$ takes on the following form. With $N_\chi$ and $N_f$ the number of bond and matter fermions respectively

$$\begin{aligned} D = & \prod_{\mathbf{r}} \begin{array}{l} (\chi^{x\,\dagger}_{\mathbf{r}-\mathbf{n}_1} - \chi^{x}_{\mathbf{r}-\mathbf{n}_1})(\chi^{y\,\dagger}_{\mathbf{r}-\mathbf{n}_2} - \chi^{y}_{\mathbf{r}-\mathbf{n}_2})(\chi^{z\,\dagger}_{\mathbf{r}} - \chi^{z}_{\mathbf{r}})(f^\dagger_{\mathbf{r}} - f_{\mathbf{r}})\times \\ (\chi^{x\,\dagger}_{\mathbf{r}} + \chi^{x}_{\mathbf{r}})(\chi^{y\,\dagger}_{\mathbf{r}} + \chi^{y}_{\mathbf{r}})(\chi^{z\,\dagger}_{\mathbf{r}} + \chi^{z}_{\mathbf{r}})(f^\dagger_{\mathbf{r}} + f_{\mathbf{r}}) \end{array} \\ = & \prod_{\mathbf{r}} (\chi^{x\,\dagger}_{\mathbf{r}-\mathbf{n}_1} - \chi^{x}_{\mathbf{r}-\mathbf{n}_1})(\chi^{x\,\dagger}_{\mathbf{r}} + \chi^{x}_{\mathbf{r}})(\chi^{y\,\dagger}_{\mathbf{r}-\mathbf{n}_2} - \chi^{y}_{\mathbf{r}-\mathbf{n}_2})(\chi^{y\,\dagger}_{\mathbf{r}} + \chi^{y}_{\mathbf{r}})(2\chi^{z\,\dagger}_{\mathbf{r}}\chi^{z}_{\mathbf{r}} - 1)(2f^{z\,\dagger}_{\mathbf{r}} f^{z}_{\mathbf{r}} - 1) \end{aligned} \tag{2.14}$$

The product is over bilinears in $\chi^x$ and $\chi^y$ variables. Therefore the product over $\mathbf{r}$ can be ordered in such a way as to obtain the following terms

$$\begin{aligned} D = & \prod_{\mathbf{r}} (2\chi^{x\,\dagger}_{\mathbf{r}}\chi^{x}_{\mathbf{r}} - 1)(2\chi^{y\,\dagger}_{\mathbf{r}}\chi^{y}_{\mathbf{r}} - 1)(2\chi^{z\,\dagger}_{\mathbf{r}}\chi^{z}_{\mathbf{r}} - 1)(2f^{z\,\dagger}_{\mathbf{r}} f^{z}_{\mathbf{r}} - 1) \\ = & (-1)^{N_\chi}(-1)^{N_f} \ . \end{aligned} \tag{2.15}$$

In this form, it is clear that the projection operator annihilates states of odd total fermion number. The complex fermion Hamiltonian $H_u$ in Eq. (2.10) conserves fermion number modulo 2 and therefore commutes with $D$, which also commutes $H_{\hat{u}}$. Contrast this with $D_j$ that commutes with $H_{\hat{u}}$ but *not* with $H_u$.

To summarise, the projection operator either annihilates a state that has odd total fermion number or transforms a state with even total fermion number to an equal weight superposition of all terms in $\mathcal{P}$ that change bond fermion number in an inequivalent way[93]: the terms of $\mathcal{P}'$. Note that the Hamiltonian $H_{\hat{u}}$ and terms in $\mathcal{P}'$ do not change the parity of the total fermion number. Therefore, $H_{\hat{u}}$ may be block diagonalised into parts that act on on even and odd fermion number states. Furthermore, changing the gauge of $H_u$ does not change the spectrum but can change the fermion parity. Therefore, for any eigenstate of $H_{\hat{u}}$, there will be a projected physical state with the same energy. The restriction to even fermion number is overcome by simply changing the gauge. The same conclusions apply to thermal averages over physical states.

Having established the effects of the projection operator we will now show that for a large class of operators, expectation values evaluated using an eigenstate $|\Phi\rangle = |\chi\rangle \otimes |f\rangle$ of $H_{\hat{u}}$ are the same as those obtained using the projected physical states.

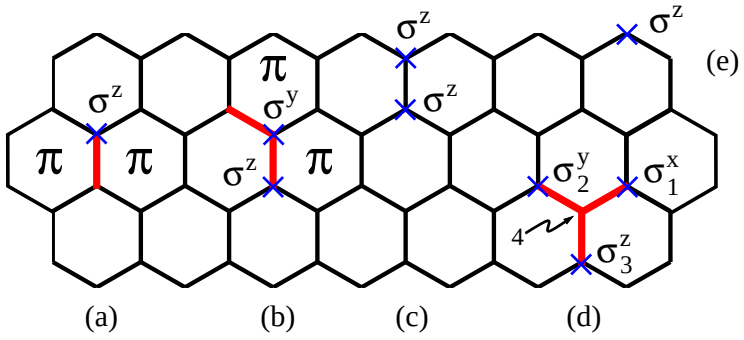



Figure 2.4: A graphical illustration of the final state that results from the action of various spin operators on an initial state $|\chi\rangle$ with all $\langle \hat{u}_{jk} \rangle = \langle 2\left(\chi^{\alpha}_{\mathbf{r}}\right)^{\dagger}\chi^{\alpha}_{\mathbf{r}} - 1\rangle = +1$. We denote final state values $u_{jk} = +1$ by black lines and $u_{jk} = -1$ by thick red lines. Spin operators act on both the gauge and matter fields but we illustrate here only the gauge fields. (a) A single spin operator $\sigma^{\alpha}_{j}$ changes the bond fermion number on a single bond and changes the flux sector, adding $\pi$ flux either side of the bond. (b) and (c) Nearest neighbour spin operators $\sigma^{\alpha}_{j}\sigma^{\beta}_{k}$ change the bond fermion number and flux sector if they are not of the form $\sigma^{\alpha_{jk}}_{j}\sigma^{\alpha_{jk}}_{k}$. (d) A three spin operator that changes bond fermion number but not the flux sector and whose action can by undone by the term $D_4$ in $\mathcal{P}'$. Care must be taken with operators of this type as the terms in $\mathcal{P}'$ also act on the matter sector $|f\rangle$. (e) At the edge of the lattice with open boundary conditions, spin operators do not necessarily change the flux sector.

It is immediately apparent that if an operator $\hat{\mathcal{O}}$ changes the fermion numbers on the bonds in a manner that cannot be undone by a term in $\mathcal{P}'$ then its expectation value is zero. This is a statement about the bond fermion part of the wavefunction only. It is the case for a single spin operator, for which $\sigma^{\alpha}_{A,\mathbf{r}} = ib^{\alpha}_{A,\mathbf{r}}c_{A,\mathbf{r}} = i(\chi^{\alpha}_{\mathbf{r}}{}^{\dagger} + \chi^{\alpha}_{\mathbf{r}})(f^{\dagger}_{\mathbf{r}} + f_{\mathbf{r}})$. A two spin operator that is not nearest neighbour and in the direction of the bond also has zero expectation value: if $\hat{\mathcal{O}} = \sigma^{\beta}_{j}\sigma^{\gamma}_{k}$ then $\langle\hat{\mathcal{O}}\rangle = 0$ in the ground state unless $j$ and $k$ are nearest neighbours and $\beta = \gamma = \alpha_{jk}$. The Kitaev honeycomb model therefore has strictly nearest neighbour spin correlations and is termed a spin liquid[11]. The effects of the operators mentioned above are illustrated graphically in Figure 2.4.

For simplicity, it is desirable to calculate matrix elements using an eigenstate $|\Phi\rangle = |\chi\rangle \otimes |f\rangle$. It is only sensible to do so if these matrix elements are the same as those obtained using the projected physical states. Throughout this paper we will consider operators $\hat{\mathcal{O}}$ that do not change the bond fermion number, which includes the Hamiltonian and types

(c) and (e) in Figure 2.4. In these cases

$$\begin{aligned}
\frac{\langle\Phi|\mathcal{P}\hat{\mathcal{O}}\mathcal{P}|\Phi\rangle}{\langle\Phi|\mathcal{P}\mathcal{P}|\Phi\rangle} &= \frac{\langle\Phi|\hat{\mathcal{O}}\mathcal{P}|\Phi\rangle}{\langle\Phi|\mathcal{P}|\Phi\rangle} && \text{all spin operators commute with } \mathcal{P} \\
&= \frac{\langle\Phi|\hat{\mathcal{O}}(1+D)|\Phi\rangle}{\langle\Phi|(1+D)|\Phi\rangle} && \text{only the identity part of } \mathcal{P}' \text{ does not change the bond fermion number} \\
&= \frac{\langle\Phi|\hat{\mathcal{O}}|\Phi\rangle}{\langle\Phi|\Phi\rangle} && |\Phi\rangle \text{ is also an eigenstate of } D
\end{aligned} \tag{2.16}$$

For operators of this type we are thus free to evaluate matrix elements using an unprojected eigenstate and obtain the same result as when we use the projected physical states.

Operators that do change bond fermion number but in a gauge like way are more complicated: when this change is undone by a term in $\mathcal{P}'$ additional $c$ operators that are introduced must be taken into account. As an example, let us consider the operator $\hat{\mathcal{O}} = \sigma_1^x\sigma_2^y\sigma_3^z$, where the site labels are those used in Figure 2.4(d)

$$\begin{aligned}
\frac{\langle\Phi|\mathcal{P}\hat{\mathcal{O}}\mathcal{P}|\Phi\rangle}{\langle\Phi|\mathcal{P}\mathcal{P}|\Phi\rangle} &= \frac{\langle\Phi|\hat{\mathcal{O}}\mathcal{P}|\Phi\rangle}{\langle\Phi|\mathcal{P}|\Phi\rangle} && \text{all spin operators commute with } \mathcal{P} \\
&= \frac{\langle\Phi|\hat{\mathcal{O}}D_4(1+D)|\Phi\rangle}{\langle\Phi|(1+D)|\Phi\rangle} && \text{In conjunction with } \hat{\mathcal{O}}\text{, only the } D_4 \text{ part of } \mathcal{P}' \text{ does not change the bond fermion number} \\
&= \frac{\langle\Phi|\hat{\mathcal{O}}D_4|\Phi\rangle}{\langle\Phi|\Phi\rangle} && |\Phi\rangle \text{ is also an eigenstate of } D
\end{aligned} \tag{2.17}$$

We will not consider operators of this type in this thesis.

The energy levels $S_m$ in Eq. (2.8) may be found by considering a tight binding model with real hopping

$$\begin{pmatrix} 0 & M \\ M^T & 0 \end{pmatrix}, \tag{2.18}$$

which has eigenvalues $\pm S_m$. Throughout this thesis we will construct a Majorana hopping model that correctly represents the disorder configuration under consideration and then use the above tight binding model to find its ground state energy and excitations. This procedure is of particular use when finding the ground state energy of a finite sized lattice: it involves finding the singular values of an $N \times N$ matrix $M$, compared with the original spin Hamiltonian, which involves finding the eigenvalues of a $2^{2N}$ matrix.

## 2.3 Properties of the clean system

We have seen in Eq. (2.8) that the Kitaev Hamiltonian in a particular flux sector may be brought into diagonal form $\sum_{j=1}^{N} S_j \left(2a_j^\dagger a_j - 1\right)$. The ground state energy within this flux sector is then $-\sum_j S_j$. To find the global ground state energy, the correct flux sector must be chosen such that $\sum_j S_j$ is maximised. For a translationally invariant system, this is flux free[57]. The spectrum may be found by choosing a gauge in which all $u_{ij} = +1$ and using Fourier transform to diagonalise the tight binding model. In the momentum representation we define complex fermion operators $a_{\mathbf{q}}^\dagger$ and a momentum space Hamiltonian:

$$\begin{aligned} a'_{\mathbf{q}} &= \frac{1}{2\sqrt{N}} \sum_{\mathbf{r}} e^{i\mathbf{q}.\mathbf{r}} \left(c_{A,\mathbf{r}} + i c_{B,\mathbf{r}}\right) \qquad & c_{A,\mathbf{r}} &= \frac{1}{\sqrt{N}} \sum_{\mathbf{q}} e^{-i\mathbf{q}.\mathbf{r}} a'_{\mathbf{q}} + e^{i\mathbf{q}.\mathbf{r}} a'^\dagger_{\mathbf{q}} \\ a'^\dagger_{\mathbf{q}} &= \frac{1}{2\sqrt{N}} \sum_{\mathbf{r}} e^{-i\mathbf{q}.\mathbf{r}} \left(c_{A,\mathbf{r}} - i c_{B,\mathbf{r}}\right) \qquad & c_{B,\mathbf{r}} &= \frac{-i}{\sqrt{N}} \sum_{\mathbf{q}} e^{-i\mathbf{q}.\mathbf{r}} a'_{\mathbf{q}} - e^{i\mathbf{q}.\mathbf{r}} a'^\dagger_{\mathbf{q}} \end{aligned} \tag{2.19}$$

$$H_u = \sum_{\mathbf{q}} \begin{pmatrix} a'^\dagger_{\mathbf{q}} & a'_{-\mathbf{q}} \end{pmatrix} \begin{pmatrix} S_R(\mathbf{q}) & iS_I(\mathbf{q}) \\ -iS_I(\mathbf{q}) & -S_R(\mathbf{q}) \end{pmatrix} \begin{pmatrix} a'_{\mathbf{q}} \\ a'^\dagger_{-\mathbf{q}} \end{pmatrix},$$

where $S_R(\mathbf{q})$ and $S_I(\mathbf{q})$ are the real and imaginary parts of $S(\mathbf{q}) = J_x e^{i\mathbf{q}.\mathbf{n}_1} + J_y e^{i\mathbf{q}.\mathbf{n}_2} + J_z$ respectively. Later it will be useful to use a shorthand notation $q_1 = \mathbf{q}.\mathbf{n}_1$ and $q_2 = \mathbf{q}.\mathbf{n}_2$ so that $S(\mathbf{q}) = J_x e^{iq_1} + J_y e^{iq_2} + J_z$. Note the unusual normalisation required to convert between Majorana and complex fermions. This Hamiltonian can then be diagonalised by Bogoliubov transformation

$$\begin{pmatrix} a'_{\mathbf{q}} \\ a'^\dagger_{-\mathbf{q}} \end{pmatrix} = \begin{pmatrix} \cos(\theta_{\mathbf{q}}) & i\sin(\theta_{\mathbf{q}}) \\ i\sin(\theta_{\mathbf{q}}) & \cos(\theta_{\mathbf{q}}) \end{pmatrix} \begin{pmatrix} a_{\mathbf{q}} \\ a^\dagger_{-\mathbf{q}} \end{pmatrix} \qquad \text{where } \tan(2\theta_{\mathbf{q}}) = -\frac{S_I(\mathbf{q})}{S_R(\mathbf{q})} \tag{2.20}$$

$$H_u = \sum_{\mathbf{q}} |S(\mathbf{q})| (2a^\dagger_{\mathbf{q}} a_{\mathbf{q}} - 1)$$

The Hamiltonian $H_u$ with fixed bond fermion number has a Hilbert space dimension of $\sqrt{2}^{2N} = 2^N$ and having transformed back to complex fermions, we should check that the Hilbert space dimension is unchanged. There are $N$ unit cells and hence $N$ values of $\mathbf{q}$ and $N$ independent $a_{\mathbf{q}}^\dagger$ fermion operators, so the Hilbert space dimension is $2^N$, as before. There are two distinct types of excitation: Flux excitations of $|\chi\rangle$, which are gapped, and matter fermion excitations of $|a_{\mathbf{q}}^\dagger\rangle$ that have a spectrum $|S(\mathbf{q})|$ and which will be gapped if $|J_z| > |J_x| + |J_y|$ or permutations thereof. For $J_\alpha > 0$ there are three topologically distinct gapped phases, given the labels $A_x, A_y, A_z$ and one gapless phase $B$, as shown in Figure 2.5(a).

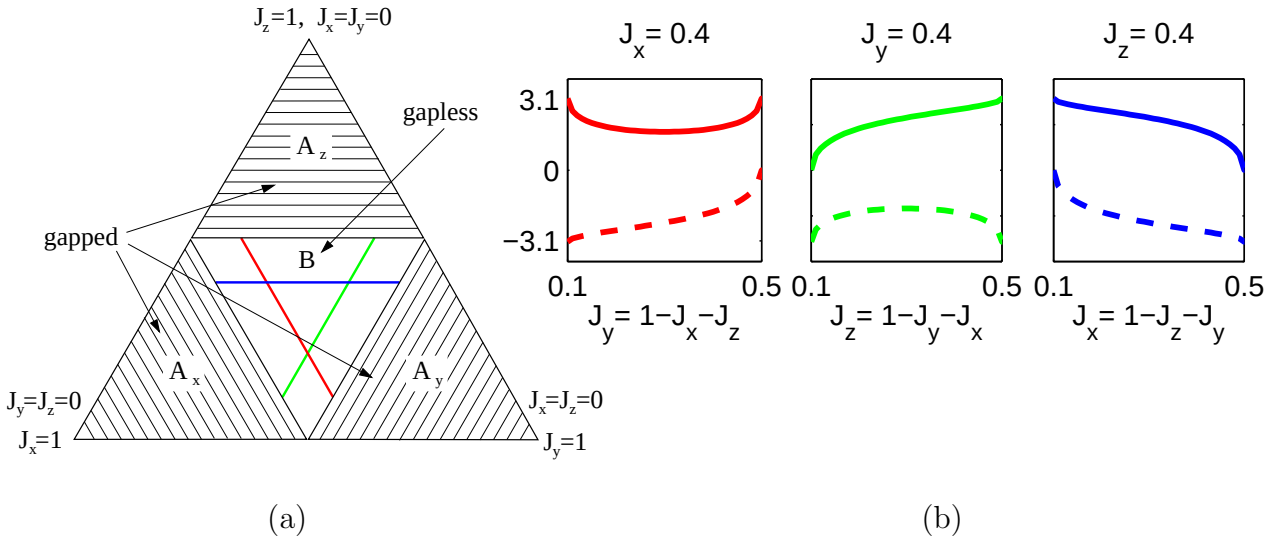



Figure 2.5: (a)Phase diagram for $J_\alpha > 0$. (b) $Q_1$ (solid line) and $Q_2$ (dashed line) for the directions in parameter space shown in (a). $\mathbf{Q}$ merges with $-\mathbf{Q}$ as the model reaches the edge of the gapless phase in parameter space.

In the gapless phase there are two zero energy modes in the first Brillouin zone. Defining the zero energy momentum $\mathbf{Q} = (Q_1, Q_2)$, they are found through the conditions $S_R(\mathbf{Q}) = S_I(\mathbf{Q}) = 0$. Define $j_x \equiv J_x/J_z$ and $j_y = J_y/J_z$. The zero energy momentum points are at

$$Q_1 \equiv \pm \cos^{-1}\left[\frac{j_x^2 - j_y^2 - 1}{2j_y}\right] \qquad Q_2 = \mp \cos^{-1}\left[\frac{-j_x^2 + j_y^2 - 1}{2j_x}\right] \tag{2.21}$$

$Q_1$ and $Q_2$ are real if and only if the Hamiltonian is in the parameter space for the gapless phase. The spectrum is asymptotically linear around these points and they are hence termed Dirac points. For $J_\alpha = 1$, $\mathbf{Q} = (2\pi/3, -2\pi/3)$ and linearity can be demonstrated easily: define a small momentum $\mathbf{p}$ such that $\mathbf{q} = \mathbf{Q} + \mathbf{p}$, then $|S(\mathbf{p})| \simeq [\frac{3}{4}(p_x^2 + p_y^2)]^{1/2}$. Similar results are obtained throughout the gapless phase.

Moving towards the boundary of the gapless phase in parameter space, the two Dirac points at $\pm\mathbf{Q}$ move towards each other in the Brillouin zone before fusing at the boundary and disappearing. There are three inequivalent and non zero points in the first Brillouin zone where $\mathbf{Q} = -\mathbf{Q}$ and they can fuse: $\mathbf{Q} = (0, \pm\pi), (\pm\pi, \mp\pi), (\pm\pi, 0)$. The Dirac points fuse in this manner for the paths in parameter space indicated in Figure 2.5(a), with $Q_1$ and $Q_2$ plotted in Figure 2.5(b).

The similarity with graphene is now clear. The spectrum of matter fermion excitations in the Kitaev model may be deduced from the eigenvalues of the tight binding model for hopping on a hexagonal lattice, i.e. the tight binding model for graphene. We issue a caution though: the Kitaev model is a spin Hamiltonian and the transformations required

to obtain the spectrum from a tight binding model are non-trivial. In particular, this means that the similarity to graphene is completely lost when we consider the Kitaev model in a magnetic field.

Although spin correlations are strictly nearest neighbour we would expect some algebraic range correlations in the gapless phase. The local energy can be defined for nearest neighbour sites $j$ and $k$, with $j$ on the A sublattice in unit cell at $\mathbf{r}$, as $E^{\alpha}(\mathbf{r}) = \sigma_j^{\alpha_{jk}}\sigma_k^{\alpha_{jk}}$ and we shall see that these observables have just such long range correlations. To find the energy correlations the following results are needed: Writing $b_j^{\alpha_{jk}} = (\chi_j^{\alpha_{jk}})^\dagger + \chi_j^{\alpha_{jk}}$ and $b_k^{\alpha_{jk}} = i(\chi_j^{\alpha_{jk}})^\dagger - \chi_j^{\alpha_{jk}}$ it is clear that $\langle b_j^{\alpha} b_k^{\beta}\rangle = 0$ unless $j,k$ are nearest neighbours and $\alpha = \beta = \alpha_{jk}$; In the ground state flux sector a gauge can be chosen such that all $u_{jk} = +1$ and $\langle b_j^{\alpha_{jk}} b_k^{\alpha_{jk}}\rangle = -i\langle \hat{u}_{jk}\rangle = -i$; Wick's theorem can be used with Majorana fermions in just the way it can be for complex fermions.

The energy correlators in the $z$ direction are given by

$$\begin{aligned}
&\langle E^z(\mathbf{r})E^z(\mathbf{r}')\rangle - \langle E^z(\mathbf{r})\rangle\langle E^z(\mathbf{r}')\rangle \\
=\ &\langle ib^z_{A,\mathbf{r}}c_{A,\mathbf{r}}ib^z_{B,\mathbf{r}}c_{B,\mathbf{r}}ib^z_{A,\mathbf{r}'}c_{A,\mathbf{r}'}ib^z_{B,\mathbf{r}'}c_{B,\mathbf{r}'}\rangle - \langle ib^z_{A,\mathbf{r}}c_{A,\mathbf{r}}ib^z_{B,\mathbf{r}}c_{B,\mathbf{r}}\rangle\langle ib^z_{A,\mathbf{r}'}c_{A,\mathbf{r}'}ib^z_{B,\mathbf{r}'}c_{B,\mathbf{r}'}\rangle \\
=\ &[\langle c_{A,\mathbf{r}}c_{B,\mathbf{r}}c_{A,\mathbf{r}'}c_{B,\mathbf{r}'}\rangle - \langle c_{A,\mathbf{r}}c_{B,\mathbf{r}}\rangle\langle c_{A,\mathbf{r}'}c_{B,\mathbf{r}'}\rangle] \times \left[\langle b^z_{A,\mathbf{r}}b^z_{B,\mathbf{r}}\rangle\langle b^z_{A,\mathbf{r}'}b^z_{B,\mathbf{r}'}\rangle\right] \\
=\ &[\langle c_{A,\mathbf{r}}c_{B,\mathbf{r}'}\rangle\langle c_{B,\mathbf{r}}c_{A,\mathbf{r}'}\rangle - \langle c_{A,\mathbf{r}}c_{A,\mathbf{r}'}\rangle\langle c_{B,\mathbf{r}}c_{B,\mathbf{r}'}\rangle] \times (-1)
\end{aligned} \tag{2.22}$$

The Majorana correlators given above can be found explicitly for this translationally invariant system. In the ground state

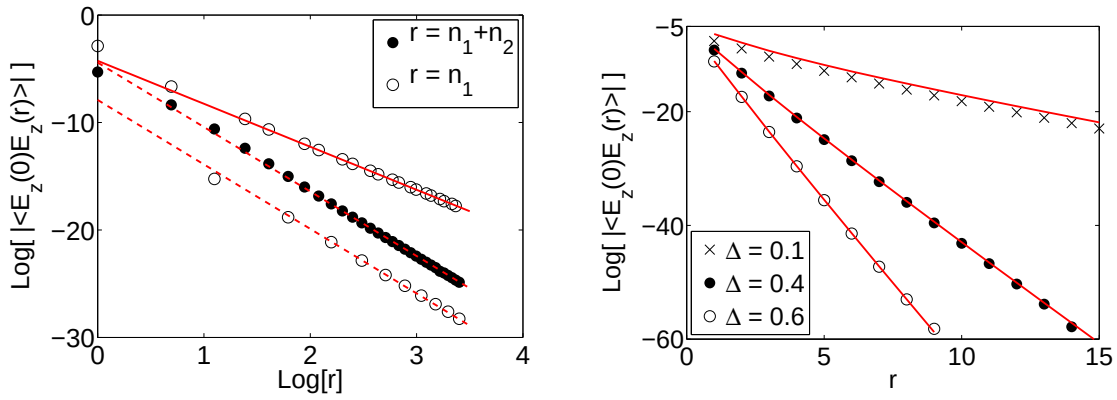
$$\begin{aligned}
\langle c_{A,\mathbf{r}}c_{B,\mathbf{r}'}\rangle =\ & \frac{-i}{N}\sum_{\mathbf{q},\mathbf{q}'}\langle\left(e^{-i\mathbf{q}.\mathbf{r}}a'_{\mathbf{q}} + e^{i\mathbf{q}.\mathbf{r}}a'^{\dagger}_{\mathbf{q}}\right)\left(e^{-i\mathbf{q}.\mathbf{r}'}a'_{\mathbf{q}} - e^{i\mathbf{q}.\mathbf{r}'}a'^{\dagger}_{\mathbf{q}}\right)\rangle \\
=\ & \frac{-i}{N}\sum_{\mathbf{q}} e^{-i\mathbf{q}.(\mathbf{r}-\mathbf{r}')}(\sin^2(\theta_{\mathbf{q}}) - \cos^2(\theta_{\mathbf{q}}) = \frac{i}{N}\sum_{\mathbf{q}}\frac{S_R(\mathbf{q})e^{-i\mathbf{q}.(\mathbf{r}-\mathbf{r}')}}{|S(\mathbf{q})|} \\
\langle c_{A,\mathbf{r}}c_{A,\mathbf{r}'}\rangle =\ & \langle c_{B,\mathbf{r}}c_{B,\mathbf{r}'}\rangle = \delta_{\mathbf{r}=\mathbf{r}'}
\end{aligned} \tag{2.23}$$

Using the above matrix elements, the energy correlators can be shown to be

$$\langle E^z(\mathbf{r})E^z(\mathbf{r}')\rangle - \langle E^z(\mathbf{r})\rangle\langle E^z(\mathbf{r}')\rangle = -\left|\frac{1}{N}\sum_{\mathbf{q}}\frac{S_R(\mathbf{q})e^{-i\mathbf{q}.(\mathbf{r}-\mathbf{r}')}}{|S(\mathbf{q})|}\right|^2 + \delta_{\mathbf{r}=\mathbf{r}'} \tag{2.24}$$

This expression is evaluated numerically in both the gapped and gapless phases, with the results shown in Figure 2.6. As expected it decays algebraically in the gapless phase and exponentially in the gapped.

To evaluate this correlator analytically we take the thermodynamic limit by letting the system size go to infinity and turn the summation into an integral. In the gapless phase,




(a) (b)

Figure 2.6: a) Energy correlations in the gapless phase along $\mathbf{r} = r(\mathbf{n}_1 + \mathbf{n}_2)$ and $\mathbf{r} = r\mathbf{n}_1$. Red lines are guides for the eye with gradient -4 solid and -6 dashed. b) Energy correlations in the gapped phase, where they decay exponentially. Here we plot along a line $\mathbf{r} = r(\mathbf{n}_1 + \mathbf{n}_2)$, for $\Delta = 0.1, 0.4, 0.6$ and with $J_z + J_x + J_y = 1$. Red curves are the analytic calculation.

the dominant contribution to the integral will come from the non analytic points of the integrand at $\pm\mathbf{Q}$. One can then expand around these points $\mathbf{q} = \pm\mathbf{Q} + \mathbf{p}$ and use a smooth cut off on $\mathbf{p}$, such as $\exp[-(arp)^2]$, where $p = |\mathbf{p}|$, $r = |\mathbf{r}|$ and $a \ll 1$. This cuts off the integral at $|\mathbf{p}| \sim 1/a|\mathbf{r}|$. A smooth cut off must be used as a hard cut off would introduce long range correlations that decayed more slowly than those of the true energy correlators. Setting $\mathbf{r}' = 0$, $J_\alpha = 1$ and by defining $\theta_\mathbf{r}$ as the angle between $\mathbf{r}$ and the x-axis, the integral becomes

$$\begin{aligned}
\int \frac{S_R(\mathbf{q})e^{-i\mathbf{q}.\mathbf{r}}}{|S(\mathbf{q})|}\frac{d^2q}{4\pi^2} &\simeq \int \left(\frac{-p_x\cos(-\mathbf{Q}.\mathbf{r} - \mathbf{p}.\mathbf{r})}{|\mathbf{p}|} + \frac{p_x\cos(\mathbf{Q}.\mathbf{r} - \mathbf{p}.\mathbf{r})}{|\mathbf{p}|}\right) e^{-(arp)^2}\frac{d^2\mathbf{p}}{4\pi^2} \\
&= \int_{\theta=-\pi}^{\pi}\int_{p=0}^{\infty} 2\cos(\theta)\sin(pr\cos(\theta - \theta_\mathbf{r}))\sin(\mathbf{Q}.\mathbf{r})e^{-(arp)^2}\frac{pdpd\theta}{4\pi^2} \\
&= \int_{p=0}^{\infty}\cos(\theta_\mathbf{r})\sin(\mathbf{Q}.\mathbf{r})pJ_1(pr)e^{-ap^2}\frac{dp}{\pi} \\
&= \frac{1}{r^2}\cos(\theta_\mathbf{r})\sin(\mathbf{Q}.\mathbf{r})\int_{x=0}^{\infty} xJ_1(x)e^{-ax^2}\frac{dx}{\pi}
\end{aligned} \tag{2.25}$$

To leading order, the energy correlators therefore decay as $\sim 1/r^4$. If the separation is perpendicular to the x-axis, so that $\theta_\mathbf{r} = \pi/2$, then the leading order term vanishes and the decay will be at a higher power of $1/r$. A similar effect will occur if $\sin(\mathbf{Q}.\mathbf{r}) = 0$. Both of these effects are seen in Figure 2.6(a), where we have numerically integrated Eq. (2.24) along lines $\mathbf{r} = r(\mathbf{n}_1 + \mathbf{n}_2)$ and $\mathbf{r} = r\mathbf{n}_1$.

In the gapped phase, where $j_x < 1$ and $j_y < 1$ the summation can be evaluated in a different manner: by performing an expansion of $S(\mathbf{q})$ in $j_x$ and $j_y$, which converges inside the gapped phase. Only certain terms from this expansion will then contribute to the integral.

$$\int \frac{S_R(\mathbf{q})e^{-i\mathbf{q}.\mathbf{r}}}{|S(\mathbf{q})|}\frac{d^2\mathbf{q}}{4\pi^2} = \int \frac{S(\mathbf{q})\cos(\mathbf{q}.\mathbf{r})}{|S(\mathbf{q})|}\frac{d^2\mathbf{q}}{4\pi^2} = \int \sqrt{\frac{S(\mathbf{q})}{S^*(\mathbf{q})}}\cos(\mathbf{q}.\mathbf{r})\frac{d^2\mathbf{q}}{4\pi^2}$$

$$= \int \sum_{n,n'=0}^{\infty} \frac{(-1)^n(2n)!}{(1-2n)(n!)^2 4^n}\left(j_x e^{iq_1} + j_y e^{iq_2}\right)^n \times$$

$$\frac{(-1)^{n'}(2n'+2)!}{2(1+2n')n'!(n'+1)!4^{n'}}\left(j_x e^{-iq_1} + j_y e^{-iq_2}\right)^{n'}\cos(\mathbf{q}.\mathbf{r})\frac{d^2\mathbf{q}}{4\pi^2} \tag{2.26}$$

Most terms in this summation are annihilated by the integral over $\mathbf{q}$, although there are still an infinite number of non zero terms. However, if the gap is large then the above summation may be approximated by considering only the lowest order term that is not annihilated by the integral over $\mathbf{q}$. The correlators are inversion symmetric in $\mathbf{r}$ and we therefore only consider the two cases for positive $n_1, n_2$: $\mathbf{r} = n_1\mathbf{n}_1 + n_2\mathbf{n}_2$ and $\mathbf{r} = n_1\mathbf{n}_1 - n_2\mathbf{n}_2$. To lowest order in $j_x, j_y$, the integral is

$$\frac{(-1)^{n_1+n_2}(2n_1+2n_2)!}{2[(n_1+n_2)!]^2 4^{n_1+n_2}}\begin{pmatrix} n_1+n_2 \\ n_1 \end{pmatrix} j_x^{n_1} j_y^{n_2}\left[1 + \frac{1}{1-2n_1-2n_2}\right] \qquad \mathbf{r} = n_1\mathbf{n}_1 + n_2\mathbf{n}_2 \tag{2.27}$$

$$\frac{(-1)^{n_1+n_2}(2n_1)!(2n_2)!}{2(n_1!)^2(n_2!)^2 4^{n_1+n_2}} j_x^{n_1} j_y^{n_2}\left[\frac{1}{1-2n_1} + \frac{1}{1-2n_2}\right] \qquad \mathbf{r} = n_1\mathbf{n}_1 - n_2\mathbf{n}_2 \tag{2.28}$$

Both of these decay exponentially. In Figure 2.6(b) we plot the energy correlations along $\mathbf{r} = r(\mathbf{n}_1 + \mathbf{n}_2)$ for gaps $\Delta = 0.1, 0.4, 0.6$ and with $J_z + J_x + J_y = 1$. The decay is still exponential for a small gap and large $r$ but the above approximation becomes less good as other terms in the summation become significant. After we completed this calculation, similar work was published by other authors[91].

## 2.4 Proposals for experiment

At first glance the Kitaev model does not look very realistic. How would one create the strong correlations between real space and spin degrees of freedom necessary to produce the

anisotropic interactions in the Hamiltonian? However, strong spin orbit coupling of late transition metal (TM) ions (e.g. Ir, Os, Rh and Ru) can produce just such an anisotropy [49, 19]. More precisely, the spin-orbit coupling of a single hole in an otherwise full $t_{2g}$ level far exceeds the interactions between $t_{2g}$-levels on different sites. Therefore, the spin and orbital angular momentum are 'locked' together forming a total angular momentum locally. The $t_{2g}$ level is three fold degenerate and consists of $xy$, $xz$ and $yz$ orbitals, which are themselves anisotropic in space. Each orbital preferentially interacts along particular spatial orientations, thereby generating an anisotropic spin interaction. For certain TM ions, the anisotropic interaction is found to reproduce the Kitaev Hamiltonian. A hexagonal lattice may be generated by, for instance, taking a slice in the [111] plane and by the periodic replacement of magnetic ions by non-magnetic ions, as shown in Figure 2.7.

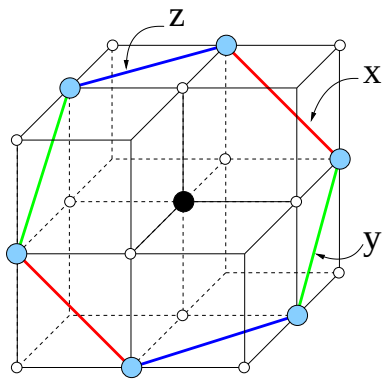



Figure 2.7: Figure from Ref. [49]. TM ions in light blue have super exchange via oxygen atoms drawn in white. Substitution of a subset of TM ions by non magnetic ions (black dot) leads to hexagonal lattice in [111] plane.

There have also been proposals for experimental realisations using cold atoms in optical lattices. At the root of these experiments is the ability to use lasers to generate a spatially variable, spin dependent potential on either individual atoms[25] or polar molecules[64]. Interfering lasers generate a standing wave potential that forms the lattice. The particles are energetically constrained to lie on the sites of this lattice, forming a Mott insulator. There is only virtual hopping between sites, which leads to a spin Hamiltonian with exchange coupling dependent on the standing wave potential generated by the lasers. Additional beams are then used to introduce the spin dependent fields by using linearly polarised light. Careful control of the interference patterns produced by these lasers allows the experimentalist to control the height of the various spin dependent potential barriers between lattice sites and the point symmetries of the lattice itself. In this way it is possible to produce a large number of tunable spin Hamiltonians such as Ising, Heisenberg, XXZ and the

Kitaev Hamiltonian[25, 64]. Furthermore, since the parameters are adjustable, one can tune freely between gapped and gapless phases.

## 2.5 Thesis outline

The Kitaev model is so attractive because it is exactly solvable, yet non-trivial. We have seen that it has a spin liquid ground state but with algebraic bond energy correlations. Furthermore, the spins are fractionalised into two types of excitation - matter fermion and flux excitations. The rest of this thesis addresses the issue of disorder in this model. Crucially, we find that the model remains exactly solvable in the presence of certain types of disorder. The properties of the model with disorder can then be used as a test of this intricate description in terms of matter and flux excitations.

In chapters 3 and 4 we focus mainly on the magnetic response of the system with varying amounts of site dilution. We consider a single vacancy, two vacancies and a finite density of vacancies in the gapped and gapless phases. The response is found to be markedly different for the two phases and we separate our analysis accordingly. Furthermore, a finite density of vacancies changes the density of states at low energies and we study the resultant effects on the heat capacity.

Having investigated the effects of site dilution, in chapter 5 we then turn to several other types of disorder including weak and strong, slowly varying disorder in exchange parameters and also disorder in the signs of the exchange. Finally, in chapter 6 we summarise the main results of this thesis, present some questions that are left unresolved by the current work and also some areas that might prove interesting places for further study.

Some of the results of this thesis may be found in a Letter [89] and a longer work to be published soon [88].

# Chapter 3

# Site dilution in the gapped Phase

In many respects properties of the gapped phase are easier to discern than the gapless phase. In general, integrals converge and computer simulations do no suffer from the finite size effects that plague calculations in the gapless phase. Also, if the gap is large then many calculations can be approximated by an expansion using $j_x, j_y$ as small parameters, as was seen already in the calculation of the energy correlations. Despite this, the gapped phase is far from trivial and we will see that disorder has an effect on both the flux and matter sectors. We take $0 < J_\alpha$ and $j_x + j_y < 1$ throughout.

## 3.1 Flux binding

The ground state flux sector of the clean Kitaev model is flux free, for example with $u_{jk} = +1$ on every link. However, we will show that the removal of a site binds a flux to the vacancy plaquette. In the limit, $j_x \ll 1, j_y \ll 1$ the energy cost of changing the flux sector may be found by perturbation theory, without resorting to the Majorana decomposition given above[52]. Therefore, in this section, operators will appear with a tilde since calculations are performed in spin space. We do not follow the approach presented by Kitaev. Instead we use degenerate perturbation theory[15, 63] and extend it to a system with vacancies to show that the ground state has a flux bound to each vacancy. The Hamiltonian is $\widetilde{H} = \widetilde{H}_0 + \widetilde{V}$, where $\widetilde{H}_0$ is the limit of decoupled pairs of spins on $z$ bonds and $\widetilde{V}$ is the perturbative exchange coupling along $x$ and $y$ bonds.

$$\begin{aligned} \widetilde{H}_0 &= -J_z \sum_{\text{z-links}} \tilde{\sigma}^z_j \tilde{\sigma}^z_k \\ \widetilde{V} &= -J_x \sum_{\text{x-links}} \tilde{\sigma}^x_j \tilde{\sigma}^x_k - J_y \sum_{\text{y-links}} \tilde{\sigma}^y_j \tilde{\sigma}^y_k \end{aligned} \tag{3.1}$$

The ground state of $\widetilde{H}_0$ is $2^N$-fold degenerate and has an energy $E_0 = -J_z N$. Since each pair of spins in a unit cell must be aligned in the ground state, one can combine them into one effective spin $|\uparrow\uparrow\rangle = |\Uparrow\rangle$ and $|\downarrow\downarrow\rangle = |\Downarrow\rangle$. In the end we would like to find an effective perturbation that acts within this space of effective spins. To find the low energy states, one can project onto ground states of $\widetilde{H}_0$ and work perturbatively in $\widetilde{V}$. In this restricted subspace $\widetilde{V}$ takes the form of an effective flux Hamiltonian that acts within the ground states of $\widetilde{H}_0$, lifting the degeneracy.

Let $\Pi$ be a projection onto ground states of $\widetilde{H}_0$ and define operators

$$\begin{gathered} Q = 1 - \Pi \ , \qquad \frac{Q}{a^k} \equiv Q \frac{1}{(E_0 - \widetilde{H}_0)^k} Q \ , \qquad S^k = \begin{cases} -\Pi & \text{if } k = 0 \\ \dfrac{Q}{a^k} & \text{if } k \geq 1 \end{cases} \\ \widetilde{U} = \sum_{n=0}^{\infty} \widetilde{U}^{(n)} \ , \qquad \widetilde{U}^{(n)} = \sum_{(n)} S^{k_1} \widetilde{V} S^{k_2} \widetilde{V} \cdots \widetilde{V} S^{k_n} \widetilde{V} \Pi \ . \end{gathered} \tag{3.2}$$

The summation $\sum_{(n)}$ is over all sets of non-negative integers $k_1, k_2, \ldots, k_n$ satisfying the conditions

$$\begin{aligned} &k_1 + k_2 + \cdots + k_p \geq p \quad (p = 1, 2, \ldots, n-1) \\ &k_1 + k_2 + \cdots + k_n = n \ . \end{aligned} \tag{3.3}$$

The eigenvalues of the perturbed Hamiltonian in the ground state subspace are given by the eigenvalues of the operator $\widetilde{H}_{\text{eff}} = \Pi \widetilde{H} \widetilde{U}$ [15, 63]. The expansion of $\widetilde{U}$ in turn generates an expansion for $\widetilde{H}_{\text{eff}} = \sum_j \widetilde{H}^{(j)}_{\text{eff}}$.

The action of $\widetilde{V}$ on a state is to flip two spins and thus change the energy by $4J_z$. Let the eigenvectors of $\widetilde{H}_0$ be $|n\rangle$, such that $\widetilde{H}_0 |n\rangle = E_n |n\rangle$. The first five and n$^{\text{th}}$ terms in the perturbation theory are

$$\begin{aligned} \widetilde{H}^{(0)}_{\text{eff}} &= E_0 \Pi \\ \widetilde{H}^{(1)}_{\text{eff}} &= \Pi \widetilde{V} \Pi = 0 \\ \widetilde{H}^{(2)}_{\text{eff}} &= \Pi \widetilde{V} \frac{Q}{a} \widetilde{V} \Pi = \Pi \sum_n{}' \frac{\widetilde{V}|n\rangle\langle n|\widetilde{V}}{E_0 - E_n} \Pi = -\sum_{\text{x-links}} \frac{J_x^2}{4J_z} - \sum_{\text{y-links}} \frac{J_y^2}{4J_z} = -\frac{NJ_z}{4} \left(j_x^2 + j_y^2\right) \\ \widetilde{H}^{(3)}_{\text{eff}} &= \Pi \left( -\widetilde{V} \frac{Q}{a^2} \widetilde{V} \Pi \widetilde{V} + \widetilde{V} \frac{Q}{a} \widetilde{V} \frac{Q}{a} \widetilde{V} \right) \Pi = 0 \\ \widetilde{H}^{(4)}_{\text{eff}} &= \Pi \left( -\widetilde{V} \frac{Q}{a^2} \widetilde{V} \Pi \widetilde{V} \frac{Q}{a} \widetilde{V} + \widetilde{V} \frac{Q}{a} \widetilde{V} \frac{Q}{a} \widetilde{V} \frac{Q}{a} \widetilde{V} \right) \Pi \\ \widetilde{H}^{(n+1)}_{\text{eff}} &= \Pi \widetilde{V} \widetilde{U}^{(n)} \ , \end{aligned} \tag{3.4}$$

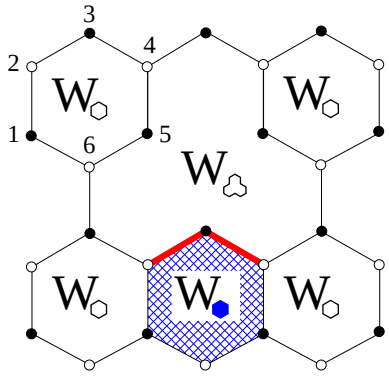



Figure 3.1: In the establishment of an effective flux Hamiltonian for a system with isolated vacancies we define three types of plaquettes with fluxes as shown.

where the primed summation is restricted to states not in the ground state manifold of $\widetilde{H}_0$. $\widetilde{H}^{(2)}_{\text{eff}}$ simply provides a constant shift to the zeroth oder energy $E_0$. Notice that $\widetilde{H}^{(1)}_{\text{eff}}$ and $\widetilde{H}^{(3)}_{\text{eff}}$ are both zero. In fact, since there must be an even number of spin flips to return to the ground state of $\widetilde{H}_0$, all odd terms of $\widetilde{H}^{(n)}_{\text{eff}}$ will be zero. At higher order, each $H^{(n)}_{\text{eff}}$ will contain parts that are a small perturbation on terms already found at lower order.

For a clean lattice, the lowest order term that reduces the ground state degeneracy is

$$\widetilde{H}^{(4)}_{\text{eff}} = -\frac{J_z}{16} j_x^2 j_y^2 \sum \widetilde{W}_{\hexagon} + \text{const } \mathrm{O}(j_x^2 + j_y^2)^2 \tag{3.5}$$

where $\widetilde{W}_{\hexagon}$ is the flux through a hexagonal plaquette of the lattice. The factor $-\frac{1}{16}$ is found from summing 4! terms, corresponding to the permutations of acting with elements from the four $\widetilde{V}$ operators. These come with an energetic contributions and sign dependent on the permutation. For example, using the site labelling shown in Figure 3.1, consider the following three terms that contribute to $\widetilde{H}^{(4)}_{\text{eff}}$

$$\begin{aligned}
&1) \quad J_x\tilde{\sigma}_2^x\tilde{\sigma}_3^x\frac{-1}{4J_z}J_y\tilde{\sigma}_3^y\tilde{\sigma}_4^y\frac{-1}{4J_z}J_x\tilde{\sigma}_5^x\tilde{\sigma}_6^x\frac{-1}{4J_z}J_y\tilde{\sigma}_6^y\tilde{\sigma}_1^y = +\frac{J_x^2J_y^2}{64J_z^3}\tilde{\sigma}_2^y\tilde{\sigma}_2^z\tilde{\sigma}_3^z\tilde{\sigma}_4^z\tilde{\sigma}_4^x\tilde{\sigma}_5^y\tilde{\sigma}_5^z\tilde{\sigma}_6^z\tilde{\sigma}_1^z\tilde{\sigma}_1^x \\
&\quad = +\frac{J_z}{64}j_x^2j_y^2\widetilde{W}_{\hexagon}\tilde{\sigma}_1^z\tilde{\sigma}_2^z\tilde{\sigma}_4^z\tilde{\sigma}_5^z = +\frac{J_z}{64}j_x^2j_y^2\widetilde{W}_{\hexagon} \\
&2) \quad J_y\tilde{\sigma}_3^y\tilde{\sigma}_4^y\frac{-1}{4J_z}J_x\tilde{\sigma}_2^x\tilde{\sigma}_3^x\frac{-1}{4J_z}J_x\tilde{\sigma}_5^x\tilde{\sigma}_6^x\frac{-1}{4J_z}J_y\tilde{\sigma}_6^y\tilde{\sigma}_1^y = -\frac{J_x^2J_y^2}{64J_z^3}\tilde{\sigma}_4^z\tilde{\sigma}_4^x\tilde{\sigma}_3^z\tilde{\sigma}_2^y\tilde{\sigma}_2^z\tilde{\sigma}_5^y\tilde{\sigma}_5^z\tilde{\sigma}_6^z\tilde{\sigma}_1^z\tilde{\sigma}_1^x \\
&\quad = -\frac{J_z}{64}j_x^2j_y^2\widetilde{W}_{\hexagon}\tilde{\sigma}_1^z\tilde{\sigma}_2^z\tilde{\sigma}_4^z\tilde{\sigma}_5^z = -\frac{J_z}{64}j_x^2j_y^2\widetilde{W}_{\hexagon} \\
&3) \quad J_x\tilde{\sigma}_2^x\tilde{\sigma}_3^x\frac{-1}{4J_z}J_x\tilde{\sigma}_6^x\tilde{\sigma}_5^x\frac{-1}{8J_z}J_x\tilde{\sigma}_3^y\tilde{\sigma}_4^y\frac{-1}{4J_z}J_y\tilde{\sigma}_6^y\tilde{\sigma}_1^y = +\frac{J_x^2J_y^2}{128J_z^3}\tilde{\sigma}_2^y\tilde{\sigma}_2^z\tilde{\sigma}_3^z\tilde{\sigma}_5^y\tilde{\sigma}_5^z\tilde{\sigma}_4^z\tilde{\sigma}_4^x\tilde{\sigma}_6^z\tilde{\sigma}_1^z\tilde{\sigma}_1^x \\
&\quad = +\frac{J_z}{128}j_x^2j_y^2\widetilde{W}_{\hexagon}\tilde{\sigma}_1^z\tilde{\sigma}_2^z\tilde{\sigma}_4^z\tilde{\sigma}_5^z = +\frac{J_z}{128}j_x^2j_y^2\widetilde{W}_{\hexagon}
\end{aligned} \tag{3.6}$$

Separating such terms by their energetic contribution to the effective perturbation we find

$$\left(4\cdot\frac{1}{64}+12\cdot\frac{-1}{64}+8\cdot\frac{1}{128}\right)J_z j_x^2 j_y^2\sum\widetilde{W}_{\hexagon}=-\frac{1}{16}J_z j_x^2 j_y^2\sum\widetilde{W}_{\hexagon}\ . \tag{3.7}$$

If the lattice has one or more vacancies, then at each vacancy there is one hexagonal plaquette that has a larger prefactor, indicated by ⬢ in Figure 3.1. Here, the two elements of $\widetilde{V}$ adjacent with the vacancy plaquette still flip a spin pair but since the bond to the vacancy site has been removed, the energy change is only $2J_z$ . These elements are shown in red in Figure 3.1, where we also define the vacancy plaquette ⏢. The contribution from plaquettes ⬢ to the effective Hamiltonian again comes from 4! terms that can be summed to give a term

$$\left(2\cdot\frac{-1}{8}+4\cdot\frac{-1}{16}+2\cdot\frac{1}{24}+2\cdot\frac{-1}{32}+4\cdot\frac{1}{48}+2\cdot\frac{1}{96}\right)J_z j_x^2 j_y^2\sum\widetilde{W}_{\hexagon}=-\frac{3}{8}J_z j_x^2 j_y^2\sum\widetilde{W}_{\hexagon}. \tag{3.8}$$

There will of course be terms of $6^{\text{th}}$ order and higher for the hexagonal plaquettes but these are subordinate to those already mentioned and are not significant if the gap is large.

The perturbation theory must be extended to $8^{\text{th}}$ order to find a term that is dependent on the flux through the vacancy plaquettes. This involves a summation of 8! permutations from terms encircling ⏢ and an additional 8! from those encircling both ⏢ and ⬢ plaquettes, which are both $8^{\text{th}}$ order in the perturbation. This leads to a term

$$J_z j_x^4 j_y^4\left(\frac{21}{2^{10}}\sum\widetilde{W}_{⏢}-\frac{33}{2^{11}}\sum\left(\widetilde{W}_{⏢}\times\widetilde{W}_{\hexagon}\right)\right) \tag{3.9}$$

Since this involved a summation over a large number of terms it is sensible to check with results from exact diagonalisation of the tight binding Hamiltonian (2.18). Figure 3.2 shows that the two are in good agreement as the gap becomes large.

Combining all these terms, to lowest order in flux operators the effective Hamiltonian for a system containing isolated vacancies is

$$\begin{aligned}\widetilde{H}_{\text{eff}}=\ & E_0-J_z j_x^2 j_y^2\left(\frac{1}{16}\sum\widetilde{W}_{\hexagon}+\frac{3}{8}\sum\widetilde{W}_{\hexagon}\right)\\ & +J_z j_x^4 j_y^4\left(\frac{21}{2^{10}}\sum\widetilde{W}_{⏢}-\frac{33}{2^{11}}\sum\left(\widetilde{W}_{⏢}\times\widetilde{W}_{\hexagon}\right)\right)\cdots\ .\end{aligned} \tag{3.10}$$

The ellipsis here represent higher order terms associated with each $\widetilde{H}_{\text{eff}}^{(n)}$. For example, $E_0$ has an $O(NJ_z j_x^2 j_y^2)$ correction, where as each $\widetilde{W}_{\hexagon}$ has an $O(J_z j_x^4 j_y^4)$ correction. The fluxes $\widetilde{W}_{\hexagon}$ and $\widetilde{W}_{\hexagon}$ are determined by the fourth order terms in Eq. (3.10) and both are flux free in the ground state flux sector: $\langle\widetilde{W}_{\hexagon}\rangle=\langle\widetilde{W}_{\hexagon}\rangle=+1$. The terms involving $\widetilde{W}_{⏢}$ can then be combined to give a term $9/2^{11}\,J_z j_x^4 j_y^4\sum\widetilde{W}_{⏢}$. The positive sign on $\sum W_{⏢}$ indicates that

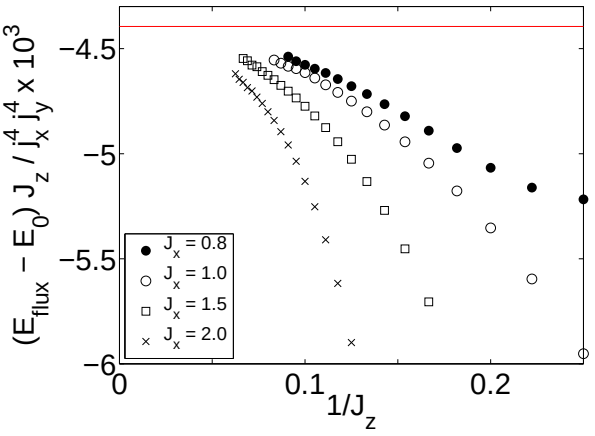



Figure 3.2: We find the difference in ground state energy of a system with and without fluxes attached to vacancies and use this to determine the flux binding energy. Specifically, we use a system of size $14 \times 14$ unit cells on twisted periodic boundary conditions with two well separated vacancies. We normalise the difference by $J_z^7/J_x^4 J_y^4 \times 10^3$ and do this for the various values of $J_z$ and $J_x$ indicated, whilst keeping $J_y = 1$. The red line is the analytic result $-9/2^{11} \times 10^3$.

the introduction of vacancies changes the ground state flux sector. With open boundary conditions, each vacancy binds a flux, $\widetilde{W}_{\hexagon} = -1$. This is irrespective of the vacancy sublattice. With periodic boundary conditions fluxes must appear in pairs. Therefore, with periodic boundary conditions it is energetically unfavourable for a single vacancy to bind a flux since the second flux must lie on a hexagonal plaquette. Indeed, a system with an odd number of vacancies will always have one that does not bind a flux. The interactions between fluxes will determine which vacancy plaquette is most energetically favourable to be flux free.

That impurities bind a flux has important consequences for topological quantum computations. One of the major sources of error in performing a calculation arises from stray quasiparticles that can braid with the intended and controlled quaisparticles of the qubit. At finite temperature there is a finite rate at which quasiparticle-quasihole pairs are created from the vacuum. If these have a long enough lifetime to braid with the topological quasi-particles that are used to perform a calculation, they will affect the result in an unquantifiable way. These thermally activated processes can be reduced by performing the calculation at temperatures much less than the gap for pair creation and in fact many will not affect the outcome even if they do occur[69]. However, there is another source of error due to impurities. It can be shown that the effective Hamiltonian (3.10) maps onto the more familiar toric code and that the elementary flux excitations are abelian anyons[51, 52].

Non-magnetic impurities may cause vacancies in the Kitaev model and the effective flux Hamiltonian (3.10) shows that in the ground state the vacancies have bound fluxes. Care must then be taken to keep track of the impurities in a sample being used for a computation.

## 3.2 Local moment formation

Having seen that a vacancy affects the flux sector, we now investigate its effects on the spectrum of matter states and describe the magnetic properties of the Kitaev model with a vacancy. We do this by calculating the changes to the spectrum of the tight binding model (2.18) caused by the inclusion of a vacancy, from which the ground state energy and spectrum of the Kitaev model may be read off. We will show that a single vacancy generates a paramagnetic moment localised on a single site adjacent to the vacancy.

Introduction of a single vacancy on the $A$ sublattice means that the matrix $M$ is now $N-1\times N$ and has only $N-1$ linearly independent columns. Its rank is $N-1$ and therefore is termed rank deficient. Furthermore, there is a single $N$ component vector $\mathbf{y}$ that $M$ maps onto the null vector: $M\mathbf{y}=\mathbf{0}$. Thus the matrix $M$ has a nullity of 1. This guarantees at least one zero energy state with amplitude only on the $B$ sublattice. Analogous conclusions can be reached for $M^T$ and a vacancy on the $B$ sublattice. In the gapped phase and flux free sector, these states have a particularly simple form, with amplitude only on the opposite sublattice to the vacancy and only in a 60° wedge emerging from the vacancy site. For a vacancy on the A(B) sublattice, the zero energy state $\Psi^{A(B)}$ is given by[1]

$$\begin{aligned}
\Psi^B(\mathbf{r}) &= a_0(-1)^{n_1+n_2}\, j_x^{n_1}\, j_y^{n_2}\binom{n_1+n_2}{n_1} && \begin{array}{c} n_1,n_2\geq 0 \\ \text{A sublattice only}\end{array} && \text{0 otherwise} \\
\Psi^A(\mathbf{r}) &= a_0(-1)^{|n_1|+|n_2|} j_x^{|n_1|}\, j_y^{|n_2|}\binom{|n_1|+|n_2|}{|n_1|} && \begin{array}{c} n_1,n_2\leq 0 \\ \text{B sublattice only}\end{array} && \text{0 otherwise.}
\end{aligned} \tag{3.11}$$

$$a_0 = \left((1-j_x^2-j_y^2)^2-4j_x^2j_y^2\right)^{1/4}$$

We note that the normalisation $a_0$ will play a central role in the calculation of the effective paramagnetic moment that forms adjacent to the vacancy. $\Psi^{A(B)}(\mathbf{r})$ can be found directly by iteratively solving the tight binding equations for a zero mode only on one sublattice, starting from a site next to the vacancy:

$$\begin{aligned}
\Psi^B(\mathbf{r})+\Psi^B(\mathbf{r}-\mathbf{n}_1)+\Psi^B(\mathbf{r}-\mathbf{n}_2) &= 0 \\
\Psi^A(\mathbf{r})+\Psi^A(\mathbf{r}+\mathbf{n}_1)+\Psi^A(\mathbf{r}+\mathbf{n}_2) &= 0\ .
\end{aligned} \tag{3.12}$$

[1] We remind the reader that $j_x = J_x/J_z$ and $j_y = J_y/J_z$. As the gap to matter excitations $\Delta$ becomes large, $j_x$ and $j_y$ tend to zero.

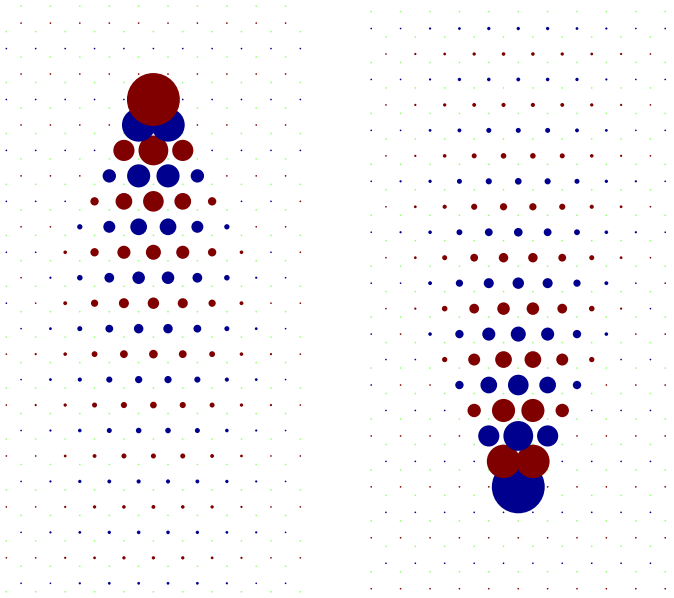



Figure 3.3: Vacancy zero modes found by exact diagonalisation with $J_x = J_y = 1$ and $J_z = 2.5$ and lattice size $36 \times 36$ unit cells. The amplitude on a site is proportional to the area and the sign is denoted by the color. The finite amplitude outside of the cone is a due to the periodic boundary conditions imposed on the lattice.

The binomial factor is the sum of all paths that connect the unit cells at 0 and $\mathbf{r}$. One can then check that the states are normalisable in the gapped phase. Both $\Psi^A(\mathbf{r})$ and $\Psi^B(\mathbf{r})$ decay rapidly with $|\mathbf{r}|$. The short distance behaviour is complicated due to the combinatorial factors but for large $|\mathbf{r}|$, the binomial coefficient can be approximated by a Gaussian. For $j_x = j_y = j$ and $1 \ll |n_1|, |n_2|$.

$$\begin{aligned} \left|\Psi^B(\mathbf{r})\right| &\simeq a_0 j^{n_1+n_2} \sqrt{\frac{2}{\pi(n_1+n_2)}} e^{-(n_1-n_2)^2/2(n_1+n_2)} && n_1, n_2 \geq 0 \\ & && \text{A sublattice only} \\ \left|\Psi^A(\mathbf{r})\right| &\simeq a_0 j^{|n_1+n_2|} \sqrt{\frac{2}{\pi|n_1+n_2|}} e^{-(n_1-n_2)^2/2|n_1+n_2|} && n_1, n_2 \leq 0 \\ & && \text{B sublattice only} \end{aligned} \tag{3.13}$$

The slowest decay is along the wedge axis, where $n_1 = n_2$. The decay in this direction is exponential and generates a length scale for the gapped phase

$$\frac{1}{\xi} = 2\ln(1/j) \tag{3.14}$$

An illustration of these states found by exact diagonalisation is shown in Figure 3.3.

The above zero energy states are for the flux free sector, however, we have already seen that the ground state flux sector has fluxes bound to vacancies. With periodic boundary

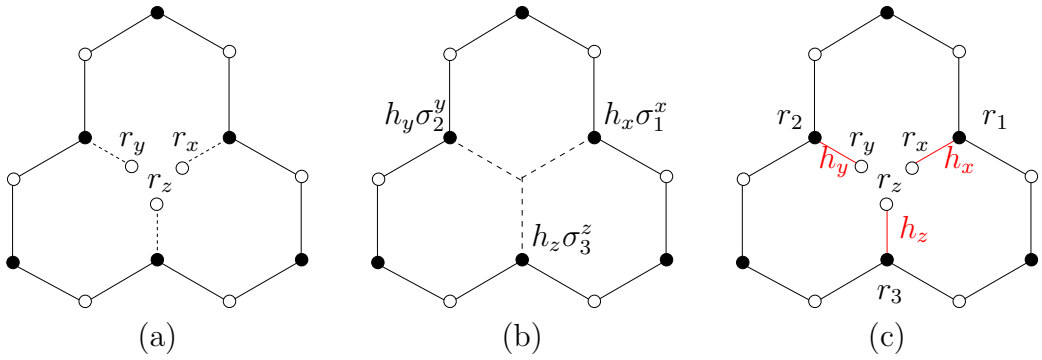



Figure 3.4: a) A vacancy generates a localised state at zero energy but there are also three dangling bond fermions that do not appear in the Hamiltonian. b) Sites at which field components $h_x, h_y$, and $h_z$ contribute linearly to the projected Hamiltonian with a vacancy. c) Sites are coupled with hopping amplitude $h_x, h_y, h_z$ in the equivalent tight binding model.

conditions fluxes must be created in pairs, with a connecting string of $u_{ij} = -1$ bonds between them. We term this a flux string and its path is gauge dependent. With open boundary conditions fluxes can be created in isolation, with the flux string being taken to the boundary of the system. In fact, if a flux is attached to the vacancy plaquette it is easy to show that the sign of $\Psi^{A(B)}(\mathbf{r})$ at a particular site depends on the choice of gauge but the magnitude is unaltered, as expected for a $Z_2$ gauge field.

Since the Kitaev model is a spin Hamiltonian, we might hope to make a correspondence between this localised mode and an effective local moment that may be polarised by an applied magnetic field. However, under the Majorana decomposition, the spins are composite degrees of freedom and eigenstates of the Kitaev Hamiltonian consist of a direct product of a matter state and a massive flux state. We will see that this means the effective local moment generated by a vacancy is constrained to lie on the sites adjacent to the vacancy and which were connected by the strong bonds. For $j_x, j_y \ll 1$ this is site $r_3$ in Figure 3.4(c) and we study the moment formed in this parameter regime.

We investigate the effective moment formed on a single vacancy when we apply a uniform magnetic field $\mathbf{h}$ across the lattice with Zeeman coupling to spins. The Hamiltonian representing this is

$$\widetilde{H} - \sum_j \mathbf{h}\cdot\tilde{\sigma}_j = -J_x \sum_{\text{x-links}} \tilde{\sigma}_j^x\tilde{\sigma}_k^x - J_y \sum_{\text{y-links}} \tilde{\sigma}_j^y\tilde{\sigma}_k^y - J_z \sum_{\text{z-links}} \tilde{\sigma}_j^z\tilde{\sigma}_k^z - \sum_j \mathbf{h}\cdot\tilde{\sigma}_j \ , \qquad (3.15)$$

where $\widetilde{H}$ is the Kitaev Hamiltonian given in Eq. (2.1) and rewritten here for ease of reference. The $Z_2$ fluxes $\widetilde{W}$ no longer commute with the Hamiltonian, rather they become dynamical and the solvability is lost[52]. However, since the gap above the ground state

flux sector $\Delta_W$ scales as in Eq.(3.10), at field strength $h \ll \Delta_W$ one can project onto that flux sector and work perturbatively in $h$. Let $\Pi$ now be a projection operator onto a particular flux sector. Define the Zeeman energy as $\widetilde{V}_{\mathbf{h}} = \sum_j \mathbf{h} \cdot \tilde{\sigma}_j$. The first and second order terms for the clean system are

$$\begin{aligned} \widetilde{H}^{(1)}_{\text{eff}} &= \Pi\ \widetilde{V}_{\mathbf{h}}\ \Pi = 0 \\ \widetilde{H}^{(2)}_{\text{eff}} &= \Pi \sum_n{}' \frac{\widetilde{V}_{\mathbf{h}}|n\rangle\langle n|\widetilde{V}_{\mathbf{h}}}{E_0 - E_n}\Pi\ , \end{aligned} \tag{3.16}$$

where the primed summation is over states that do not belong to the ground state flux sector. Let us assume that all intermediate states in the calculation of $\widetilde{H}^{(2)}_{\text{eff}}$ have an energy $\Delta_W \simeq 2 \times J_z j_x^2 j_y^2/16$ above the ground state, as per Eq. (3.10). In truth, vortices interact and higher order terms in Eq. (3.10) mean that the energy will be a little different to this. However, using this approximation we find

$$\widetilde{H}^{(2)}_{\text{eff}} \sim -\frac{8}{J_z j_x^2 j_y^2}\left( h_x^2 \sum_{\text{x-links}} \tilde{\sigma}_j^x \tilde{\sigma}_k^x + h_y^2 \sum_{\text{y-links}} \tilde{\sigma}_j^y \tilde{\sigma}_k^y + h_z^2 \sum_{\text{z-links}} \tilde{\sigma}_j^z \tilde{\sigma}_k^z \right). \tag{3.17}$$

For the clean system in a weak field the leading order effect is simply to increase the bond strengths

$$J_\alpha \to J_\alpha \left(1 + \frac{8}{j_x^2 j_y^2}\frac{h_\alpha^2}{J_z J_\alpha}\right) \tag{3.18}$$

resulting in a field independent magnetic susceptibility[52].

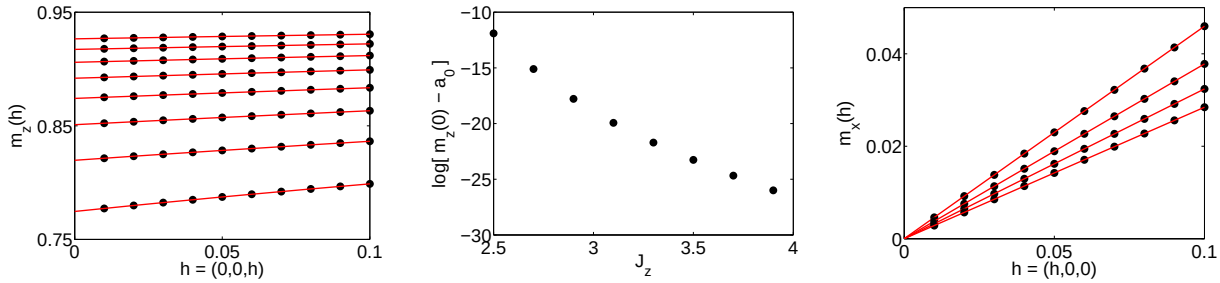
Each bond variable $\hat{u}_{jk}$ in the Kitaev model is composed of two Majorana fermions. Introduction of a vacancy breaks three bonds and leaves three Majorana fermions that do not appear in the Hamiltonian. These are represented in the tight binding model by the addition of three zero energy orbitals $\mathbf{r}_x, \mathbf{r}_y, \mathbf{r}_z$ that are uncoupled from the system, as shown in Figure 3.4(a).

In the presence of a vacancy the first order term $\widetilde{H}^{(1)}_{\text{eff}}$ has elements that are non zero. The Zeeman terms corresponding to the field components and sites indicated in Figure 3.4(b) have non-zero matrix elements between states within the same flux sector and so are the leading order term in our effective perturbation. Employing the site labelling shown there, the projected Zeeman energy is

$$\widetilde{H}_{\text{Z}} = -(h_x \tilde{\sigma}_1^x + h_y \tilde{\sigma}_2^y + h_z \tilde{\sigma}_3^z) \tag{3.19}$$

and the effective Hamiltonian

$$\widetilde{H} + \widetilde{H}_z\ . \tag{3.20}$$




(a) (b) (c)

Figure 3.5: a) The magnetisation of a single vacancy in the gapped phase with $J_x = J_y = 1$ and values of $J_z$ ranging between 2.5 (bottom) and 3.9 (top) with a spacing of 0.2. The field is in the $z$ direction $\mathbf{h} = (0, 0, h)$. Red lines are guides for the eye. The magnetisation is found by exact diagonalisation of the tight binding model of Figure 3.4(c), with a lattice size $20 \times 20$. The plots have a small linear component in $h$ that are a signature of second order terms in $h$ in the Hamiltonian and indicate that $H_{\text{eff spin}}$ is only valid for small $h$. b) Plot of the difference between the moment at $h = 0$ and the analytical moment: $m(0) - a_0$. The very small discrepancy is due to finite size effects that are negligible as the gap becomes large. c) With $J_x = J_y = 1$ and values of $J_z$ ranging between 2.5 (top) and 3.9 (bottom) with a spacing of 0.4 and with a field $\mathbf{h} = (h, 0, 0)$ that produces a small, linear magnetisation $m_x$. The susceptibility decreases as the gap increases.

Remarkably, this Hamiltonian with projected Zeeman energy is exactly solvable by the steps laid out in chapter 2. Note that if a local field were applied with the field components and sites of $\widetilde{H}_Z$ then clearly $\widetilde{H} + \widetilde{H}_Z$ would describe the Kitaev model with a single vacancy and this local field *exactly*, without any of the above requirements on a small field. Written using Majorana fermions, the contributions to $\widetilde{H}_{\text{Z}}$ have the form $h_\alpha \sigma_i^\alpha = i h_\alpha b_i^\alpha c_i$. They can be represented in the tight binding model (2.18) by coupling the zero energy orbitals $\mathbf{r}_x, \mathbf{r}_y, \mathbf{r}_z$ to sites $\mathbf{r}_1, \mathbf{r}_2, \mathbf{r}_3$ with strength $h_x, h_y, h_z$ respectively, as illustrated in Figure 3.4(c). The tight binding model shown here is for a vacancy on the $A$ sublattice but an analogous procedure can be performed for a vacancy on the $B$ sublattice.

The task now is to calculate the field-dependence of the ground state energy of the Kitaev model with a vacancy, using the effective Hamiltonian (3.20), which is represented in the tight binding model of Figure 3.4(c). This will allow us to calculate a vacancy moment with a susceptibility $\chi(h)$, defined as the difference in susceptibility between the disordered and clean systems:

$$\chi(h) = \chi_{\text{disordered}} - \chi_{\text{clean}} \ . \tag{3.21}$$

Let the ground state energy of the effective Hamiltonian (3.20) be $\mathcal{E}(h)$. The vacancy susceptibility is then defined as $\chi(h) = -\partial_h^2 \mathcal{E}(h)$, where, in writing the effective Hamiltonian

in this way, we have already taken into account the difference $\chi_{\text{disordered}} - \chi_{\text{clean}}$. Note that Eq. (3.18) implies that to leading order $\chi_{\text{clean}} \propto N(j_x^2 j_y^2 J_z)^{-1}$, scaling with the size of the system. Therefore, in the limit of large system size $\chi_{\text{clean}}$ will always be much larger than $\chi(h)$ unless the disorder is extensive. Nevertheless, a local probe such as NMR may be used to distinguish vacancy from bulk susceptibilities.

Since the field is small compared to the gap, degenerate perturbation theory can be used, in which, to leading order in $\mathbf{h}$, the effective Hamiltonian couples the orbital $\mathbf{r}_z$ only to the vacancy zero mode with a matrix element proportional to $h_z$. The vacancy mode $\Psi(\mathbf{r})$ has no amplitude on sites $\mathbf{r}_1$ and $\mathbf{r}_2$, and so field components $h_x$ and $h_y$ couple only to states in the band, producing a small, field independent magnetic susceptibility that decreases as the gap becomes large, as shown in Figure 3.5(c). The tight binding model in this approximation is then

$$\begin{pmatrix} 0 & h_z a_0 \\ h_z a_0 & 0 \end{pmatrix} , \tag{3.22}$$

where $a_0$ is the amplitude of the vacancy zero mode on a site adjacent to the vacancy defined in Eq. (3.11). The magnetisation $m_z = -\partial_{h_z}\mathcal{E}(h)$ is independent of $h_z$ in this low field approximation. In general, the interaction of a magnetic moment with a magnetic field is described by a $g$-tensor. For a spin-$\frac{1}{2}$ degree of freedom $\tau^\mu$ the Zeeman energy is $-\tau^\mu g_{\mu\nu} h_\nu$. We normalise $g$ such that a free electron corresponds to a diagonal matrix with entries equal to 1. Using these definitions, the paramagnetic moment that is generated by the vacancy is described by a $g$-tensor and effective Hamiltonian

$$g = \begin{pmatrix} 0 & 0 & 0 \\ 0 & 0 & 0 \\ 0 & 0 & a_0 \end{pmatrix} \qquad H_{\text{eff spin}} = -\tau^\mu_{\mathbf{r}_3} g_{\mu\nu} h_\nu \tag{3.23}$$

The constant $a_0$ vanishes at the boundary of the gapped phase and is equal to one as $j_x, j_y \to 0$, a conclusion corroborating the knowledge that in this limit we have a free spin-$\frac{1}{2}$. It is apparent from the form of the projected Zeeman energy $\widetilde{H}_{\text{Z}}$ that this magnetisation is entirely localized on site $\mathbf{r}_3$ adjacent to the vacancy. Furthermore, the low lying energy levels of the Kitaev model are given by the Zeeman splitting of $H_{\text{eff spin}}$.

In Figure 3.5 we compare the magnetisation that is derived from the effective spin Hamiltonian Eq. (3.23) with that found by exact diagonalisation of the associated tight binding model of Figure 3.4(c). In this sense, Figure 3.5(a) is a test of Hamiltonian (3.23) having made the assumption that the field $h \ll \Delta_W$, so that the Kitaev model can be approximated by $\widetilde{H} + \widetilde{H}_Z$ as in Eq. (3.20). The results of Figure 3.5 were obtained by using the general solution presented in Eq. (2.8). The magnetisation in the ground state

with a finite field is given by

$$\begin{aligned}\langle\sigma_3^z\rangle &= \langle ib_z c_3\rangle = \langle i\sum_{j,k} V_{3,j}c'_{B,j}U_{b_z,k}c'_{A,k}\rangle \\ &= \langle -\sum_{j,k} V_{3,j}U_{b_z,k}(a_j^\dagger - a_j)(a_k^\dagger + a_k)\rangle = \sum_j V_{3,j}U_{b_z,j}\ .\end{aligned} \tag{3.24}$$

Similarly, $\langle\sigma_1^x\rangle = \sum_j V_{1,j}U_{b_x,j}$ and $\langle\sigma_2^y\rangle = \sum_j V_{2,j}U_{b_y,j}$. In the strict limit that $\mathbf{h} = 0$ there is, of course, no spontaneous magnetisation and $\langle\sigma_\alpha\rangle = 0$.

## 3.3 Interaction of moments

We next consider a pair of vacancies, represented by a tight binding model with two vacancies of the type shown in Figure 3.4(a). Throughout, we shall consider vacancies that are not on nearest neighbour lattice sites. In the Kitaev Hamiltonian (2.5) two vacancies lead to six uncoupled Majorana fermions from the six broken bonds. In the tight binding model (2.18) these are represented as six uncoupled zero energy orbitals. There will also be two localised modes roughly of the form shown in Figure (3.3). If the vacancies are on the same sublattice, these localised modes are both at zero energy. Two vacancies on the same sublattice therefore lead to two effective paramagnetic moments, each of the same form as for a single vacancy. This process may be iterated to include a number of well separated vacancies on the same sublattice, that will give rise to the same number of isolated paramagnetic moments. If the separation between two vacancies becomes smaller than the decay length of the zero modes in Eq. (3.11) then the loss of sites will affect the normalisation of the wavefunctions and hence the magnitude of the paramagnetic moment. More precisely, the magnitude will increase as the lattice is diluted until every site on one sublattice is removed and the lattice consists of isolated spin-$\frac{1}{2}$ degrees of freedom. At this point the normalisation is such that $a_0 = 1$.

If the vacancies are on opposite sublattices the vacancy modes hybridise, forming states within the gap at $\pm E$. We will show that in this situation the effective moments interact with an exchange coupling characterised by the energy $E$, which we will evaluate. Using the $g$-tensor introduced for the single vacancy calculation, applying local fields $h_1$ and $h_2$ at the two vacancy sites, the effective spin Hamiltonian is

$$\begin{aligned}H_{\text{eff spin}} &= E\tau_1^x\tau_2^x - \tau_1^\mu g_{\mu,\nu}h_{1,\nu} - \tau_2^\mu g_{\mu,\nu}h_{2,\nu} \\ &= E\tau_1^x\tau_2^x - a_0\tau_1^z h_{1,z} - a_0\tau_2^z h_{2,z}\end{aligned} \tag{3.25}$$

The magnitude of the magnetic moment formed on the site adjacent to each vacancy in the Kitaev model is given by the expectation values $\langle a_0\tau_1^z\rangle$ and $\langle a_0\tau_2^z\rangle$. Matrix elements for the

other components $\langle a_0\tau_i^x\rangle = \langle a_0\tau_i^y\rangle = 0$. Note that these effective spins do not themselves correspond to the original spins in the Kitaev model nor the effective moments that form upon the introduction of vacancies . For instance, at $\mathbf{h} = 0$, spin correlations in the Kitaev model remain nearest neighbour in the presence of vacancies but the above effective spin Hamiltonian would falsely imply a finite matrix element $\langle\tau_1^x\tau_2^x\rangle$. $H_{\text{eff spin}}$ should therefore be used simply as a tool with which to calculate the z-component of the effective magnetic moment of two vacancies in the Kitaev model.

We will now show how the energy $E$ may be derived and how to obtain the effective Hamiltonian (3.25). Much work here and in this thesis as a whole will depend on Green function equations and standard T-matrix formalism. For a Hamiltonian $H = H_0 + V$ and associated Green functions $G$ and $G_0$, the T-matrix is defined through the Green function equations

$$\begin{aligned} G = &\quad G_0 + G_0 T G_0 \\ T = &\quad V(1 - G_0 V)^{-1} \end{aligned} \tag{3.26}$$

In the current case we seek to find the energy levels of the Kitaev Hamiltonian with two vacancies in the ground state flux sector, with fluxes attached to the vacancy plaquettes. We therefore chose as our reference system $H_F$, the tight binding model for the hexagonal lattice without vacancies but with fluxes attached to one plaquette adjacent to each site where a vacancy will be placed. Once the vacancies are included, this will leave the system in the correct ground state flux sector. We introduce into the model a potential $V = 1/\epsilon$ at the two sites and take the limit $\epsilon \to 0$ to represent the effect of the two vacancies on those sites. This introduces new poles into the Green function in the gap and these poles are the energy levels $\pm E$ that we seek.

Let the $B$ vacancy be in the unit cell at the origin and the $A$ vacancy in a unit cell at $\mathbf{r}$. We require matrix elements of the Green function $G_F^{\alpha\beta}(\mathbf{r}, \mathbf{r}')$ for an undiluted lattice with fluxes attached to one of the plaquettes adjacent to each vacancy. Here, $\alpha, \beta$ are sublattice indices. Using Eq. (3.26), the T-matrix for the perturbation used to generate the vacancies spans a $2 \times 2$ subspace consisting of elements between sites 0 and $\mathbf{r}$:

$$\begin{aligned} T &= \lim_{\epsilon\to 0} \begin{pmatrix} 1/\epsilon & 0 \\ 0 & 1/\epsilon \end{pmatrix} \left[ \begin{pmatrix} 1 & 0 \\ 0 & 1 \end{pmatrix} - \begin{pmatrix} G_F^{AA}(\mathbf{r},\mathbf{r}) & G_F^{AB}(\mathbf{r},\mathbf{0}) \\ G_F^{BA}(\mathbf{0},\mathbf{r}) & G_F^{BB}(\mathbf{0},\mathbf{0}) \end{pmatrix} \begin{pmatrix} 1/\epsilon & 0 \\ 0 & 1/\epsilon \end{pmatrix} \right]^{-1} \\ &= - \begin{pmatrix} G_F^{AA}(\mathbf{r},\mathbf{r}) & G_F^{AB}(\mathbf{r},\mathbf{0}) \\ G_F^{BA}(\mathbf{0},\mathbf{r}) & G_F^{BB}(\mathbf{0},\mathbf{0}) \end{pmatrix}^{-1} \end{aligned} \tag{3.27}$$

The new Green function will have poles when the determinant of the above $2\times 2$ matrix is zero. Using the following identities $G_F^{AA}(\mathbf{r},\mathbf{r}) = G_F^{BB}(\mathbf{0},\mathbf{0})$ and $G_F^{AB}(\mathbf{r},\mathbf{0}) = G_F^{BA}(\mathbf{0},\mathbf{r})$.

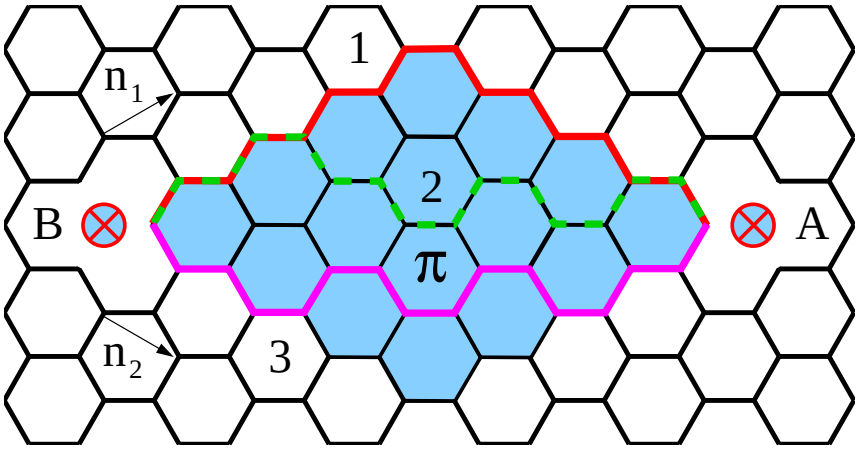



Figure 3.6: The combinatorial part of $G_0^{BA}(0,\mathbf{r})$ between two vacancy sites comes from the number of paths of length $|n_1|+|n_2|$ that connect the two vacancy unit cells. This defines a region $\mathcal{R}$ shaded in blue. Here $n_1 = n_2 = 4$. Paths that travel above the flux, e.g. 1 and 2, come with opposite sign to paths that travel below, e.g. 3, meaning that not all paths add in phase. Note that in this set up, if the A vacancy were to the left of the B vacancy then $G_0^{BA}(0,\mathbf{r}) = 0$

The hybridisation energy will then be given by solutions to the equation

$$G_F^{AA}(\mathbf{r},\mathbf{r})^2 - G_F^{BA}(\mathbf{0},\mathbf{r})^2 = 0. \tag{3.28}$$

In general, $G_F^{\alpha\beta}(\mathbf{0},\mathbf{r})$ cannot be found analytically. However, much information can be garnered by first considering the Green function in the flux free sector, $G_0^{\alpha\beta}(\mathbf{0},\mathbf{r})$. We will see that $E$ decreases exponentially with vacancy separation. If this energy is small compared to the gap $\Delta$, an expansion can be performed using $E/\Delta$ as a small parameter to find the asymptotic form for $G_0^{\alpha\beta}(\mathbf{0},\mathbf{r})$ (see Appendix A), giving

$$\begin{aligned} G_0^{AA}(\mathbf{0},\mathbf{0}) &= \frac{-E}{J_z^2\sqrt{(1-j_x^2-j_y^2)^2-4j_x^2j_y^2}} + O\left[\tfrac{1}{J_z}\left(\tfrac{E}{\Delta}\right)^3\right] \\ G_0^{BA}(\mathbf{0},\mathbf{r}) &= \frac{(-1)^{n_1+n_2+1}}{J_z} j_x^{n_1} j_y^{n_2} \binom{n_1+n_2}{n_1} + O\left[\tfrac{1}{J_z}\left(\tfrac{E}{\Delta}\right)^2\right] \qquad n_1, n_2 \geq 0,\ 0 \text{ otherwise.} \end{aligned} \tag{3.29}$$

The similarity with Eq. (3.11) is clear since $G_0^{BA}(\mathbf{0},\mathbf{r})$ evaluated at $E = 0$ satisfies the equations for a vacancy zero mode, albeit with a different normalisation:

$$J_z G_0^{BA}(0,\mathbf{r}) + J_x G_0^{BA}(0,\mathbf{r}-\mathbf{n}_1) + J_y G_0^{BA}(0,\mathbf{r}-\mathbf{n}_2) = -\delta_{\mathbf{r},\mathbf{0}}. \tag{3.30}$$

where $\delta_{\mathbf{r},\mathbf{0}}$ is the Kronecker delta function. In the same manner as $\Psi(\mathbf{r})$, the leading order term in $G_0^{BA}(\mathbf{0},\mathbf{r})$ is nonzero only inside a 60° wedge emerging from the origin and is

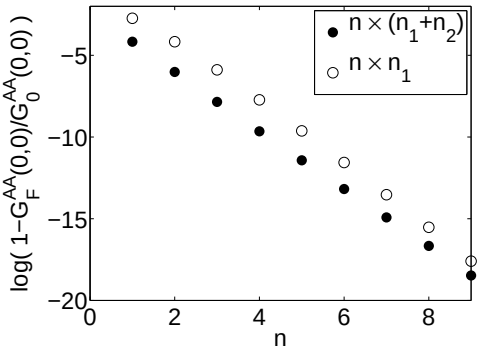



Figure 3.7: We plot $1 - G_F^{AA}(\mathbf{0},\mathbf{0})/G_0^{AA}(\mathbf{0},\mathbf{0})$, evaluated at $E = 0$ and with a flux at the origin and one at $\mathbf{r}$ for $\mathbf{r} = n(\mathbf{n}_1 + \mathbf{n}_2)$ and $\mathbf{r} = n\mathbf{n}_1$. Here, $J_x = J_y = 1$ and $J_z = 3$. The two Green functions are identical in the limit $|\mathbf{r}|/\xi \gg 1$

a product of an exponential decay in length $n_1$ and $n_2$ and a combinatorial part. The combinatorial part is given by the number of paths of length $n_1 + n_2$ between the origin and the unit cell at $\mathbf{r}$. In the absence of fluxes all these paths add constructively. In the presence of fluxes this is no longer always true. We discuss the implications of this for both $G_F^{BA}(\mathbf{0},\mathbf{r})$ and the interaction energy $E$ below. In the following discussion we approximate $G_0^{AA}(\mathbf{0},\mathbf{0})$ and $G_0^{BA}(\mathbf{0},\mathbf{r})$ by the leading order terms in Eq. (3.29) only.

The maximal extent of the paths of length $n_1 + n_2$ between the origin and $\mathbf{r}$ defines a region $\mathcal{R}$. This region is also the area of overlap between the two vacancy modes. If there are a number of fluxes inside $\mathcal{R}$ then each path comes with a relative sign given by the number $N_{FS}$ of flux strings crossed: $(-1)^{N_{FS}}$. An example region $\mathcal{R}$ is depicted in Figure 3.6. The magnitude of $G_F^{BA}(\mathbf{0},\mathbf{r})$ is of course gauge independent and dependent only on the location of fluxes. A number of conclusions can be drawn immediately: in the presence of fluxes $G_F^{BA}(\mathbf{0},\mathbf{r})$ is also zero outside of the 60° wedge; if there are no fluxes inside $\mathcal{R}$, $G_F^{BA}(\mathbf{0},\mathbf{r})$ has the same amplitude as $G_0^{BA}(\mathbf{0},\mathbf{r})$, with no restriction on fluxes outside $\mathcal{R}$; if there are some fluxes inside $\mathcal{R}$ then some paths interfere destructively and $G_F^{BA}(\mathbf{0},\mathbf{r})$ has smaller amplitude than $G_0^{BA}(\mathbf{0},\mathbf{r})$. The Green function $G_0^{BA}(\mathbf{0},\mathbf{r})$ is characterised by a length scale $\xi$ that is the same as that found earlier for the vacancy zero modes in Eq. (3.14). For vacancy separation $\mathbf{r} = n_1\mathbf{n}_1 + n_2\mathbf{n}_2$, non-zero $E$ requires $0 \leq n_1, n_2$

Numerically we find that the denominator of the leading order term of $G_0^{AA}(\mathbf{0},\mathbf{0})$ is unaffected by this change of flux sector, i.e. $G_F^{AA}(\mathbf{0},\mathbf{0}) \times E^{-1} \sim G_0^{AA}(\mathbf{0},\mathbf{0}) \times E^{-1}$ in the limit $|\mathbf{r}|/\xi \gg 1$, as demonstrated in Figure 3.7. In summary, for a system of two vacancies in the ground state flux sector, such that fluxes are bound to both vacancies but there are no more elsewhere, to leading order the hybridisation energy will be the same as that in the flux free sector.

Having found the interaction energy $E$ using the tight binding model, we are now in a position to calculate the magnetisation of the pair of vacancies. If $E/\Delta \ll 1$, the hybridised wavefunction will be approximated by two single vacancy wavefunctions of the type shown in Eq. (3.11). As for the single vacancy calculation, only the $h_z$ component of the field couples zero energy orbitals to the hybridised levels at $\pm E$. The leading order field dependent energy is determined by the tight binding model projected onto this four state subspace:

$$\frac{1}{\sqrt{2}}\begin{pmatrix} 0 & 0 & h_2 a_0 & h_2 a_0 \\ 0 & 0 & h_1 a_0 & -h_1 a_0 \\ h_2 a_0 & h_1 a_0 & \sqrt{2}E & 0 \\ h_2 a_0 & -h_1 a_0 & 0 & -\sqrt{2}E \end{pmatrix}, \tag{3.31}$$

which has eigenvalues $\pm S_\pm$

$$\begin{aligned} S_+ &= \tfrac{1}{2}\left(\sqrt{E^2+(h_1+h_2)^2}+\sqrt{E^2+(h_1-h_2)^2}\right) \\ S_- &= \tfrac{1}{2}\left|\sqrt{E^2+(h_1+h_2)^2}-\sqrt{E^2+(h_1-h_2)^2}\right|. \end{aligned} \tag{3.32}$$

The Kitaev Hamiltonian with two vacancies on opposite sublattices and a small, uniform magnetic field is approximately given by

$$H_u = S_+(2a_+^\dagger a_+ - 1) + S_-(2a_-^\dagger a_- - 1) + \sum_{\text{band}} S_j(2a_j^\dagger a_j - 1). \tag{3.33}$$

The summation is over states in the band and to leading order depends quadratically on $h$, contributing a small field independent susceptibility on every site, as for the clean system. The first two terms govern the magnetic behaviour of the impurities and lead to the following low lying energy levels

$$\begin{array}{rl|rl} \multicolumn{2}{c|}{\text{sgn}(h_1)=\text{sgn}(h_2)} & \multicolumn{2}{c}{\text{sgn}(h_1)\neq\text{sgn}(h_2)} \\ -S_+-S_- &= -\sqrt{E^2+a_0^2(h_1+h_2)^2} & -S_+-S_- &= -\sqrt{E^2+a_0^2(h_1-h_2)^2} \\ -S_++S_- &= -\sqrt{E^2+a_0^2(h_1-h_2)^2} & -S_++S_- &= -\sqrt{E^2+a_0^2(h_1+h_2)^2} \\ S_+-S_- &= \sqrt{E^2+a_0^2(h_1-h_2)^2} & S_+-S_- &= \sqrt{E^2+a_0^2(h_1+h_2)^2} \\ S_++S_- &= \sqrt{E^2+a_0^2(h_1+h_2)^2} & S_++S_- &= \sqrt{E^2+a_0^2(h_1-h_2)^2} \end{array} \tag{3.34}$$

Using a basis for two spin-$\frac{1}{2}$ degrees of freedom $|\tau_1^z\tau_2^z\rangle$, $\{|\uparrow\uparrow\rangle, |\uparrow\downarrow\rangle, |\downarrow\uparrow\rangle, |\downarrow\downarrow\rangle\}$ the effective spin Hamiltonian given earlier in Eq. (3.25) is

$$E\tau_1^x\tau_2^x - a_0\tau_1^z h_{1,z} - a_0\tau_2^z h_{2,z} = \begin{pmatrix} a_0(-h_1-h_2) & 0 & 0 & E \\ 0 & a_0(-h_1+h_2) & E & 0 \\ 0 & E & a_0(h_1-h_2) & 0 \\ E & 0 & 0 & a_0(h_1+h_2) \end{pmatrix} \tag{3.35}$$

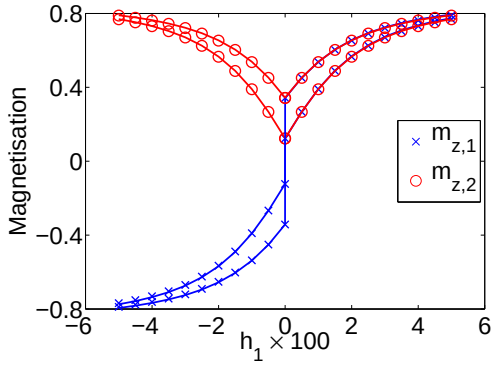



Figure 3.8: Solid lines are the magnetisation found by exact diagonalisation of a tight binding model for a system of one A and one B vacancy and projected Zeeman energy as in Eq. (3.20). A lattice size $20 \times 20$ on periodic boundary conditions was used with $J_x = J_y = 1, J_z = 3$. Markers are the magnetisation found by the effective spin Hamiltonian with an interaction energy $E = 2.38 \times 10^{-2}$ obtained from exact diagonalisation in zero field. All fields are taken in the z-direction only $\mathbf{h} = (0, 0, h)$. From the top, we plot $m_z$ vs. $h_1$ for $h_2 = E/2$ and $h_2 = E/6$. Here the moment has magnitude $a_0 = (5/9)^{1/4} \simeq 0.863$.

Ignoring the states in the band, it is clear that this effective spin Hamiltonian has the same ground state energy and set of excitations as the Kitaev Hamiltonian Eq. (3.33).

The magnetisation $m_z$ for this effective spin Hamiltonian and that found by exact diagonalisation of the tight binding model corresponding to the Kitaev Hamiltonian with projected Zeeman energy, as in Eq. (3.20), are in very good agreement as shown in Figure 3.8.

For $h_1 = h_2 = h$, this gives a combined impurity moment

$$m_z(E, h) = \frac{4ha_0^2}{\sqrt{E^2 + 4h^2a_0^2}} \tag{3.36}$$

As for the single vacancy calculation, from the projected form of the Zeeman energy, it is apparent that this moment is entirely localised on the sites equivalent to $\mathbf{r}_3$ in Figure 3.4(b), adjacent to each vacancy. For fields $h \ll E$ there is a large, field independent vacancy susceptibility $\chi = 4a_0^2/E$. Since $E$ is exponentially small in vacancy separation this susceptibility is much larger than that of the clean system per site. For $E \ll h \ll 1$ the moment saturates to $2a_0$, which is twice the isolated vacancy moment.

## 3.4 Finite density of vacancies

The approach outlined above to the two vacancy problem using T-matrix formalism can be extended to include a finite density of vacancies. We study a system with $N_{A(B)}$ vacancies

on the $A(B)$ sublattice. If $N_A = N_B$, we say that the vacancies are compensated, if $N_A \neq N_B$, we say that the vacancies are uncompensated.

First, consider the compensated case and let $G_F^{AA}$, $G_F^{BB}$ and $G_F^{BA}$ be $N_A \times N_A$ matrices of Green function elements evaluated between sites where vacancies will be introduced. Analogously to the two vacancy problem, the hybridised energy levels are given by the solution to the following determinant equation

$$\begin{vmatrix} G_F^{AA} & (G_F^{BA})^{\mathrm{T}} \\ G_F^{BA} & G_F^{BB} \end{vmatrix} = 0, \tag{3.37}$$

where, as before, the subscript $F$ denotes the Green function for a system that has fluxes on one plaquette adjacent to each site where a vacancy will be introduced. We assume that the vacancies are well separated in the sense that the distance between vacancies $|\mathbf{r}|$ satisfies $1 \ll \mathbf{r}/\xi$. The diagonal elements of $G_F^{AA}$ and $G_F^{BB}$ will then be much larger than the off diagonal elements and the Green function elements can be approximated to lowest order in an expansion in $E/\Delta$, given in (3.29). Setting the off diagonal elements of $G_F^{AA}$ and $G_F^{BB}$ to zero, the above determinant equation is equivalent to

$$\begin{vmatrix} E & \dfrac{(G_F^{BA})^{\mathrm{T}}}{\partial_E G_F^{AA}(\mathbf{0},\mathbf{0})|_{E=0}} \\ \dfrac{G_F^{BA}}{\partial_E G_F^{AA}(\mathbf{0},\mathbf{0})|_{E=0}} & E \end{vmatrix} = 0, \tag{3.38}$$

In this way we can see that the hybridised energy levels are approximated by the eigenenergies of a bipartite hopping Hamiltonian

$$H_{\mathrm{BPH}} = \frac{1}{\partial_E G_F^{AA}(\mathbf{0},\mathbf{0})|_{E=0}} \begin{pmatrix} 0 & (G_F^{BA})^T \\ G_F^{BA} & 0 \end{pmatrix}. \tag{3.39}$$

For uncompensated vacancies, the nullity of $G_F^{BA} = |N_A - N_B|$ and there are guaranteed to be $|N_A - N_B|$ exact zero energy states. In addition there are $3(N_A + N_B)$ uncoupled, zero energy orbitals, that come from the three broken bonds to each vacancy. The remaining states form an impurity band with a divergent density of states as $E \to 0$. For compensated vacancies with periodic boundary conditions, the local modes associated with every vacancy mix, forming the impurity band and there remain only the $3(N_A + N_B)$ orbitals from the broken bonds at zero energy. The form of the divergence in the density of states, the nature of the states within the impurity band and the resulting susceptibility are the subject of the remainder of this chapter.

With open boundary conditions, a vacancy that has a mode as in Eq. (3.11) that does not overlap with a vacancy on the opposite sublattice will give an additional zero energy

state. Furthermore, there will be a number of edge states at zero energy that depends on the sublattice imbalance at the edge. For simplicity we consider only systems with periodic boundary conditions.

The Hamiltonian of Eq. (3.39) has entries that vary exponentially with vacancy separation, so the couplings vary over many orders of magnitude and it thus has similarities with the well studied problem of strong disorder bipartite random hopping (BPRH). Here the density of states diverges as $\rho(E) = \mathcal{F}(E)/E$, where $\mathcal{F}(E)$ goes to zero more slowly than any power of $E$ and ensures that the density of states remains integrable[36, 68]. Numerically we find the density of states for a finite density of vacancies in the ground state flux sector of the Kiteav honeycomb model to be of this form, as shown in Figure 3.9(a). The exact form of $\mathcal{F}(E)$ is difficult to ascertain. However, our numerics suggest a functional form

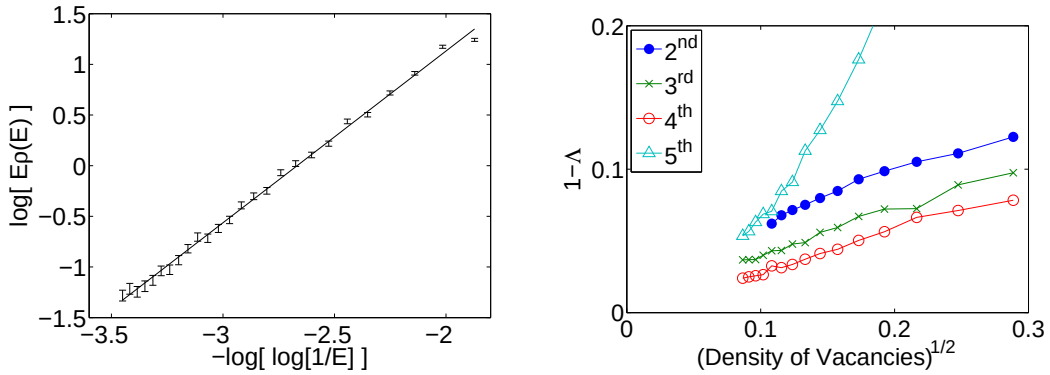
$$\mathcal{F}(E) \propto \frac{1}{\log[1/E]^{1.7}} \ . \tag{3.40}$$

Note, however, that since $\mathcal{F}(E)$ is such a slowly varying function of $E$, precision in the exponent is difficult to achieve: in Figure 3.9 the points used to determine Eq. (3.40) vary over less than a factor of two.

Any particular state will be a hybridisation of impurity modes, of the form in Eq. (3.11), centered on each vacancy site. However, at low vacancy concentration we find that the vacancy modes hybridise into isolated A-B pairs via the same mechanism as for the strong disorder BPRH. This was the real space renormalisation group procedure introduced to describe the low lying states of the strong disorder spin-$\frac{1}{2}$ Heisenberg antiferromagnetic chain in section 1.2.1.

We confirm this numerically by the following method. A hybridised state of well separated vacancies may be approximated as $\sum_{j=1}^{M} A_j \Psi_j^A(\mathbf{r} - \mathbf{r}_j) + \sum_{k=1}^{M} B_k \Psi_k^B(\mathbf{r} - \mathbf{r}_k)$ where $\Psi^{A(B)}(\mathbf{r} - \mathbf{r}_j)$ is a vacancy zero mode of the form given in Eq. (3.11) for an $A(B)$ vacancy in unit cell $\mathbf{r}_j$. Without loss of generality, let $|A_1| \geq |A_2| \geq \cdots \geq |A_M|$ and $|B_1| \geq |B_2| \geq \cdots \geq |B_M|$. A measure of the localisation of a state is given by $\Lambda = (A_1^2 + B_1^2)/2a_0^2$, with $\Lambda = 1$ for an isolated pair. Note that $A_j a_0$ and $B_k a_0$ are the amplitude on the sites equivalent to $\mathbf{r}_3$ in Figure 3.4(c) associated with each vacancy. If the vacancies are not well separated then the above decomposition into vacancy modes is not an accurate representation of the state. Nevertheless, we obtain a value for $\Lambda$ by measuring the amplitudes on each of the sites equivalent to $\mathbf{r}_3$ next to the vacancies.

In this manner, we place 24 compensated vacancies randomly on a lattice with periodic boundary conditions and obtain 12 pairs of states in the gap, each with a corresponding value of $\Lambda$. We do this many times (between 1400 for the largest and 3600 for the smallest




(a) (b)

Figure 3.9: (a) Density of states for 160 randomly placed compensated vacancies on a lattice of 3200 sites, with fluxes attached to vacancies and with $J_x = J_y = 1$, $J_z = 4$. The density of states was found by averaging over 1000 disorder realisations. Solid line is a best fit to the data with gradient of 1.7. (b) With $\Lambda$ defined in the text, we plot $1 - \bar{\Lambda}$ for different fifths of energy. All curves tend to zero as the vacancy density goes to zero indicating hybridisation into isolated pairs of vacancies.

lattices) and in this way obtain a spectrum of states. We then separate this spectrum by energy into fifths and plot the average $(1 - \bar{\Lambda})$ in the $2^{nd}, 3^{rd}, 4^{th}$ and $5^{th}$ fifths. The lowest fifth in energy has entries below machine precision and is not plotted. In Figure 3.9(b) we can see that all curves tend to zero as the density tends to zero, indicating that all hybridised states appear to form isolated pairs in this limit.

For vacancy modes that hybridise into an isolated pair, the magnetisation is given by Eq. (3.36). Assuming that all vacancy modes are of this kind, the total magnetisation and susceptibility are

$$\begin{aligned} m_z(h) &= \int m_z(E,h)\rho(E)dE \\ \chi(h) &= \int \frac{4a_0^2 E}{(E^2 + 4a_0^2h^2)^{3/2}}\mathcal{F}(E)dE \end{aligned} \tag{3.41}$$

The susceptibility integral has its dominant contribution from a region around $E = \sqrt{2}a_0 h$. Since $\mathcal{F}(E)$ goes to zero more slowly than any power of $E$, it is a slowly varying function over this region and the susceptibility is approximately

$$\chi(h) \simeq \int \frac{4a_0^2 E}{(E^2 + 4a_0^2h^2)^{3/2}}\mathcal{F}\left(\sqrt{2}a_0 h\right) dE \propto \mathcal{F}\left(\sqrt{2}a_0 h\right) h^{-1} \tag{3.42}$$

The physical picture of the total magnetisation is the following. Since there is a divergent density of states, the majority of pairs with energy $E < h$ will be completely polarised and the majority with $E > h$ will be completely unpolarised. The fraction of states with

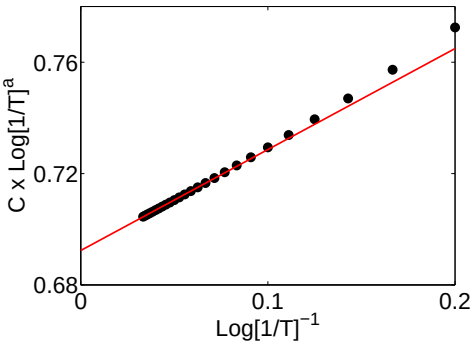



Figure 3.10: Numerical integration of Eq. (3.46) to determine the low temperature heat capacity for the gapped phase in the presence of vacancies. Red line is a guide for the eye.

energy $E \simeq h$ that cannot be considered fully polarised or fully unpolarised will be small and gives a subleading contribution to the magnetisation. At a finite temperature $T$, the leading order susceptibility can be found by considering all pairs with energy $E < T$ to be essentially free and to have a Curie response. Pairs with $E > T$ have a very small response and will give a subleading contribution. Assuming a functional form for the density of states as in Eq. (3.40) $\rho(E) \sim [E \log(1/E)^a]^{-1}$, the susceptibility at finite T is

$$\chi(T) \sim \int_0^T \frac{1}{T}\rho(E)dE \propto \frac{1}{T\ \log(1/T)^{a-1}} \tag{3.43}$$

### 3.4.1 Heat capacity

We have seen that the introduction of a finite density of vacancies leads to an impurity band with a divergent density of states. This will clearly have a dramatic effect on the low temperature heat capacity, which we investigate now.

For the clean system, the density of states may be found from the site diagonal Green function, as outlined in Appendix. A. For energies close to the band edge, the density of states is given by

$$\rho(E) \simeq \begin{cases} \alpha + \beta E & \Delta \leq E \\ 0 & E < \Delta \end{cases} , \tag{3.44}$$

where the constants $\alpha$ and $\beta$ depend on the parameters $J_x, J_y$ and $J_z$. This leads to an exponentially small heat capacity for the clean system

$$C_{\text{clean}} \sim \alpha\Delta e^{-\Delta/T} . \tag{3.45}$$

To find the heat capacity for a system with a finite density of vacancies we use the

functional form for $\mathcal{F}(E)$ given in Eq. (3.40). In the following, $f(E)$ is the Fermi function:

$$\begin{aligned} C = & \ \partial_T \int_0^{E_{\max}} E\rho(E)f(E)dE = \partial_T \int_0^{E_{\max}} E\frac{1}{E\log(1/E)^a}\frac{1}{e^{E/T}+1}dE \\ = & \ \int_0^{E_{\max}/T} \frac{xe^x}{(\log(1/xT)^a(e^x+1)^2}dx \end{aligned} \tag{3.46}$$

For small $T$, $[\log(1/xT)]^{-a}$ is a slowly varying function of $x$ over the dominant contribution to the integral Eq. (3.46). Therefore, we use only the leading order term in a Taylor expansion of this function to obtain the leading order temperature dependence of the heat capacity and find

$$C \propto \frac{1}{\log(1/T)^a} + O\left(\frac{1}{\log(1/T)\log(1/T)^a}\right) . \tag{3.47}$$

We confirm this numerically in Figure 3.10. Clearly the introduction of vacancies has a profound effect on the heat capacity: it is exponentially small in $1/T$ for the clean system but is only logarithmically small in $T$ for the system with vacancies.

# Chapter 4

# Site dilution in the Gapless Phase

We have seen in chapter 3 that in the gapped phase the vacancy modes form hybridised states in the gap. For weak fields the leading order magnetic properties of the Kitaev model with vacancies may be obtained by considering changes to the energy of only these levels. By contrast, in the gapless phase hybridised states appear as resonances in the continuum of states and no such separation of vacancy and band states is possible, making calculations significantly more difficult. Furthermore, in the gapped phase it is easy to overcome finite size effects when performing a numerical analysis. In the gapless phase however, vacancy modes are only quasi-localised[74], making it exceedingly difficult to simulate the thermodynamic limit. The upside of this increase in complexity is that vacancy properties in the gapless phase are more subtle, although several features of the gapped phase remain.

This chapter is organised as follows. In section 4.1 we begin an exploration of the properties of the gapless phase with site dilution by showing that vacancies also bind a flux in this phase. In section 4.2 we then move on to describe the magnetic properties of the Kitaev model in the gapless phase with vacancies in a uniform magnetic field. We find that a vacancy moment forms on the three sites adjacent to the vacancy and with a divergent susceptibility $\chi(h) \sim \log(1/h)$. This is in contrast to the susceptibility of the clean system, which is a constant to leading order in $h$. The vacancy susceptibility is defined in the same was as in chapter 3 and Eq. (3.21). In section 4.3 we see that for two vacancies, the magnetic response is dependent on the relative sublattices of the vacancies. If they are on opposite sublattices, interactions between the vacancy moments cuts off the divergence in susceptibility present for an isolated vacancy at a large but finite constant at small $h$. For well separated vacancies, this susceptibility will be much larger than that of the clean system. Two vacancies on the same sublattice behave quite differently. Here the susceptibility diverges as $\chi(h) \sim [h(\log(1/h))^{3/2}]^{-1}$ at small $h$, parametrically faster than that of an isolated vacancy. The results given in this paragraph are the central results of

this chapter and are summarised below. In the gapless phase and to leading order in $h$ the vacancy susceptibility of the Kitaev model is given by

$$\chi(h) \propto \begin{cases} \log(1/h) & \text{Isolated vacancy} \\ \textit{large constant} & \text{two vacancies on opposite sublattices} \\ \dfrac{1}{h[\log(1/h)]^{3/2}} & \text{two vacancies on the same sublattice} \end{cases} \tag{4.1}$$

In the final section of this chapter, section 4.4 we comment on finite size effects in the gapless phase.

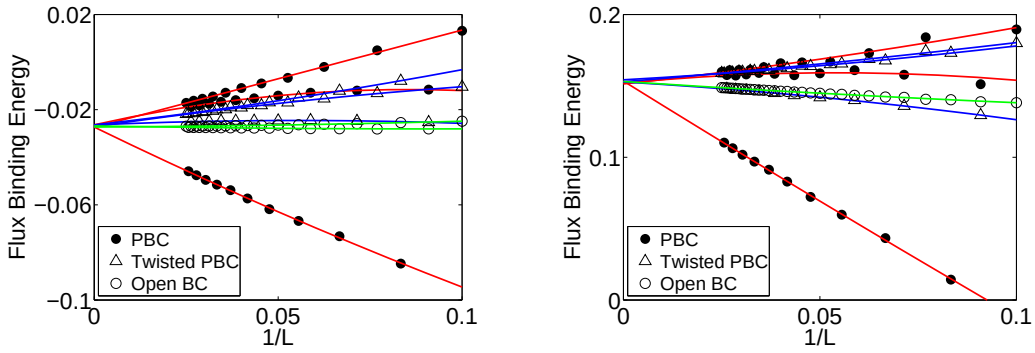
For simplicity, throughout this chapter we set $J_\alpha = J > 0$ for all $\alpha$, although all of the results presented are qualitatively similar throughout the gapless phase.

## 4.1 Flux binding

In the gapped phase we are able to use a perturbative expansion to study flux binding. This expansion is based on the flux through loops defined on the lattice, and, deep in the gapped phase, only the shortest loops are important. By contrast, in the gapless phase the flux through loops of all length now contribute to the effective Hamiltonian (3.10) and the perturbative expansion used in the gapped phase is no longer useful. Instead, as we explain below, numerics can be used to show that the flux binding energy for a vacancy is $-0.027J$ and of a hexagonal plaquette $+0.153J$. The smaller in magnitude of these determines the gap to flux excitations, which is

$$\Delta_W \simeq 0.027J \tag{4.2}$$

Specifically, we find the change in ground state energy of the Kitaev model when fluxes are bound to vacancy plaquettes, i.e. we find the change to the sum $-\sum_m S_m$ introduced in Eq. (2.8) and evaluated by exact diagonalisation of the tight binding model (2.18). In Figure 4.1(a) we consider lattices of size $L \times L$, with periodic boundary conditions (PBC) and twisted PBC. In the latter the unit cells at $((L+n_1)\mathbf{n}_1, n_2\mathbf{n}_2)$ and $(n_1\mathbf{n}_1, (1+n_2)\mathbf{n}_2)$, and $(n_1\mathbf{n}_1, (L+n_2)\mathbf{n}_2)$ and $((1+n_1)\mathbf{n}_1, n_2\mathbf{n}_2)$ are equivalent. Since fluxes must be created in pairs, we find the energy change of binding fluxes to two vacancies separated by $\frac{L}{2}(\mathbf{n}_1 + \mathbf{n}_2)$, so that there is a single length scale in the problem. In the same figure we also show the flux binding energy of a single vacancy at the center of a lattice with open boundary conditions (open BC). In this case the flux string may be taken to the edge of the lattice. Finally, for both boundary conditions we take the limit of large system size, where the flux binding energy from all three boundary conditions converge.




(a) (b)

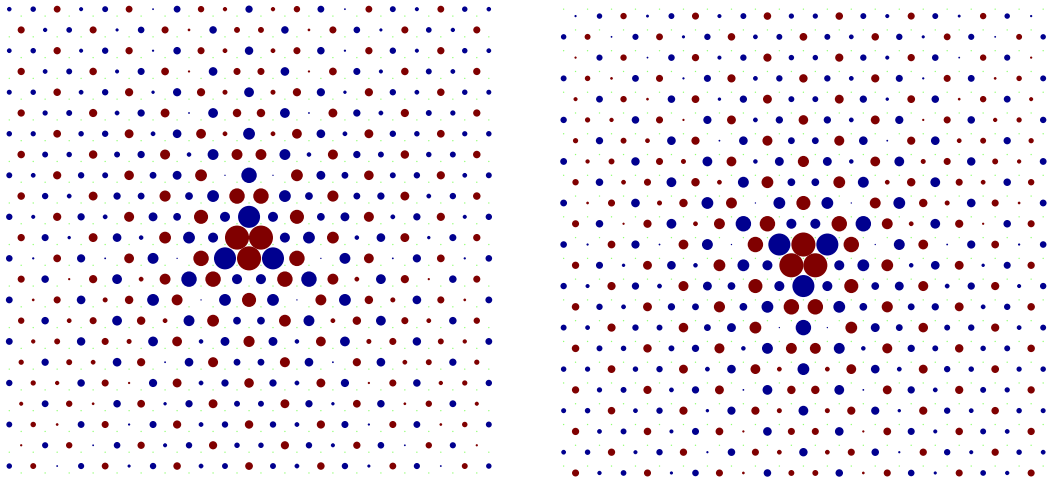
Figure 4.1: a) The energy cost of binding a flux to an isolated vacancy plaquette $-0.027J$. Details of the numerical calculation are given in the text. b) For comparison, the energy cost of binding a flux to a hexagonal plaquette is $+0.153J$. Lines are best fit curves to second order in $1/L$.

These procedures enable us to calculate the energy cost of binding a flux to an isolated vacancy and conclude that it is energetically favourable to bind fluxes to vacancies in the gapless phase of the Kitaev model. In Figure 4.1(b) we use the same approach to show that the energy cost for adding an isolated flux on a hexagonal plaquette in the clean system is $+0.153J$.

## 4.2 Local moment formation

In this section we investigate the magnetic properties of the Kitaev model in the gapless phase with a single vacancy and a uniform magnetic field. We will see later that in contrast to behaviour in the gapped phase, binding a flux changes greatly the form of the effective moment that forms on the sites adjacent to the vacancy. However, first we begin the investigation with a discussion of the vacancy zero modes in the absence of a flux, since this problem is simpler.

In the gapped phase, knowledge of the vacancy zero modes is sufficient to obtain the magnetic properties of the effective moments that form around each vacancy site. In the gapless phase, however, one must also consider the continuum of states. Despite this, a study of zero modes is useful because it contributes to our general understanding of properties of the gapless phase and the interaction of the effective moments. In section 4.4 we will see that knowledge of these modes also forms an essential part of the discussion of finite size effects.



A vacancy B vacancy

Figure 4.2: Vacancy zero modes found by exact diagonalisation of the tight binding model (2.18) for a single vacancy on the A and B sublattices. We take a lattice a $34 \times 34$ unit cells with PBC.

It remains the case that introduction of a single vacancy on one sublattice causes the matrix $M$ (or $M^T$) to be rank deficient and therefore guarantees at least one zero energy state with amplitude only on the opposite sublattice. However, the form of that zero energy state is qualitatively different in the gapless phase. Using Cartesian coordinates $\mathbf{r} = (x, y)$ , at long distances from a vacancy on the A(B) sublattice located at the origin, the vacancy zero mode $\Psi^{A(B)}(\mathbf{r})$ decays as[74]

$$\Psi^{A(B)}(\mathbf{r}) \propto \frac{1}{x+iy} + \frac{1}{x-iy} \qquad (4.3)$$

B(A) sublattice only, 0 otherwise

and is thus only quasinormalisable, by which we mean that the normalisation is proportional to $1/\sqrt{\log(L)}$ for large system sizes. In Figure 4.2 we plot the vacancy zero mode found by exact diagonalisation of the tight binding model (2.18). Notice that a three fold rotational symmetry of $\Psi^{A(B)}(\mathbf{r})$ is clearly visible.

Ideally we would also like to consider the vacancy zero mode with a flux attached to the vacancy plaquette. However, we do not know how to obtain analytically the zero mode in this, the ground state flux sector. Indeed, the lack of translational symmetry makes if very hard to obtain *any* analytic results in the ground state flux sector. One can gain an understanding of the localisation of the mode by calculating its inverse participation ratio (IPR), though even this task is not trivial. A lattice with a single vacancy with

a flux attached to the vacancy plaquette and no others requires open BC. However, this generates zero energy edge states that obscure the IPR of the zero energy vacancy mode. Instead, one must consider two vacancies on a lattice with PBC, choosing system sizes so that there are no zero energy states in the clean system, and take the limit of large vacancy separation. In detail, we put two vacancies on the same sublattice, on a square lattice with twisted PBC. A clean, square lattice with twisted PBC has no exact zero energy states. Introduction of two vacancies on the same sublattice generates two zero energy modes, $\Psi_0(\mathbf{r})$ and $\Psi_0'(\mathbf{r})$. The remaining $2N-2$ states $\Psi_n(\mathbf{r})$, with $n \neq 0$, are extended and have finite energy $E_n \neq 0$. We define the IPR for the zero energy modes and an average IPR for the non-zero energy states as respectively:

$$\text{IPR} = \sum_{\mathbf{r}} \left( |\Psi_0(\mathbf{r})|^2 + |\Psi_0'(\mathbf{r})|^2 \right)^2 \qquad \langle \text{IPR} \rangle = \sum_{\mathbf{r}} \sum_{E_n \neq 0} \frac{|\Psi_n(\mathbf{r})|^4}{2N-2} \ . \tag{4.4}$$

Extended states have an $\langle \text{IPR} \rangle \sim O(1/N)$, whereas a completely localised state has an IPR $\sim O(1)$. The vacancy zero mode in the flux free sector, Eq. (4.3), has a normalisation $1/\sqrt{\log(N)}$ and therefore has an IPR $\sim 1/\log(N)^2$. In Figure 4.3 our numerics show that the vacancy zero modes in the presence of a flux are less localised and suggest a functional form

$$\text{IPR} \sim \frac{\log(N)^{1/2}}{N} \ , \tag{4.5}$$

though the slowly varying nature of $\log(N)$ makes precision on the exponent difficult. It is hard to make any further quantitative analysis of the vacancy mode. However, we will now show that by using the standard T-matrix formalism introduced in Eq. (3.26), one can find the functional form of the vacancy susceptibility without full knowledge of the vacancy zero modes in the ground state flux sector.

As in the gapped phase, a vacancy breaks three bonds, leaving three Majoranas that do not appear in the Kitaev Hamiltonian (2.5) and which are interpreted as three uncoupled orbitals in the tight binding model (2.18). There are two qualitative differences from the calculation of the vacancy moment in the gapped phase. First, since the bulk excitations are gapless we must use a more general T-matrix approach to describe the action of the perturbing field. Secondly, all three of the zero energy orbitals are coupled to the extended, bulk excitations and also to the zero energy vacancy mode. This means that all three components of the effective moment formed at the vacancy $m_x, m_y$ and $m_z$ may be non-zero.

First, we will discuss the effective vacancy moment formed in the flux free sector, where analytical results can be obtained. This calculation will not only guide us in our attempts to find the vacancy magnetisation in the ground state flux sector but will later be used

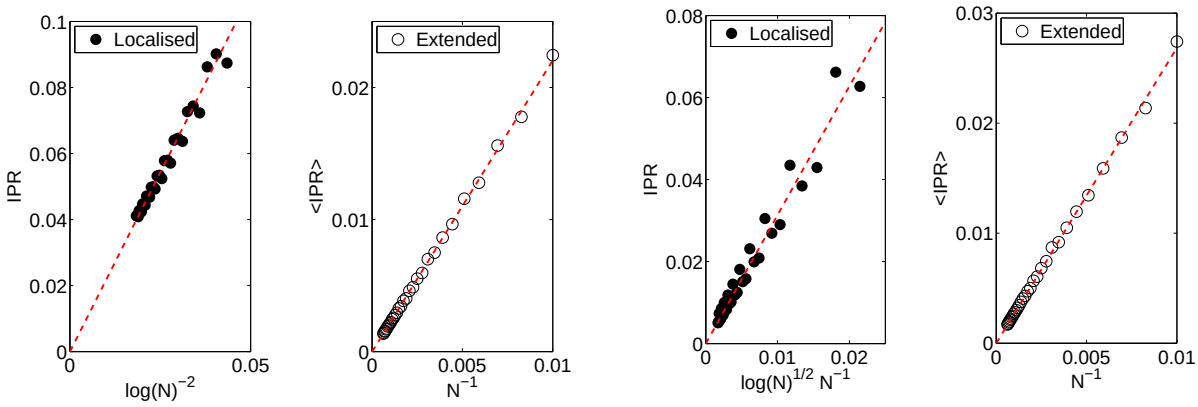



Figure 4.3: a) The IPR for zero energy modes and the average $\langle \text{IPR} \rangle$ for non-zero energy states in the flux free sector versus system size $N$ b) The same quantities but in the ground state flux sector with fluxes attached to vacancy plaquettes. The range of system size in each plot is the same: $10^2 \leq N \leq 40^2$.

to determine the magnetisation of pairs of vacancies on the same sublattice. We will then find the effective moment in the ground state flux sector by a combination of analytical treatment and numerical results. Our approach for the flux free sector is to find the Green function $G(\mathbf{h}, \mathbf{r}, \mathbf{r}')$ for the tight binding model depicted in Figure 3.4(c) as a function of weak field strength $\mathbf{h}$, where the condition on the smallness of the field is $\mathbf{h} \ll \Delta_W$. The gap to flux excitations is $O(J)$ and the condition on the smallness of $\mathbf{h}$ is therefore less strict than in the gapped phase, where $\Delta_W$ is small and goes to zero as $j_x, j_y \to 0$, as shown in Eq. (3.10). As for the gapped phase, one can project onto the ground state flux sector and work perturbatively in $\mathbf{h}$. In the gapless phase, and to leading order, the undiluted system has a finite, field independent magnetic susceptibility.

The Green function $G(\mathbf{h}, \mathbf{r}, \mathbf{r}')$ is a matrix with row and column labels $\mathbf{r}$ and $\mathbf{r}'$ and in the following, Tr is a trace over these labels. Defining $\mathcal{E}(z, h) = z\text{Tr}[G(\mathbf{h}, \mathbf{r}, \mathbf{r}') - G(0, \mathbf{r}, \mathbf{r}')]$, the change in ground state energy as a function of field for the Kitaev model with a vacancy and field, compared to its zero field value is given by an anticlockwise integral around the negative real axis:

$$\mathcal{E}(h) = \frac{1}{2\pi i} \oint \mathcal{E}(z, h) dz. \tag{4.6}$$

For simplicity we present a derivation of $G(\mathbf{h}, \mathbf{r}, \mathbf{r}')$ with a field for which only one component is non-zero; $\mathbf{h} = (0, 0, h)$. To arrive at the Green function for the tight binding model of Figure 3.4(c) we use the standard T-matrix formalism, introduced in Eq. (3.26), with a sequence of two perturbations to cast matrix elements of $G(h, \mathbf{r}, \mathbf{r}')$ in terms of the Green

function for the undiluted hexagonal lattice $G_0(\mathbf{r}, \mathbf{r}')$.

First, we add to the model a potential $1/\epsilon$ at the site $\mathbf{r}_v$ and take the limit $\epsilon \to 0$ to represent the effect of a vacancy. Let there be $2N$ sites in the original lattice. Since $G(0, \mathbf{r}, \mathbf{r}_v) = 0$ for all $\mathbf{r}$, this procedure then generates a $(2N-1) \times (2N-1)$ block in the Green function $G(0, \mathbf{r}, \mathbf{r}')$. We then introduce a new orbital $\mathbf{r}_z$ at zero energy, which will be coupled by the field to $\mathbf{r}_3$. In doing this we have obtained the $2N \times 2N$ Green function $G(0, \mathbf{r}, \mathbf{r}')$ with block diagonal structure

$$G(0, \mathbf{r}, \mathbf{r}') = \begin{cases} G_0(\mathbf{r}, \mathbf{r}') - \dfrac{G_0(\mathbf{r}, \mathbf{r}_v) G_0(\mathbf{r}_v, \mathbf{r}')}{G_0(\mathbf{r}, \mathbf{r})} & \mathbf{r}, \mathbf{r}' \neq \mathbf{r}_v \\ 1/z & \mathbf{r} = \mathbf{r}' = \mathbf{r}_z. \end{cases} \tag{4.7}$$

The sites $\mathbf{r}_x$ and $\mathbf{r}_y$ in Figure 3.4(c) remain uncoupled and do not appear in the tight binding Hamiltonian.

Secondly, we introduce the field that couples sites $\mathbf{r}_z$ and $\mathbf{r}_3$. The T-matrix for this perturbation is therefore $2 \times 2$. Defining the site-diagonal element of $G(0, \mathbf{r}, \mathbf{r}')$ at the site $\mathbf{r}_3$ adjacent to the vacancy as $g(z) \equiv G(0, \mathbf{r}_3, \mathbf{r}_3) = G_0(\mathbf{r}, \mathbf{r}) - G_0(\mathbf{r}_3, \mathbf{r}_v)^2 / G_0(\mathbf{r}, \mathbf{r})$, we find

$$T = \frac{h}{z - g(z)h^2} \begin{pmatrix} g(z)hz & z \\ z & h \end{pmatrix} . \tag{4.8}$$

Let $T(\mathbf{r}', \mathbf{r}'')$ be an element of this matrix, then

$$\begin{aligned} \mathcal{E}(z, h) = & \; z \sum_{\mathbf{r} \neq \mathbf{r}_v} \sum_{\mathbf{r}', \mathbf{r}''} G(0, \mathbf{r}, \mathbf{r}') T(\mathbf{r}', \mathbf{r}'') G(0, \mathbf{r}'', \mathbf{r}) \\ = & \; \frac{h^2 g(z)}{z - g(z)h^2} + \frac{z h^2}{z - g(z)h^2} \sum_{\mathbf{r} \neq \mathbf{r}_v} G(0, \mathbf{r}, \mathbf{r}_3) G(0, \mathbf{r}_3, \mathbf{r}) \; , \end{aligned} \tag{4.9}$$

where the sums on $\mathbf{r}'$ and $\mathbf{r}''$ run over sites $\mathbf{r}_z$ and $\mathbf{r}_3$. Finally, using $\sum_{\mathbf{r} \neq \mathbf{r}_v} G(0, \mathbf{r}, \mathbf{r}_3) G(0, \mathbf{r}_3, \mathbf{r}) = \sum_r G(0, \mathbf{r}, \mathbf{r}_3) G(0, \mathbf{r}_3, \mathbf{r}) = -\partial_z g(z)$,

$$\mathcal{E}(z, h) = \frac{h^2 [g(z) - z \partial_z g(z)]}{z - h^2 g(z)} \; . \tag{4.10}$$

For fields $h \ll J$, the dominant contribution to the integral (4.6) comes from the region of small $z$ and therefore $\mathcal{E}(h)$ is dependent only on the low energy properties of $g(z)$. In Appendix A we show that for small $z$

$$G_0(\mathbf{r}, \mathbf{r}) \sim \lambda z \log \left[ -(\mu z)^2 \right] \tag{4.11}$$

and

$$G_0(\mathbf{r}_3, \mathbf{r}_v) \sim -\nu \; , \tag{4.12}$$

with $\lambda = 1/\sqrt{3}\pi$ and $\mu = \nu = 1/3$ . The $z$-dependences of Eq. (4.11) are a direct consequence of the massless Dirac spectrum for the nearest neighbour tight binding model on the honeycomb lattice, and hold with appropriate values for $\lambda$, $\mu$ and $\nu$ throughout the gapless phase.

Evaluation of the integral (4.6) is outlined in Appendix B.1, where we obtain the asymptotic behaviour of the field dependent energy $\mathcal{E}(h)$ at small $h$. In the following equations $W_{-1}$ is the $-1$ branch of the Lambert W function[20] evaluated with argument $-h^2\mu^2\nu^2/\lambda$:

$$\mathcal{E}(h) \sim \frac{h\sqrt{-W_{-1}}}{(1+W_{-1})}\sqrt{\frac{\nu^2}{\lambda}} \tag{4.13}$$

$$\sim -h\nu[2\lambda \log(1/h)]^{-1/2} \ . \tag{4.14}$$

To leading order, the magnetisation is therefore

$$m(h) = -\partial_h \mathcal{E}(h) \sim \nu[2\lambda \log(1/h)]^{-1/2} \ . \tag{4.15}$$

If the field is in a general orientation, then $G(0, \mathbf{r}, \mathbf{r}')$ has dimension $(2N+2) \times (2N+2)$, since it now includes the sites $\mathbf{r}_x$ and $\mathbf{r}_y$. The T-matrix analogous to (4.8) is now $6 \times 6$ and significantly more complicated. Nevertheless, in Appendix B.3 we describe the steps that allow one to show that the integrand in Eq. (4.6) is dependent only on the magnitude of $\mathbf{h}$ and becomes $\mathcal{E}(z, |\mathbf{h}|)$. As for the gapped phase, the magnetisation is entirely localized on sites adjacent to the vacancy but now each of these sites, labelled $\mathbf{r}_1, \mathbf{r}_2, \mathbf{r}_3$ in Figure 3.4(c), carries a separate component ($m_x, m_y$ and $m_z$, respectively). The magnitude of component $m_\alpha$ can be found by differentiation of $\mathcal{E}(|\mathbf{h}|)$ with respect to $h_\alpha$

$$m_\alpha(\mathbf{h}) = -\partial_{h_\alpha}\mathcal{E}(|\mathbf{h}|) = m(|\mathbf{h}|)\frac{h_\alpha}{|\mathbf{h}|}. \tag{4.16}$$

The relative magnitude of the moment on each site is thus proportional to the corresponding component of $\mathbf{h}$. From Eq. (4.15) we find the vacancy susceptibility diverges in the small $h$ limit:

$$\chi(h) = \partial_h m(h) \sim \frac{1}{h[\log(1/h)]^{3/2}} \ . \tag{4.17}$$

It is also interesting to consider the susceptibility at finite temperatures. If the temperature $T$ is small compared to exchange, thermal fluctuations can be treated as fermion excitations within one flux sector and the magnetisation must be calculated from the free-energy rather than the energy. The partition function $\mathcal{Z}$ can be written as an anticlockwise integral around the negative real axis and the magnetisation is given by

$$\begin{aligned} m(h,T) = &\ T\partial_h \log(\mathcal{Z}) = T\partial_h \sum_m \log\left[2\cosh(S_m/T)\right] \\ = &\ T\partial_h \ \frac{1}{2\pi i}\oint \frac{\mathcal{E}(z,h)}{z}\log\left[2\cosh(z/T)\right] dz. \end{aligned} \tag{4.18}$$

In Appendix B.2 we perform this integral and obtain the following results

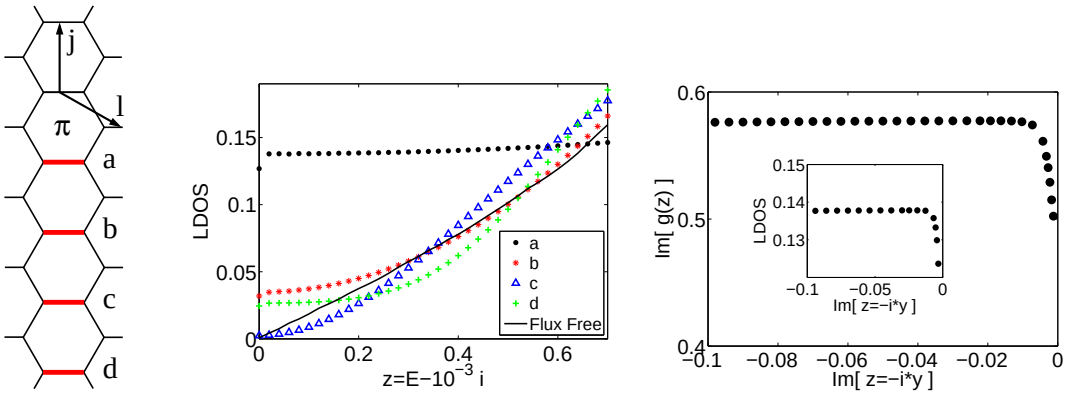
$$m(h,T) \simeq \begin{cases} \dfrac{h\nu^2}{2T\lambda\log(1/\mu T)} & \dfrac{h\nu}{\sqrt{2\lambda\log(1/h)}} \ll T \ll 1 \\ \sqrt{\dfrac{\nu^2}{2\lambda\log[1/h]} - \dfrac{\lambda T^3}{h^3\nu^2}} & T \ll \dfrac{h\nu}{\sqrt{2\lambda\log(1/h)}} \ll 1 \ . \end{cases} \tag{4.19}$$

We can understand these results physically as follows. The vacancy has locally reduced the number of constraints on the three spins adjacent to it and allowed an ultra-local effective moment to form. In the high temperature regime it may be described as *almost* free, by which we mean that it has almost Curie behaviour, but with a Curie 'constant' that varies as $[\log(1/\mu T)]^{-1}$. Contrast this with the effective moment that forms around a vacancy in a two dimensional HAF magnet. Here the moment is spread over a number of spins, as depicted in Figure 1.5, and to leading order is of pure Curie form, as shown in Eq. (1.20). In fact, the high temperature regime for a vacancy in the Kitaev model has the same functional form as the boundary susceptibility of an open ended spin-$\frac{1}{2}$ HAF chain, Eq. (1.7). However, this is almost certainly a coincidence: for example, the $T = 0$ susceptibility of that system, given in Eq. (1.8), is parametrically smaller than that found here.

Having found the magnetisation in the flux free sector we now turn to an analysis of the magnetisation in the ground state flux sector. The above results for the magnetisation are dependent only on the functional form of $g(z)$. To find the magnetisation in the ground state flux sector, with a flux attached to the vacancy plaquette, it is therefore sufficient to determine $g(z)$ in the presence of a flux. We find that the addition of a flux causes an increase in the local density of states (LDOS) around the flux and also removes the singular $z$-dependence of $g(z)$, such that $g(z) \sim$ constant for small $z$. As a consequence the susceptibility is only logarithmically divergent. The numerical method used for the calculation of the LDOS can be found in Appendix D and the results are shown in Figure 4.4(b).

We find $g(z)$ by the following numerical method. In Appendix A we show that the Green function for the infinite, undiluted hexagonal lattice $G_0(\mathbf{0}, \mathbf{r})$ may be found by recursion relations involving elements $G_0(\mathbf{0}, \mathbf{r}')$ closer to the origin, i.e. with $|\mathbf{r}'| \leq |\mathbf{r}|$. One can then use a real space perturbation to find the Green functions in a different flux sector. Explicitly, we find the Green function for a system with a flux at the origin and one at a separation along the x axis $\mathbf{r} = d(\mathbf{n}_1 + \mathbf{n}_2)$ by using a perturbation to the tight binding model (2.18) of

$$\sum_{z-\text{links}} -2J_z u_{jk} \ , \tag{4.20}$$




(a) (b) (c)

Figure 4.4: a) The LDOS is evaluated for the sites 'a-d' indicated on an infinite cylinder, periodic in direction **j**, with circumference 1502 lattice units. The flux string, as indicated by thick, red lines, is also in direction **j**. The second flux is taken half way round the cylinder. The unit vectors **j** and **l** used in calculation of the LDOS in Appendix D are also shown. b) The local density of states. Note that, in particular, the LDOS remains non-zero at site 'a' as $E \to 0$, in the presence of flux. For comparison we include the LDOS for the flux free system. c) $g(z)$ for a system with a flux at the origin and one at $d = 170\hat{\mathbf{x}}$. For $z \lesssim 1/d$ the Green functions that determine $g(z)$ become sensitive to the finite separation of the fluxes. In the limit $d \to \infty$, $g(z) \sim i\zeta$, where $\zeta \simeq 0.58$ is a constant. Inset) The LDOS at site 'a' calculated using this numerical method is in agreement with that calculated using the method in (b).

where the sum runs over $z$-links in the unit cells at $\mathbf{r} = n(\mathbf{n}_1 + \mathbf{n}_2)$ for $0 \leq n \leq d$. This leads to a finite rank T-matrix and a Green function[1] equation $G_F(\mathbf{r}, \mathbf{r}') = G_0(\mathbf{r}, \mathbf{r}') + \sum_{\mathbf{r}'', \mathbf{r}'''} G_0(\mathbf{r}, \mathbf{r}'') T(\mathbf{r}'', \mathbf{r}''') G_0(\mathbf{r}''', \mathbf{r}')$ that can be solved numerically. Convergence of $G_F(\mathbf{r}, \mathbf{r}')$ to that of an isolated vacancy, i.e. the $d \to \infty$ limit, is quickest if we chose $z$ pure imaginary and in Figure 4.4(c) we see that $g(z) \sim i\zeta$, where $\zeta$ is a positive constant.

In Appendix C we perform the integral Eq. (4.6) to calculate the effective vacancy moment in the ground state flux sector that results from this form for $g(z)$. We find

$$m(h,T) \sim \begin{cases} \dfrac{2h\zeta \log(1/T)}{\pi} + O(2h\zeta) & h^2\zeta \ll T \ll 1 \\ \dfrac{2h\zeta \log(1/h^2\zeta)}{\pi} + O\left(\dfrac{-T^2}{h^3}\right) & T \ll h^2\zeta \ll 1 \, . \end{cases} \tag{4.21}$$

Note that the susceptibility diverges at small $T$ and small $h$. Contrast this with the susceptibility of the clean system, which is a constant to leading order. We also point

[1] We remind the reader that the subscript $F$, introduced in section 3.3, denotes that the Green function $G_F(\mathbf{r}, \mathbf{r}')$ relates to a tight binding model with a flux on a plaquette adjacent to the vacancy site, such that when the vacancy is introduced there will be a flux on the vacancy plaquette.

out that the susceptibility in the flux free sector is parametrically larger than that in the ground state flux sector. This fact will be important when calculating the susceptibility of two vacancies on the same sublattice.

## 4.3 Magnetisation of two vacancies

In this section we address the interaction of the effective moments when there are two vacancies present. In the gapped phase, the interaction between vacancy moments sets a field scale. Above this scale the response is the sum of independent vacancy contributions. Below it, the behaviour is dependent on the relative sublattices occupied by the two vacancies. In both regimes the response is qualitatively the same in the flux free sector as in the ground state flux sector, with fluxes attached to vacancies. In the gapless phase this is not the case: as we have seen for a single vacancy, there is a marked difference between behaviour in the ground state and flux free sectors.

In the gapless phase interactions also set a field scale. More precisely, for two vacancies on opposite sublattices, it is the magnitude of the Green function evaluated between the vacancy sites that sets the field scale and also determines the interaction energy between vacancy modes. Vacancies modes on the same sublattice do not interact but we will show that there is still a high and low field regime, with the field scale set by the change of behaviour of the Green function shown in Figure 4.4(c). In both cases, above this scale the effective local moment generated by each vacancy is that of an isolated vacancy $m(h) \sim h\log(1/h)$. Below it, the weak-field response involves low-energy and long-distance features of the system and is controlled by the $Z_2$ sum of the fluxes associated with the vacancies. This $Z_2$ sum is zero. Therefore, remarkably, results for the flux-free sector, expressible in terms of the Green function for the undiluted hexagonal lattice $G_0(\mathbf{r}, \mathbf{r}')$, therefore also illustrate behaviour in the ground state flux sector. In the gapless phase, the magnetic response of the system in these two flux sectors is dramatically different. In particular, we will show that two nearby vacancies on the same sublattice have a *parametrically* larger weak-field susceptibility ($\chi(h) \sim (h[\log(1/h)]^{3/2})^{-1}$) than an isolated vacancy with a bound flux.

In essence there is no further physical insight required to find the susceptibility of two vacancies and we use the same Green function approach as for a single vacancy, leading to the integral Eq. (4.6). We first consider two vacancies on opposite sublattices in a uniform magnetic field.

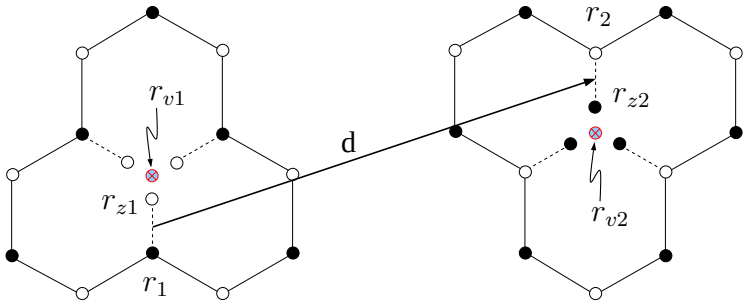



Figure 4.5: Site labelling used in the calculation of the effective moment of two vacancies on opposite sublattices.

### 4.3.1 Two vacancies on opposite sublattices

We introduce a potential $1/\epsilon$ at two sites $\mathbf{r}_{v,1}$ and $\mathbf{r}_{v,2}$, as shown in Figure 4.5, and take the limit $\epsilon \to 0$ to represent the two vacancies. We take a spatially uniform field with only a single non-zero component $\mathbf{h} = (0, 0, h)$ and introduce two zero energy orbitals, that are initially uncoupled from the Hamiltonian but will be coupled with a strength $h$ upon introducing the field. This is exactly analogous to the single vacancy calculation and the first stage leads us to obtain a $2N \times 2N$ Green function $G(h = 0, \mathbf{r}, \mathbf{r}')$ with block diagonal structure

$$\begin{array}{ll} G_0(\mathbf{r}, \mathbf{r}') + (G_0(\mathbf{r}, \mathbf{r}_{v1})\ G_0(\mathbf{r}, \mathbf{r}_{v2}))\, T_v \begin{pmatrix} G_0(\mathbf{r}_{v1}, \mathbf{r}') \\ G_0(\mathbf{r}_{v2}, \mathbf{r}') \end{pmatrix} & \mathbf{r}, \mathbf{r}' \neq \mathbf{r}_{v1} \text{ or } \mathbf{r}_{v2} \\ 1/z & \mathbf{r} = \mathbf{r}' = \mathbf{r}_{z,A} \text{ or } \mathbf{r}_{z,B} \end{array} \tag{4.22}$$

where

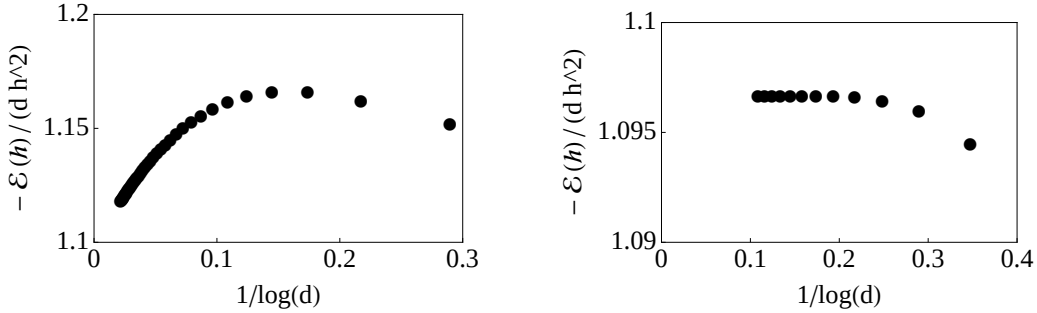
$$T_v = \begin{pmatrix} -G_0(\mathbf{r}, \mathbf{r}) & G_0(\mathbf{r}_{v1}, \mathbf{r}_{v2}) \\ G_0(\mathbf{r}_{v1}, \mathbf{r}_{v2}) & -G_0(\mathbf{r}, \mathbf{r}) \end{pmatrix} \times \frac{1}{G_0(\mathbf{r}, \mathbf{r})^2 - G_0(\mathbf{r}_{v1}, \mathbf{r}_{v2})^2} \tag{4.23}$$

and where in the above equation for $T_v$ we have used that $G_0(\mathbf{r}, \mathbf{r}') = G_0(\mathbf{r}', \mathbf{r})$.

The field couples orbitals $\mathbf{r}_{z,1}$ to $\mathbf{r}_1$, and $\mathbf{r}_{z,2}$ to $\mathbf{r}_2$, and therefore has a T-matrix $T$ that is $4 \times 4$. The integrand of Eq. (4.6) has many terms that may be found by explicit substitution into

$$\mathcal{E}(z, h) = z \sum_{\mathbf{r} \neq \mathbf{r}_{v1}, \mathbf{r}_{v2}} \sum_{\mathbf{r}', \mathbf{r}''} G(0, \mathbf{r}, \mathbf{r}') T(\mathbf{r}', \mathbf{r}'') G(0, \mathbf{r}'', \mathbf{r}) \ , \tag{4.24}$$

where the sums on $\mathbf{r}'$ and $\mathbf{r}''$ now run over sites $\mathbf{r}_{z,1}, \mathbf{r}_1, \mathbf{r}_{z,2}$ and $\mathbf{r}_2$. Using the following




(a) (b)

Figure 4.6: a) The contribution to $\mathcal{E}(h)$ from Eq. (4.29) with $h = 10^{-25}$. Note that $\mathcal{E}(h)/|\mathbf{d}|h^2$ changes by less than 10% as $d$ changes by over 20 orders of magnitude. Changing $h$ by many orders of magnitude leads to changes in $\mathcal{E}(h)/|\mathbf{d}|h^2$ that are not observable at this scale, so long as $hz_1 \ll 1$ is maintained. b) Contribution to $\mathcal{E}(h)$ from the minimum of (4.27). Similarly to (a), changing $h$ by several orders of magnitude produces no observable change in $\mathcal{E}(h)/dh^2$.

identities

$$\begin{aligned} G(0,\mathbf{r}_1,\mathbf{r}_2) &= G(0,\mathbf{r}_2,\mathbf{r}_1) \\ G(0,\mathbf{r}_2,\mathbf{r}_2) &= G(0,\mathbf{r}_1,\mathbf{r}_1) \\ \sum_{\mathbf{r}\neq\mathbf{r}_{v1},\mathbf{r}_{v2}} G(0,\mathbf{r},\mathbf{r}_1)G(0,\mathbf{r}_1,\mathbf{r}) &= -\partial_z G(0,\mathbf{r}_1,\mathbf{r}_1) \\ \sum_{\mathbf{r}\neq\mathbf{r}_{v1},\mathbf{r}_{v2}} G(0,\mathbf{r},\mathbf{r}_1)G(0,\mathbf{r}_2,\mathbf{r}) &= -\partial_z G(0,\mathbf{r}_2,\mathbf{r}_1)\ , \end{aligned} \tag{4.25}$$

we find that $\mathcal{E}(z,h)$ has a numerator

$$\begin{aligned} &2h^2\left\{h^2\left[G(0,\mathbf{r}_2,\mathbf{r}_1)^2 - G(0,\mathbf{r}_1,\mathbf{r}_1)^2\right] + zG(0,\mathbf{r}_1,\mathbf{r}_1)\right\} \\ &-2h^2z\left[z - G(0,\mathbf{r}_1,\mathbf{r}_1)h^2\right]\partial_z G(0,\mathbf{r}_1,\mathbf{r}_1) - 2h^4 zG(0,\mathbf{r}_1,\mathbf{r}_2)\partial_z G(0,\mathbf{r}_1,\mathbf{r}_2) \end{aligned} \tag{4.26}$$

and a denominator

$$[z - h^2G(0,\mathbf{r}_1,\mathbf{r}_1)]^2 - h^4G(0,\mathbf{r}_1,\mathbf{r}_2)^2\ . \tag{4.27}$$

There are two main contributions to the integral Eq. (4.6). The first comes from the energy $z_1$ at which $\mathrm{Abs}[G_0(\mathbf{r},\mathbf{r})^2 - G_0(\mathbf{r}_{v1},\mathbf{r}_{v2})^2]$ is a minimum, the location of which is independent of $h$. Let the separation of the unit cells in which the vacancies are located be $\mathbf{d}$. Using the results of Appendix A we find that

$$z_1 \sim \frac{|G_0(\mathbf{r}_{v1},\mathbf{r}_{v2})|}{\log(1/\,|G_0(\mathbf{r}_{v1},\mathbf{r}_{v2})|)} \propto \frac{|\sin(\mathbf{Q}.\mathbf{d}-\theta)|}{d\log\left[d/|\sin(\mathbf{Q}.\mathbf{d}-\theta)|\right]}\ , \tag{4.28}$$

where $\theta$ is the angle between $\mathbf{d}$ and the x-axis. The high and low field regimes are given by $z_1 \ll h$ and $h \ll z_1$ respectively. Close to $z_1$ the integrand may be approximated by terms

with the lowest powers of $h$ only

$$\mathcal{E}(z,h) \simeq \frac{2h^2 z\left[G(0,\mathbf{r}_1,\mathbf{r}_1) - z\partial_z G(0,\mathbf{r}_1,\mathbf{r}_1)\right]}{z^2} \ . \tag{4.29}$$

The second contribution to $\mathcal{E}(h)$ is from the energy $z_2$ where the denominator (4.27) is a minimum, the location of which is dependent on both $|\mathbf{d}|$ and $h$. We perform the integral over $\mathcal{E}(z,h)$ numerically and find that both of these contributions have the same dependence on $h$ such that

$$\mathcal{E}(h) \sim (c_1 + c_2)h^2 \tag{4.30}$$

The variables $c_1$ and $c_2$ are derived from the integration over the region close to $z_1$ and $z_2$ respectively and are dependent on the vacancy separation $\mathbf{d}$. The numerical integration can be used to find this $\mathbf{d}$ dependence and in Figure 4.6 we show that both $c_1$ and $c_2$ are proportional to $|\mathbf{d}|$ so that $\mathcal{E}(h) \propto |\mathbf{d}|h^2$. Thus, in the flux free sector, the leading order term in the magnetisation for small fields is

$$m(h) \propto |\mathbf{d}|h \ . \tag{4.31}$$

This magnetisation is dependent only on the $z$-dependence of $G(h,\mathbf{r}_1,\mathbf{r}_1)$ and $G(h,\mathbf{r}_1,\mathbf{r}_2)$ evaluated at $h = 0$. Therefore, analogously to the single vacancy calculation, to find the magnetisation in the ground state flux sector it is sufficient to ascertain these two quantities with fluxes bound to a plaquette adjacent to $\mathbf{r}_{v1}$ and $\mathbf{r}_{v2}$. We use the same numerical procedure that allowed us to find the quantity $g(z)$ for the single vacancy calculation in Figure 4.4(b). In Figure 4.7 we show that the functional dependence of $G(0,\mathbf{r}_1,\mathbf{r}_1)$ and $G(0,\mathbf{r}_1,\mathbf{r}_2)$ on the energy $z$ is qualitatively unchanged when the fluxes are included.

The contribution to $\mathcal{E}(h)$ from the integral over Eq. (4.29) is proportional to $h^2$ irrespective of the functional form of $G(0,\mathbf{r}_1,\mathbf{r}_1)$ and $G(0,\mathbf{r}_1,\mathbf{r}_2)$. Furthermore, the results shown in Figure 4.7 mean that the integral around the region $z_2$ also gives a term proportional to $h^2$. Therefore, in the ground state flux sector and for fields $h \ll J$, the leading order term in the effective moment is

$$m(h) \sim (c_1' + c_2')h \ . \tag{4.32}$$

As in the flux free sector, the variables $c_1'$ and $c_2'$ will be dependent on the pair separation $\mathbf{d}$. This dependence may be calculated by knowing the dependence of $G(0,\mathbf{r}_1,\mathbf{r}_1)$ and $G(0,\mathbf{r}_1,\mathbf{r}_2)$ on $|\mathbf{d}|$, both at $z_1$ and at $z_2$. However, we find that the dependence is a complicated function of $\mathbf{d}$, involving powers of logarithms, and we are unable to go to large enough system sizes to give a quantitative analysis of the constants of proportionality in Eq. (4.32). Nevertheless, some qualitative remarks can be made. Although this magnetisation has the same field dependence as for the clean system, the constant of proportionality is an

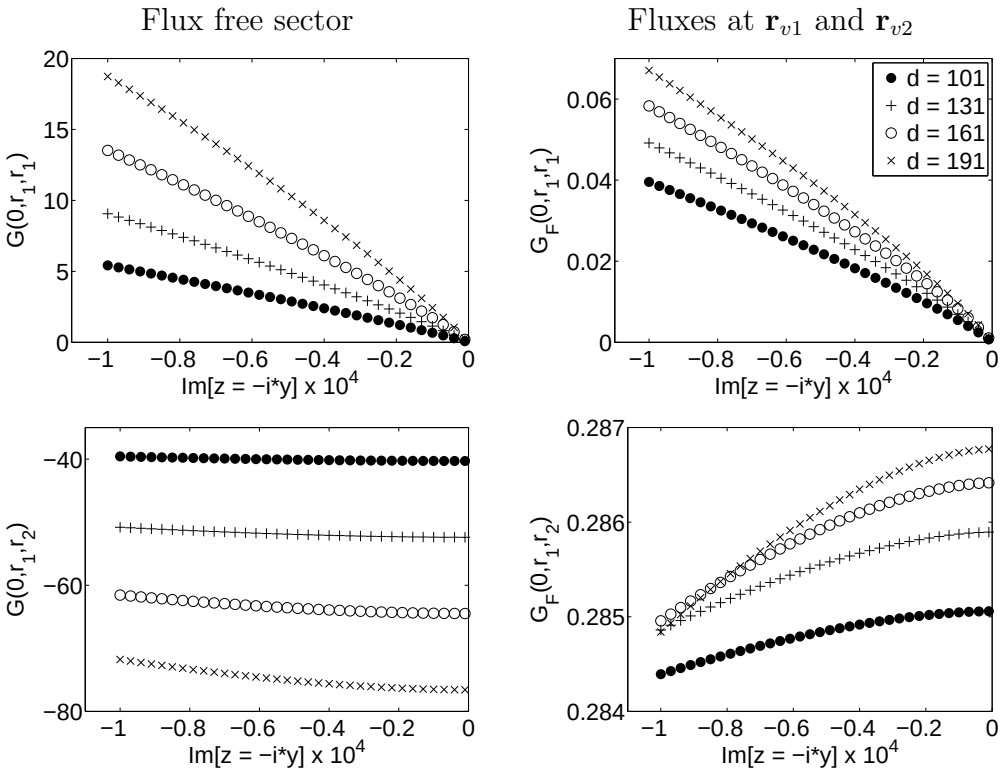



Figure 4.7: The Green function elements $G(0, \mathbf{r}_1, \mathbf{r}_1)$ and $G(0, \mathbf{r}_1, \mathbf{r}_2)$ evaluated in the flux free sector and $G_F(0, \mathbf{r}_1, \mathbf{r}_1)$ and $G_F(0, \mathbf{r}_1, \mathbf{r}_2)$ with fluxes on a plaquette adjacent to $\mathbf{r}_{v1}$ and $\mathbf{r}_{v2}$. Here the vacancies are on opposite sublattices, with a separation $\mathbf{d} = d(\mathbf{n}_1 - \mathbf{n}_2)$. We chose $d$ such that $\sin(\mathbf{Q}.\mathbf{d} - \theta) \neq 0$ and therefore $z_1$ is finite. The energy range plotted is in the regime $z \ll z_1$, where the Green function elements are seen to have qualitatively the same dependence on $z$ in both flux sectors.

increasing function of the pair separation $|\mathbf{d}|$ and means that for well separated vacancies the vacancy susceptibility is *much* larger than the bulk susceptibility per spin, though smaller than that in the flux free sector.

### 4.3.2 Two vacancies on the same sublattice

For two vacancies on the same sublattice, steps can be performed that lead to equations for $T_v$ and $\mathcal{E}(z, h)$ analogous to Eq. (4.23), Eq. (4.26) and Eq. (4.27). Again, we consider two vacancies at positions $r_{v1}$ and $r_{v2}$, as shown in Figure 4.8. Of crucial importance in the evaluation of the magnetisation for two vacancies on opposite sublattices is the Green function element $G_0(\mathbf{r}_{v1}, \mathbf{r}_{v2})$ between the vacancy sites and in particular, that its limiting value as the energy $z \to 0$, is a finite constant. In contrast to this, for two vacancies on the same sublattice, $G_0(\mathbf{r}_{v1}, \mathbf{r}_{v2})$ goes to zero as $z \to 0$. Where necessary for clarity, in what

follows we explicitly include the sublattice label for the vacancy sites. From the results in Appendix A we find that for large $|\mathbf{d}|$

$$\begin{aligned} G_0(\mathbf{r}^A_{v1},\mathbf{r}^B_{v2}) \simeq & \quad \frac{2zi}{\sqrt{3}\pi}K_1\left[\frac{i2|d|z}{\sqrt{3}}\right]\sin\left(\mathbf{Q}.\mathbf{d}-\theta\right) \qquad \sim |\mathbf{d}|^{-1}\sin(\mathbf{Q}.\mathbf{d}-\theta) \\ G_0(\mathbf{r}^A_{v1},\mathbf{r}^A_{v2}) \simeq & -\frac{2z}{\sqrt{3}\pi}K_0\left[\frac{i2|d|z}{\sqrt{3}}\right]\cos(\mathbf{Q}.\mathbf{d}) \qquad \lim_{z\ll d} \qquad \sim z\log\left[i|\mathbf{d}|z\right]\cos(\mathbf{Q}.\mathbf{d})\ . \end{aligned} \tag{4.33}$$

The asymptotic forms on the right hand side of Eq. (4.33) are the leading order approximation to the Green function at small $z$. An example of these results is shown graphically in Figure 4.9. The dependence of $G_0(\mathbf{r}^A_{v1},\mathbf{r}^A_{v2})$ on $z$ implies that the minimum of $G_0(\mathbf{r},\mathbf{r})^2 - G_0(\mathbf{r}^A_{v1},\mathbf{r}^A_{v2})^2$ occurs at $z=0$ and the main contribution to the integral over $\mathcal{E}(z,h)$ comes only from the minimum of the denominator (4.27). Furthermore, it can be shown that the contribution from this point in the integrand has the same form as for the single vacancy calculation

$$\mathcal{E}(h) \propto -h[\log(1/h)]^{-1/2}\ , \tag{4.34}$$

illustrated in Figure 4.10. As advertised earlier in Figure 4.4(c), for two vacancies on the same sublattice the cross over scale, $z_0$, between high and low field regimes is given by the change in behaviour observed in the Green function at small energies. No thorough attempt has been made to quantify the dependence of $z_0$ on $\mathbf{d}$ but a preliminary investigation indicates that approximately $z_0 \sim 1/|\mathbf{d}|$. The results shown in Figure 4.10 indicate that for fields $h \ll z_0$ and to leading order

$$m(h) \propto [\log(1/h)]^{-1/2}\ . \tag{4.35}$$

As for vacancies on opposite sublattices, this result is dependent only on the form of $G(0,\mathbf{r}_1,\mathbf{r}_1)$ and $G(0,\mathbf{r}_1,\mathbf{r}_2)$. In Figure 4.11 we demonstrate numerically that these Green function elements have a dependence on $z$ in the regime $z \ll z_0$ that is qualitatively unaffected by changing the flux sector to one with a fluxes on a plaquette adjacent to $\mathbf{r}_{v1}$ and $\mathbf{r}_{v2}$. Therefore, to leading order, the magnetisation of two nearby vacancies on the same sublattice and in the ground state flux sector is also

$$m(h) \propto [\log(1/h)]^{-1/2}\ . \tag{4.36}$$

This is arguably the most remarkable result of this thesis. In the ground state, two vacancies on the same sublattice have parametrically larger susceptibility than an isolated vacancy. The change in behaviour between high and low field regimes is dependent on the description of states in terms of $Z_2$ flux and matter excitations. The form of the magnetisation is thus not only a test of our assertion that vacancies bind a flux but also of the basic description of the Kitaev model in terms of these variables laid out in chapter 2.

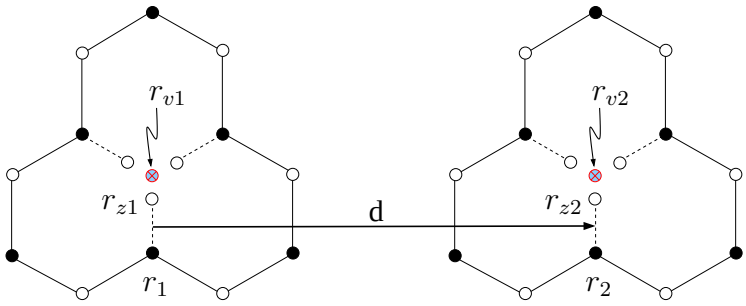



Figure 4.8: Site labelling used in the calculation of the effective moment of two vacancies on the same sublattice.

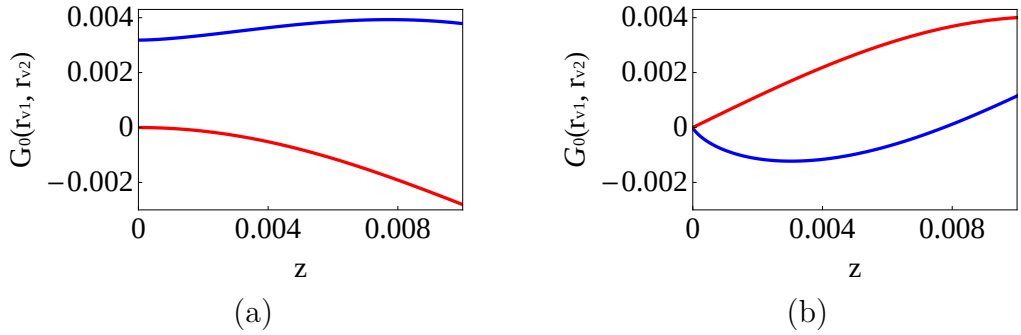



Figure 4.9: The Green function $G_0(\mathbf{r}_{v1}, \mathbf{r}_{v2})$, as given in the left hand side of Eq. (4.33), for two vacancies on a) opposite sublattices and b) the same sublattice. We chose $d = 100$ and for simplicity $\sin(\mathbf{Q}.\mathbf{r} + \theta) = 1$ and $\cos(\mathbf{Q}.\mathbf{r}) = 1$ in each case. Blue and red lines are the real and imaginary parts respectively.

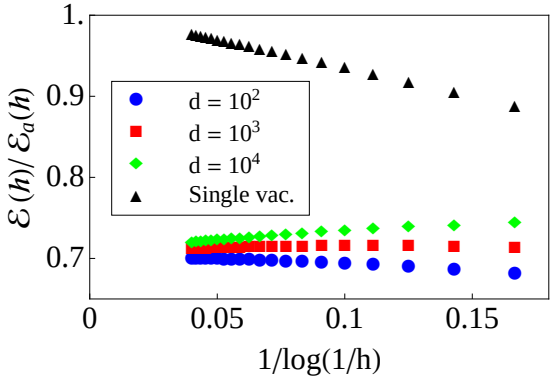



Figure 4.10: Demonstration that $\mathcal{E}(h)$ for two vacancies on the same sublattice and at small fields in the flux free sector has the same functional form as for a single vacancy, also in the flux free sector. The two vacancies have separations $\mathbf{d} = d\hat{\mathbf{x}}$ for $d$ as shown. For comparison, we also plot $\mathcal{E}(h)$ calculated for a single vacancy. In each case $\mathcal{E}(h)$ is calculated by numerical integration of Eq. (4.6) and compared to the asymptotic form for an isolated vacancy $\mathcal{E}_a(h)$ given in Eq. (4.14).

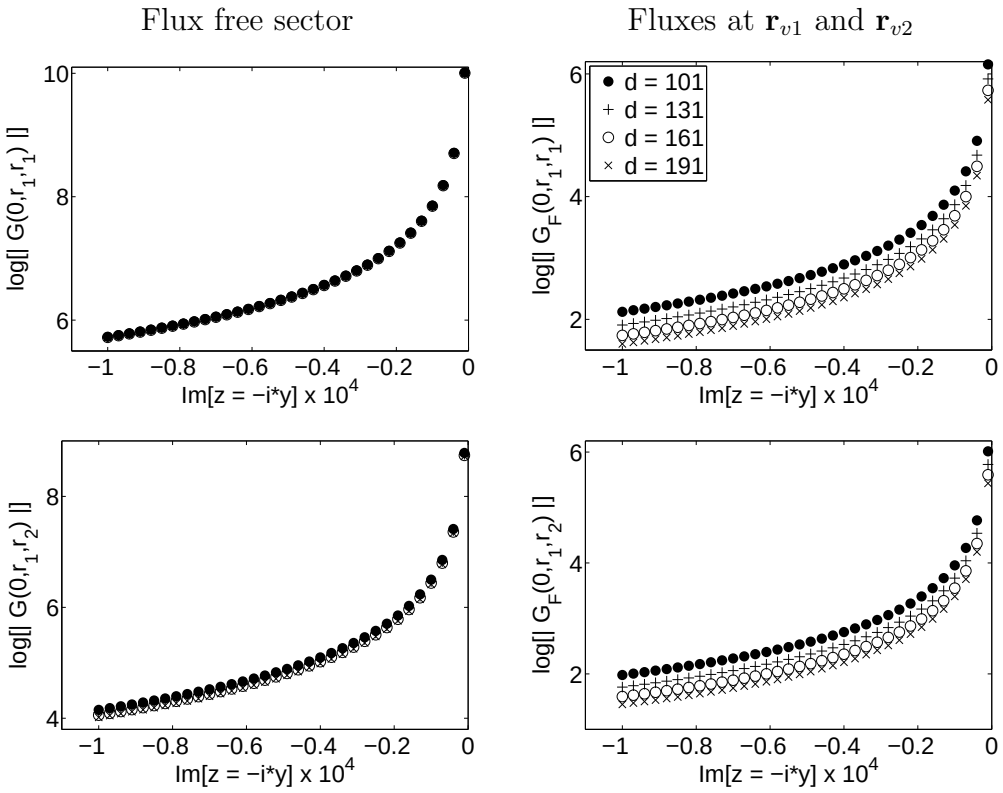



Figure 4.11: The Green function elements $G(0, \mathbf{r}_1, \mathbf{r}_1)$ and $G(0, \mathbf{r}_1, \mathbf{r}_2)$ evaluated in the flux free sector and with fluxes on a plaquette adjacent to $\mathbf{r}_{v1}$ and $\mathbf{r}_{v2}$. Here the vacancies are on the same sublattice, with a separation $\mathbf{d} = d(\mathbf{n}_1 - \mathbf{n}_2)$ and where $d$ is chosen such that $\sin(\mathbf{Q}.\mathbf{d} - \theta) \neq 0$. The elements are therefore evaluated in the regime $z \ll z_0$. The Green function elements have qualitatively the same dependence on $z$ in both flux sectors.

### 4.3.3 Finite density of vacancies

A finite density of vacancies in the gapless phase represents a noteworthy challenge, not least because the density of states is the same as that of disordered graphene, which is a wide and rich field of research[18, 75, 76]. We have not undertaken any work in this area and make only some general observations. The typical vacancy separation will give a length scale and their interactions an energy scale to the problem. For fields large compared to this scale, but still small compared to the gap to other flux sectors, we would expect the impurity susceptibility to be the sum of independent contributions from each vacancy site, which we have evaluated in this chapter. The weak field response we leave as an outstanding, and difficult, problem. Indeed, the density of states is known to diverge at low energies[18, 75, 76] but even the functional form of this divergence is still under debate.

## 4.4 Finite size effects

The above discussion of the magnetic properties of vacancies in the gapless phase has been concerned with a thermodynamically large system. However, an experimental realisation of the Kitaev model using cold atoms may be relatively small and it is pertinent therefore to discuss finite size effects. In fact, we will show that the thermodynamic limit may be approached closely for even a relatively modest sized lattice. First we present an analysis of the flux free system before discussing the ground state flux sector.

In a finite sized system with periodic boundary conditions the spectrum is discrete, with the low energy states having gaps of order $1/L$ between them. First, we consider the case where the tight binding model (2.18) does not have a zero energy state in the undiluted system. Upon introduction of a single vacancy, the quasi localised mode (4.3) is generated at zero energy and the only other zero energy states are the uncoupled orbitals derived from the broken bonds $\mathbf{r}_1, \mathbf{r}_2, \mathbf{r}_3$ in Figure 3.4(c). For fields $|\mathbf{h}| \ll 1/L$ the leading order field dependence of the ground state energy is found by considering the energy change of only these levels and a similar approach to the gapped phase may be followed. The degeneracy is broken, with a level splitting proportional to the applied field. This leads to a paramagnetic moment that is located on the sites adjacent to the vacancy and described by a g-tensor and effective spin Hamiltonian

$$g = \begin{pmatrix} a_0 & 0 & 0 \\ 0 & a_0 & 0 \\ 0 & 0 & a_0 \end{pmatrix}, \qquad H_{\text{eff spin}} = -\tau^\mu g_{\mu\nu} h_\nu \ , \tag{4.37}$$

where now $a_0 \propto [\log(L)]^{-1/2}$ and each component of the magnetisation $m_x, m_y, m_z$ lies on sites $\mathbf{r}_x, \mathbf{r}_y, \mathbf{r}_z$ respectively. The dependence of $a_0$ on $L$ can be demonstrated numerically, as in Figure 4.12(b).

We now consider the case where the finite sized undiluted system with periodic boundary conditions has an exact zero energy state. Eigenvalues of the tight binding model must come in $\pm$ pairs and there are in fact four zero energy states. They are

$$\Psi_0(\mathbf{r}) \sim \frac{1}{L}\left(\mathbb{1} \pm \sigma_z\right) \begin{pmatrix} e^{\pm i\mathbf{Q}\cdot\mathbf{r}} \\ e^{\pm i\mathbf{Q}\cdot\mathbf{r}} \end{pmatrix} \tag{4.38}$$

Upon introduction of the vacancy on one sublattice there remain the two zero energy states above that have magnitude only on the opposite sublattice and of course, the uncoupled orbitals from the broken bonds as above. Applying a field again leads to a level splitting proportional to the field and an effective spin Hamiltonian as in Eq. (4.37). However, now $a_0 \sim 1/L$ as demonstrated in Figure 4.12(a).

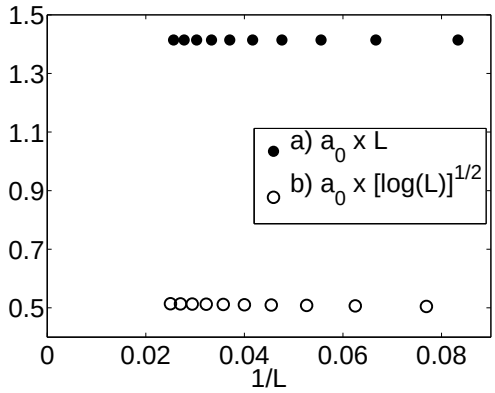



Figure 4.12: a) The effective moment, found numerically using Eq. (3.24) and the limit $\mathbf{h} = (0, 0, h) \to (0, 0, 0^+)$, for a lattice with periodic boundary conditions and system size $L \times L$. The lattice sizes are chosen such that $\mod(L, 3) = 0$ and there is an exact zero energy state in the clean system. b) As for (a) but with $\mod(L, 3) \neq 0$, such that there is no zero energy state in the clean system and the vacancy zero mode is quasi localised.

In Figure 4.3 we demonstrated that the vacancy zero mode in the ground state flux sector was only slightly more localised than a state with equal amplitude on every site: with IPR $\sim \log(N)^{1/2}/N$ compared to IPR $\sim 1/N$ for an extended state. Therefore, in the ground state flux sector, we expect that $a_0 \sim \mathcal{F}(L)/L$, where $\mathcal{F}(L)$ is some slowly varying, logarithmic function of $L$.

The weakest magnetic response of an effective moment found previously was that of two vacancies on opposite sublattices, which had a large, field independent susceptibility, with $m(h) \sim h$.The results of sections 4.2 and 4.3 will hold in the limit that this magnetisation is much larger than any spin jump due to finite size effects. The results of this chapter are thus valid in the regime

$$\frac{\mathcal{F}(L)}{L} \ll h \ll \Delta_W \ . \tag{4.39}$$

## 4.5 Summary

To summarise the information presented on the properties of the Kitaev model with site dilution, in Figure 4.13 we show a schematic plot of the vacancy susceptibility both for one and for two vacancies in the ground state flux sector. The following should also be noted. We have seen that the effective moments formed at each vacancy site interact, by which we mean that the ground state energy is dependent on the relative locations of the two vacancies and the local fields at each vacancy site. However, the Kitaev model with site dilution does not have a spontaneous magnetisation, these effective moments do not

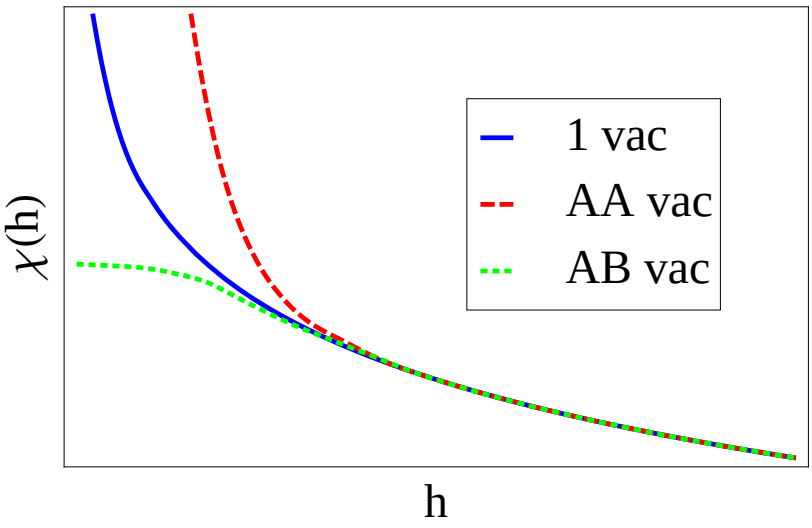



Figure 4.13: A schematic plot of the effective vacancy susceptibility per vacancy in the ground state flux sector for a single vacancy and for two vacancies. For fields large compared to the interaction between vacancy moments, the vacancies behave largely independently and thus have the single vacancy susceptibility $\chi \sim \log(1/h)$, irrespective of the sublattice arrangement. For weak fields, two vacancies on the same sublattice have a susceptibility that diverges parametrically faster than that of a single vacancy $\chi \sim [h(\log(1/h))^{3/2}]^{-1}$ but for two vacancies on opposite sublattices, interactions cut off the divergence $\chi \sim$ large const.

order in zero field and application of a local field at one vacancy site does not induce a magnetisation at another.

The final comment in the above paragraph is somewhat subtle and deserves clarification. Introduction of two vacancies generates a number of zero energy states in the Hamiltonian, two of which are the vacancy zero modes discussed in the text relating to Figure 4.3 and, crucially, the rest are ultra local zero modes associated with breaking bond fermions. Application of a small field causes level splitting, lifts the degeneracy and generates an effective local moment at each vacancy site. As we have seen, the magnitude of these moments is dependent in a complex way on the vacancy sublattices, the field and their separation. Now consider applying a local field at only one vacancy site: i.e. a field of the same form as the projected Zeeman energy in Eq. (3.19). This lifts the degeneracy associated with zero modes at that site and generates an effective moment there. However, the degeneracy associated with the zero modes at the second site remain, there is no level splitting and the magnetisation there is zero.

# Chapter 5

# Disorder in exchange

Discussion has so far been limited to the effects of site dilution on the Kitaev honeycomb model. In the introduction, however, we saw that there are other types of disorder that can have dramatic effects on the physical properties of a system. For example, disorder in the exchange couplings of a spin-$\frac{1}{2}$ Heisenberg antiferromagnetic chain leads to an almost Curie magnetic susceptibility, albeit with a logarithmically temperature dependent Curie 'constant', as shown in Eq. (1.10). In this chapter we investigate the properties of the Kitaev model with quenched disorder in exchange couplings and find that it does not qualitatively affect the magnetic susceptibility but does lead to a change in the heat capacity. We find that the heat capacity has a power law dependence on the temperature with an exponent that depends on the disorder strength.

## 5.1 Slowly varying, weak disorder

We first consider slowly varying, weak disorder in exchange coupling, with the unperturbed exchange $J_\alpha = J$. We define the bond disorder $J_\alpha(\mathbf{r}) = J(1 + \epsilon_\alpha(\mathbf{r}))$, where $\epsilon_\alpha(\mathbf{r})$ is weak $|\epsilon_\alpha(\mathbf{r})| << 1$ and slowly varying on the scale of a lattice spacing $|\epsilon_\alpha(\mathbf{r}) - \epsilon_\alpha(\mathbf{r}+\mathbf{R})| \ll |\epsilon_\alpha(\mathbf{r})|$, where $\mathbf{R}$ is some vector with magnitude of the lattice spacing. Since the disorder is weak, there will remain a finite gap $\Delta_W$ to changing the flux sector out of the ground state. As we have done previously, at field strength $h \ll \Delta_W$ one can project onto the ground state flux sector and work perturbatively in $h$. In this way, one can follow the steps laid out in section (3.2) and conclude that to leading order the magnetic susceptibility is qualitatively unaffected by the slowly varying, weak exchange disorder and to leading order is finite and field independent.

However, as advertised, the disorder will affect the heat capacity. For temperatures $T \ll \Delta_W$, the heat capacity may be found by considering only matter fermion excitations within the ground state flux sector and it is therefore sufficient to know the density of

states of the tight binding model (2.18). An eigenvector $\psi(\mathbf{r}) = (\psi_A(\mathbf{r}), \psi_B(\mathbf{r}))$ of the tight binding model, with energy $E$ satisfies

$$\begin{aligned} E\psi_A(\mathbf{r}) = &\quad J_x(\mathbf{r})\psi_B(\mathbf{r}+\mathbf{n}_1) + J_y(\mathbf{r})\psi_B(\mathbf{r}+\mathbf{n}_2) + J_z(\mathbf{r})\psi_B(\mathbf{r}) \\ E\psi_B(\mathbf{r}) = &\quad J_x(\mathbf{r}-\mathbf{n}_1)\psi_A(\mathbf{r}-\mathbf{n}_1) + J_y(\mathbf{r}-\mathbf{n}_2)\psi_A(\mathbf{r}-\mathbf{n}_2) + J_z(\mathbf{r})\psi_A(\mathbf{r}) \end{aligned} \tag{5.1}$$

The smooth disorder does not contain momentum components that mix the low energy states from the two Dirac cones and we can therefore neglect Umklapp scattering. The low energy states derived from one Dirac cone will be given by the low energy eigenstates of the clean system, modulated by a slowly varying envelope function $\phi_{a(b)}(\mathbf{r})$:

$$\begin{pmatrix} \psi_a(\mathbf{r}) \\ \psi_b(\mathbf{r}) \end{pmatrix} = \begin{pmatrix} e^{i\mathbf{Q}.\mathbf{r}}\phi_a(\mathbf{r}) \\ e^{i\mathbf{Q}.\mathbf{r}}\phi_b(\mathbf{r}) \end{pmatrix}. \tag{5.2}$$

The zero energy states of the unperturbed system are found by setting $\phi_{a(b)} =$ constant. By letting $\mathbf{Q} \to -\mathbf{Q}$ in the following analysis one obtains the low energy states derived from the other Dirac cone. Since $\epsilon_\alpha(\mathbf{r})$ and hence $\phi_{a,b}(\mathbf{r})$ are slowly varying in real space, one can obtain the low energy states by performing a Taylor expansion, keeping only the first order terms:

$$\begin{aligned} E\phi_a(\mathbf{r}) &\simeq J \begin{bmatrix} \frac{1}{2}\left(e^{i\mathbf{Q}.\mathbf{n}_1} - e^{i\mathbf{Q}.\mathbf{n}_2}\right)\partial_x + \frac{\sqrt{3}}{2}\left(e^{i\mathbf{Q}.\mathbf{n}_1} + e^{i\mathbf{Q}.\mathbf{n}_2}\right)\partial_y \\ +\epsilon_x(\mathbf{r})e^{i\mathbf{Q}.\mathbf{n}_1} + \epsilon_y(\mathbf{r})e^{i\mathbf{Q}.\mathbf{n}_2} + \epsilon_z(\mathbf{r}) \end{bmatrix} \phi_b(\mathbf{r}) \\ E\phi_b(\mathbf{r}) &\simeq J \begin{bmatrix} \frac{1}{2}\left(-e^{-i\mathbf{Q}.\mathbf{n}_1} + e^{-i\mathbf{Q}.\mathbf{n}_2}\right)\partial_x - \frac{\sqrt{3}}{2}\left(e^{-i\mathbf{Q}.\mathbf{n}_1} + e^{-i\mathbf{Q}.\mathbf{n}_2}\right)\partial_y \\ +\epsilon_x(\mathbf{r})e^{-i\mathbf{Q}.\mathbf{n}_1} + \epsilon_y(\mathbf{r})e^{-i\mathbf{Q}.\mathbf{n}_2} + \epsilon_z(\mathbf{r}) \end{bmatrix} \phi_b(\mathbf{r}) \end{aligned} \tag{5.3}$$

We make the following definitions of a two component momentum operator $\mathbf{p} = (p_\mu, p_\nu)$ and define a quantity $\mathbf{A}(\mathbf{r}) = (A_\mu(\mathbf{r}), A_\nu(\mathbf{r}))$:

$$\begin{aligned} p_\mu \equiv -i\partial_\mu &= -i\left[\tfrac{-\sqrt{3}}{2}\partial_x\right] & A_\mu(\mathbf{r}) &= \tfrac{1}{2}\left(\epsilon_x(\mathbf{r}) + \epsilon_y(\mathbf{r})\right) - \epsilon_z(\mathbf{r}) \\ p_\nu \equiv -i\partial_\nu &= -i\left[\tfrac{\sqrt{3}}{2}\partial_y\right] & A_\nu(\mathbf{r}) &= \tfrac{\sqrt{3}}{2}\left(\epsilon_x(\mathbf{r}) - \epsilon_y(\mathbf{r})\right) \ . \end{aligned} \tag{5.4}$$

Eq. (5.3) can then be written as

$$E\begin{pmatrix} \phi_a(\mathbf{r}) \\ \phi_b(\mathbf{r}) \end{pmatrix} = J\left(\sigma\cdot\mathbf{p} - \sigma\cdot\mathbf{A}(\mathbf{r})\right)\begin{pmatrix} \phi_a(\mathbf{r}) \\ \phi_b(\mathbf{r}) \end{pmatrix}, \tag{5.5}$$

where $\sigma = (\sigma_x, \sigma_y)$ is a two component vector of Pauli matrices in the standard basis. In this way we have identified the low energy states of the Kitaev model with slowly varying,

weak disorder in exchange couplings with those of a Dirac Hamiltonian with a random vector potential. This Hamiltonian has been studied extensively in Ref. [58].

We chose disorder $\langle \epsilon_\alpha(\mathbf{k})\epsilon_\beta(\mathbf{k}')\rangle = \delta_{\alpha\beta}\delta^2(\mathbf{k}+\mathbf{k}')\Delta_k \frac{8}{9}(2\pi)^2$. The normalisation is not an arbitrary choice but is chosen to coincide with the disorder in Ref. [58]. $\Delta_k$ is a constant for small values of $k$, with small magnitude and a cut off above some characteristic length scale $\xi$ such that $2\pi/\xi << 2\pi/a$, where $a$ is the lattice spacing. These conditions ensure that $\langle \epsilon_\mu(0)\epsilon_\nu(\mathbf{r})\rangle$ is small and decays slowly with $|\mathbf{r}|$.

One can define an effective magnetic field $B$ associated with this vector potential:

$$B = \epsilon_{\mu\nu}\partial_\mu A_\nu = \partial_\mu A_\nu - \partial_\nu A_\mu \tag{5.6}$$

$$B(\mathbf{k}) = \frac{\sqrt{3}}{2} i \left( -\frac{\sqrt{3}}{2}(\epsilon_x(\mathbf{k}) - \epsilon_y(\mathbf{k}))k_x + (-\frac{1}{2}(\epsilon_x(\mathbf{k}) + \epsilon_y(\mathbf{k})) + \epsilon_z(\mathbf{k}))k_y \right) \tag{5.7}$$

$$\begin{aligned}\langle B(\mathbf{k})B(\mathbf{k}')\rangle =& \frac{3}{4}\left( k_x^2 \frac{3}{4}(1+1) + k_y^2(1/4+1/4+1) + k_x k_y \frac{\sqrt{3}}{4}(1-1)\right) \times (2\pi)^2\delta^2(\mathbf{k}+\mathbf{k}')\Delta_k \frac{8}{9} \\ =& (2\pi)^2\delta^2(\mathbf{k}+\mathbf{k}')k^2\Delta_k \end{aligned} \tag{5.8}$$

The density of states of this Dirac system, with these correlations in the magnetic field, is $\rho(E) \propto E^{\frac{2}{z}-1}$, where $z = 1 + \Delta_k/\pi$ [58]. The heat capacity of the Kitaev model is then

$$\begin{aligned} C =& \ \partial_T \int_0^{E_{\max}} E\rho(E)f(E)dE \propto \partial_T \int_0^{E_{\max}} \frac{E^{2/z}}{e^{E/T}+1}dE \\ =& \ T^{2/z}\int_0^{E_{\max}/T} \frac{e^x x^{2/z+1}}{(e^x+1)^2}dx \ . \end{aligned} \tag{5.9}$$

The temperature dependence of the upper limit is unimportant at low $T$. Therefore, randomness in exchange couplings leads to a change in the power law of the heat capacity

$$C \sim T^{2/z} \ , \tag{5.10}$$

where $z \geq 1$, with equality for the unperturbed system.

One can decompose the vector potential into physical and gauge parts $\mathbf{A} = \nabla\wedge U + \nabla V$, which in two dimensions takes the form

$$\begin{aligned} A_\mu(\mathbf{r}) =& \ \ \partial_\nu U(\mathbf{r}) + \partial_\mu V(\mathbf{r}) \\ A_\nu(\mathbf{r}) =& \ -\partial_\mu U(\mathbf{r}) + \partial_\nu V(\mathbf{r}) \ . \end{aligned} \tag{5.11}$$

Written in this way, two zero energy modes may be found

$$\phi \propto (\mathbb{1} + \sigma_z)\begin{pmatrix} e^{\,U-iV} \\ e^{-U-iV} \end{pmatrix} \ . \tag{5.12}$$

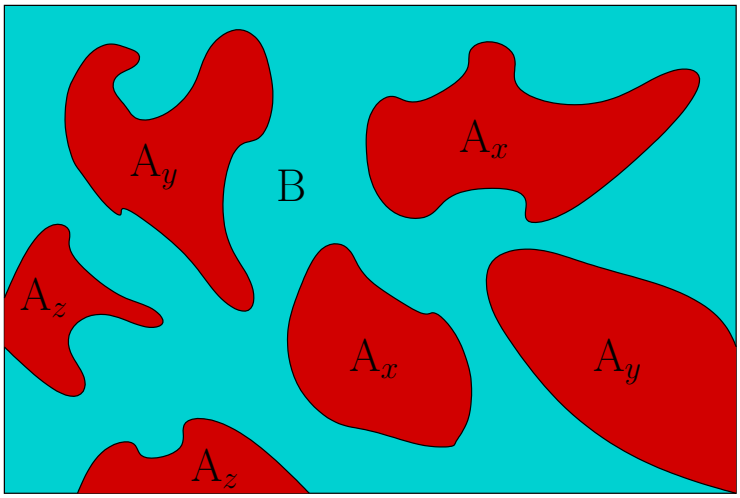



Figure 5.1: Schematic diagram showing some of the effects of slowly varying, strong disorder. Puddles of locally gapped phase are surrounded by a percolating gapless background.

## 5.2 Slowly varying, strong disorder

Slowly varying, strong disorder will cause qualitatively different effects to slowly varying, weak disorder. In particular, the disorder may be strong enough to locally gap the system. In Figure 2.5(a) one can see that there is no parameter space for a continuous transition from one gapped phase to another. In fact, it can be shown that no local perturbation will lead to a finite parameter space for such a transition[52]. Exchange disorder is clearly local and the puddles of gapped phase must therefore be surrounded by a percolating gapless background, as shown schematically in Figure 5.1.

We have seen that the ground state flux sector in both the gapped and gapless phases are flux free. It is therefore reasonable to presume that disorder of this type will not change the flux sector if the disorder does not change the sign of the bonds. The percolating gapless background will have important consequences for energy transport in a system with disorder of this type: there will always be low energy excitations that can move throughout the system but they will presumably be scattered from the gapped puddles, leading to an interesting transport problem.

Note that disorder in the signs of the bonds can be accommodated by changing the flux sector to make the matrix $M$ in Eq. (2.7) identical to that of the flux free sector in the unperturbed system or one of its gauge equivalent copies.

# Chapter 6

# Summary and outlook

## 6.1 Summary

This thesis presents work on disorder in the Kitaev honeycomb model, an exactly solvable quantum spin liquid. To put this work into context we have given first an outline of the effects of disorder in other strongly correlated electron systems. We review spin-$\frac{1}{2}$ and spin-1 Heisenberg antiferromagnetic chains, two dimensional Heisenberg antiferromagnets and provide a brief overview of their relation to the cuprates. In all these cases, site dilution locally reduces the number of constraints on a spin, allowing greater spin fluctuations and an effective moment to form around the vacancy site. The spatial extent of this moment and its magnetic susceptibility are dependent on the properties of the host system, though the effective moment typically has a Curie or almost Curie susceptibility, with latter having a Curie 'constant' that may be a slowly varying function of temperature and magnetic field. We also expand upon some areas of physics that are pertinent to a discussion of the Kitaev model including RVB liquids, VBS and spin liquids, and quantum computation, though there is not scope in this thesis for a full review of the extensive literature on these subjects.

The Kitaev honeycomb model is exactly solvable but it is far from trivial. In chapter 2 we demonstrate the transformation of spin degrees of freedom to Majorana fermions that permits a reduction of the Hamiltonian to a free fermion problem and hence leads to its exact solvability. This transformation necessitates the use of a projection operator to obtain physical states of the system and we describe how one can calculate matrix elements in the projected physical space. Finally, we present some properties of the clean system, show that the model is an algebraic spin liquid, with long-range bond energy correlations and outline two proposals for an experimental realisation of the model.

Chapters 3 and 4 are concerned with site dilution in the Kitaev model, the formation of effective moments in weak magnetic fields and their interactions. The moments have qualitatively different behaviour in the gapped and gapless phases and we have separated

our analysis accordingly. A common feature of both phases, however, is that vacancies bind a flux.

In the gapped phase, an isolated vacancy leads to a localised, effective paramagnetic moment. It is described by an effective Hamiltonian $H_{\text{eff spin}} = -\tau^\mu g_{\mu\nu} h_\nu$, where $\tau^\mu$ is a Pauli matrix and the $g$-tensor has only a single non-zero component, $g_{\alpha\alpha}$, where $\alpha$ is the bond-type of the strong bonds $x, y$ or $z$. Two vacancies on the same sublattice generate moments that do not interact and lead to two paramagnetic moments of the above form. On opposite sublattices, the moments interact with an interaction energy $E$ and are described by an effective Hamiltonian $H_{\text{eff spin}} = E\tau_1^x \tau_2^x - \tau_1^z g_{zz} h_{1,z} - \tau_2^z g_{zz} h_{2,z}$ for the gapped phase with strong $z$ bonds. As for the single vacancy, the effective moments have only a single, non-zero component defined by the strong bonds, z in this case. The other spin components $\tau_j^x$ and $\tau_j^y$ do not have physical meaning and $H_{\text{eff spin}}$ should be used solely as a means to calculate the effective moment in the $z$ direction. A finite density of vacancies leads to interactions between vacancy moments on all length scales and a divergent density of states at low energies. In turn, this leads to a divergent magnetic susceptibility at small fields. This is in contrast to the clean system, where the magnetic susceptibility is a constant.

In the gapless phase behaviour is more subtle but calculations are more difficult. For a clean system the magnetic susceptibility is still a constant, whereas the effective moment that forms around a single vacancy now has a susceptibility $\chi(h) \sim \log(1/h)$. The moments formed around vacancies on opposite sublattices interact and to leading order lead to a large, field independent vacancy susceptibility. Two vacancy moments on the same sublattice interact in a complex way and in the limit of small $h$ have a combined susceptibility $\chi(h) \sim [h(\log(1/h))^{3/2}]^{-1}$ that is parametrically larger than that of an isolated vacancy.

In chapter 5 we look at another type of disorder: slowly varying quanched disorder in exchange coupling. We find that the low energy degrees of freedom of the Kitaev model with this disorder are described by a Dirac Hamiltonian with a random vector potential. This has a heat capacity $C \sim T^{2/z}$, where $z$ is a measure of the disorder and increases from one with increasing disorder strength.

## 6.2 Outlook

In the final section of this thesis we outline some outstanding questions pertaining to the results we have obtained, indicate some systems that are natural extensions of the Kitaev honeycomb model and suggest some areas of interesting future work.

One open question concerns the Green function for the hexagonal lattice with a single flux, studied numerically in Appendix D. This is done by solving the defining Green

function equation on two half infinite cylinders and matching at the boundary, where we include the flux string. It is only in this last step that we resort to a numerical analysis to solve the following coupled integral equations

$$\begin{aligned} \Lambda^{+}(z,\mathbf{q})G^{AA}_{F,R}(\mathbf{q},0) - \int \tilde{h}(\mathbf{k}-\mathbf{q})\widetilde{G}^{BA}_{F,L}(\mathbf{k},0)\frac{dk}{2\pi} &= 1 \\ \frac{1}{\Lambda^{-}(z,\mathbf{q})}G^{BA}_{F,L}(\mathbf{q},0) - \int \tilde{h}(\mathbf{k}-\mathbf{q})\widetilde{G}^{AA}_{F,R}(\mathbf{k},0)\frac{dk}{2\pi} &= 0 \ , \end{aligned} \tag{6.1}$$

where a tilde in this case denotes a function in the reciprocal space, and

$$\Lambda^{\pm}(z,\mathbf{q}) = \frac{2z}{-1+z^2-2\cos(\mathbf{q}) \pm \sqrt{3-6z^2+z^4-4(z^2-1)\cos(\mathbf{q})+2\cos(2\mathbf{q})}} \ , \tag{6.2}$$

and

$$\tilde{\eta}(\mathbf{k}-\mathbf{q}) = \sum_j e^{i(\mathbf{k}-\mathbf{q})j}\eta(j) \ . \tag{6.3}$$

These equations can be derived from the defining Green function equations at the boundary. An analytic solution would enable an exact description of the zero energy state for a vacancy in the ground state flux sector and also would allow us to find analytically the effective moment that forms around the vacancy. However, despite much effort, the analytic solution to these equations has eluded us so far.

A second open direction concerns the formulation of a continuum description of the Kitev model with vacancies. In chapter 5 we used a low energy, effective description of the tight binding model to find the eigenvalues and density of states of the Kitaev model. This allowed us to determine the low temperature heat capacity as a function of the disorder strength in exchange couplings. In chapter 4 we used instead the Green function and standard T-matrix formalism to determine the weak field and hence low energy properties of the Kitaev model in a magnetic field. We have been unable to obtain a low energy, effective description for the Kitaev model with vacancies and a field, though one approach may be the following. At points away from the vacancies the low energy properties of the tight binding model are still locally described by a Dirac equation. It should be possible therefore to obtain a low energy, effective theory for the Kitaev model with vacancies and a small magnetic field: the vacancies and field would be encoded in the Dirac Hamiltonian as appropriate boundary conditions at the vacancy sites. The flux and flux string of a single vacancy in the ground state flux sector can be described by a Dirac equation in circular polar coordinates, with antiperiodic boundary conditions on the azimuthal part of the wavefunction. Of course, treating more than a single vacancy in this way will be very difficult. A further difficulty is the that the potential $1/\epsilon$ that we use to represent a

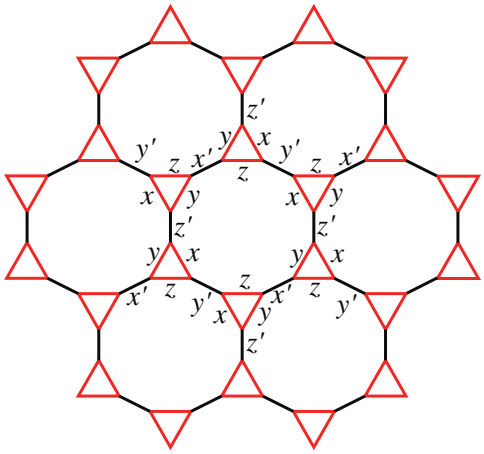



Figure 6.1: The triangular honeycomb lattice as displayed in Ref. [92]. There are six types of bonds $x, y, z$ and $x', y', z'$ and triangular and dodecagonal plaquettes.

vacancy in the tight binding model contains is a sum over all momentum components. It therefore has non-zero matrix elements between states with different valley indices and an effective Hamiltonian would most likely act on a four component wavefunction with both valley and sublattice indices. At present we are unable to find the correct encoding for the magnetic field and vacancy in the boundary conditions.

Finally, we look at some extensions of the Kitaev model to other lattices. The triangular honeycomb lattice, Figure 6.1, is perhaps the most interesting extension that maintains the three-fold coordination of the honeycomb lattice[92]. The Kitaev Hamiltonian for this lattice is

$$\begin{aligned}\widetilde{H} = \; & -J_x \sum_{\text{x-links}} \tilde{\sigma}^x_j \tilde{\sigma}^x_k - J_y \sum_{\text{y-links}} \tilde{\sigma}^y_j \tilde{\sigma}^y_k - J_z \sum_{\text{z-links}} \tilde{\sigma}^z_j \tilde{\sigma}^z_k \\ & -J'_x \sum_{\text{x'-links}} \tilde{\sigma}^x_j \tilde{\sigma}^x_k - J'_y \sum_{\text{y'-links}} \tilde{\sigma}^y_j \tilde{\sigma}^y_k - J'_z \sum_{\text{z'-links}} \tilde{\sigma}^z_j \tilde{\sigma}^z_k \,,\end{aligned} \tag{6.4}$$

and is exactly solvable by the methods laid out in chapter 2. It has both triangular and dodecagonal plaquettes and the flux through each plaquette is defined in the same way as for the Kitaev honeycomb model. Also in parallel with the Kitaev model, these fluxes are non-dynamical. Since the flux through a triangular plaquette is a product of an odd number of spins, ground states of this Hamiltonian explicitly break time reversal symmetry but, like the honeycomb model, break neither spin rotational nor translational symmetry. The ground states are therefore termed chiral spin liquids and can be found exactly.

The phase diagram has both gapped and gapless phases of matter fermion excitations, dependent on the parameters $J_\alpha$ and $J'_\alpha$. If there is a finite energy gap out of the ground state flux sector then the analysis laid out in this thesis will be directly applicable to

this model. The effective moment generated by a vacancy will then be dependent on the specifics of the vacancy zero modes and the matter fermion spectrum.

Of crucial importance to the underlying solvability of the Kitaev model on both the honeycomb and triangular honeycomb lattices is that the coordination of the lattice is equal to the number of elements in the spin-$\frac{1}{2}$ representation of the SU(2) Lie algebra: i.e. three. However, one can obtain an exactly solvable spin Hamiltonian of Kitaev type on more highly connected lattices by using larger spins that have a representation in terms of a Clifford algebra with more elements[90, 93]. For example, using a $4 \times 4$ Gamma matrix representation of a spin-$\frac{3}{2}$ degree of freedom, one can construct exactly solvable spin models on the square[93] and decorated square[90] lattices. As for the Kitaev honeycomb model, an extensive number of commuting flux operators are found that permit a reduction to a free fermion Hamiltonian. Unfortunately, the Hamiltonian on the square lattice constructed in terms of Gamma matrices in this way is somewhat complicated and cumbersome when written in terms of spin-$\frac{3}{2}$ operators and at present it is difficult to envisage a physical system that could be described by such a Hamiltonian. On the decorated square lattice, the Hamiltonian is written in terms of spin-quadrupole operators for the spin-$\frac{3}{2}$ degrees of freedom.

Application of a magnetic field will generate Zeeman terms in the Hamiltonian. However, since the spin models on these more highly connected lattices are now a complicated expression of spin and spin-quadrupole operators, an analysis of the magnetic response will require a new method and the vacancy susceptibility will likely bear little resemblance to the discussion in chapters 3 and 4.

# Appendix A

# Green function for the hexagonal lattice

## A.1 Gapless phase

This section gives details on how to find the Green function of the hexagonal lattice with uniform hopping $J_\alpha = 1$. Transforming the tight binding model, Eq. (2.18), to momentum space, the Hamiltonian and corresponding Green function are

$$\begin{aligned} H(\mathbf{q}) &= \begin{pmatrix} 0 & f_{\mathbf{q}} \\ f_{\mathbf{q}}^* & 0 \end{pmatrix} \\ G_0(\mathbf{q}) &= (z - H(\mathbf{q}))^{-1} = \frac{1}{z^2 - f_{\mathbf{q}} f_{\mathbf{q}}^*} \begin{pmatrix} z & f_{\mathbf{q}} \\ f_{\mathbf{q}}^* & z \end{pmatrix} \end{aligned} \tag{A.1}$$

where $f_{\mathbf{q}} = (1 + e^{iq_1} + e^{iq_2})$, and $q_1 = \mathbf{q}.\mathbf{n}_1$, $q_2 = \mathbf{q}.\mathbf{n}_2$. The real space Green function is

$$G_0^{\alpha\beta}(\mathbf{r}) = \int G_0^{\alpha\beta}(\mathbf{q}) e^{-i\mathbf{q}.\mathbf{r}} \frac{d^2\mathbf{q}}{4\pi^2} \ . \tag{A.2}$$

If $z$ is real and outside of the band then $G_0^{\alpha\beta}(\mathbf{r})$ can be evaluated directly for certain matrix elements and analytically continued to the whole of the complex plane[47]. Using complex energy $z = E - i\epsilon$, with $E$ real and $\epsilon$ a positive infinitesimal, we define

$$A = \frac{2}{\sqrt{(z-1)^3(z+3)}} \quad B = \sqrt{\frac{16z}{(z-1)^3(z+3)}} \qquad C = \frac{2}{1-z} \ , \tag{A.3}$$

where we take the positive square root in each case. In chapter 4 we have used the Green function evaluated at sites along the x axis. For this we will need the following three Green

function elements, valid for $E > 1$ [47]

$$\begin{aligned} G_0^{AA}(\mathbf{0}) = & \frac{zAK(B^2)}{\pi} \\ G_0^{AA}(\mathbf{n}_1+\mathbf{n}_2) = & \frac{zA}{\pi}\left[\frac{(z-3)(z+1)}{2}\Pi(B^2,C^2)+\frac{(z-1)^2}{2}K(B^2)\right] \\ G_0^{AA}(2\mathbf{n}_1+2\mathbf{n}_2) = & \frac{zA}{\pi}\left[\frac{(z-1)^2}{4}K(B^2)+\frac{4(C^2-1)}{(B^2-C^2)C^2}E(B^2)+\right. \\ & \left.\frac{4(C^2-1)(A^2-2C^2+C^4)}{(B^2-C^2)C^4}\Pi(B^2,C^2)\right] , \end{aligned} \tag{A.4}$$

where $K(B^2)$, $E(B^2)$ and $\Pi(B^2,C^2)$ are the complete elliptic integral of the first, second and third kind respectively:

$$\begin{aligned} K(B^2) = & \int_0^{\pi/2}\frac{1}{(1-B^2\sin^2\theta)^{1/2}}d\theta \\ E(B^2) = & \int_0^{\pi/2}(1-B^2\sin^2\theta)^{1/2}d\theta \\ \Pi(B^2,C^2) = & \int_0^{\pi/2}\frac{1}{(1-C^2\sin^2\theta)(1-B^2\sin^2\theta)^{1/2}}d\theta \ . \end{aligned} \tag{A.5}$$

The symmetry of the lattice and defining equations of the Green function allow one to show that

$$G_0^{AA}(\mathbf{n}_1+\mathbf{n}_2) = \frac{-z}{6}(1-zG_0^{AA}(0)) - \frac{G_0^{AA}(0)}{2} \tag{A.6}$$

and hence find a relationship between the first and third complete elliptic integrals

$$\Pi(B^2,C^2) = \frac{2}{(z-3)(z+1)}\left[\frac{-\pi}{6}+K(B^2)\left(\frac{z^2A}{6}-2+z-\frac{z^2}{2}\right)\right] . \tag{A.7}$$

The following recursion relations can be used to find $G_0^{AA}(n(\mathbf{n}_1+\mathbf{n}_2))$ at an arbitrary $A$ site along the x axis [47]

$$\begin{aligned} G_0^{AA}((n+2)(\mathbf{n}_1+\mathbf{n}_2)) = & \frac{1}{n+1}\left[(n+1)(4z^2-1)G_0^{AA}((n+1)(\mathbf{n}_1+\mathbf{n}_2))\right. \\ & -n\left((4z^2-3)^2-3\right)G_0^{AA}(n(\mathbf{n}_1+\mathbf{n}_2)) \\ & +(n+1)(4z^2-1)G_0^{AA}((n-1)(\mathbf{n}_1+\mathbf{n}_2)) \\ & \left.-(n-1)G_0^{AA}((n-2)(\mathbf{n}_1+\mathbf{n}_2))\right] \end{aligned} \tag{A.8}$$

and at an arbitrary $A$ site along the line $\mathbf{r} = n(\mathbf{n}_1+\mathbf{n}_2)+\mathbf{n}_1$

$$\begin{aligned} G_0^{AA}(n(\mathbf{n}_1+\mathbf{n}_2)+\mathbf{n}_1) = & \tfrac{1}{2}(z^2-3)G_0^{AA}(n(\mathbf{n}_1+\mathbf{n}_2)) - G_0^{AA}((n-1)(\mathbf{n}_1+\mathbf{n}_2)+\mathbf{n}_1) \\ & -\tfrac{1}{2}\left[G_0^{AA}((n+1)(\mathbf{n}_1+\mathbf{n}_2))+G_0^{AA}((n-1)(\mathbf{n}_1+\mathbf{n}_2))\right] . \end{aligned} \tag{A.9}$$

The defining Green function equations can then be used to determine the Green function at an arbitrary $B$ site along the x axis:

$$\begin{aligned} zG_0^{BA}(\mathbf{r}+\mathbf{n}_1) - G_0^{AA}(\mathbf{r}) - G_0^{AA}(\mathbf{r}-\mathbf{n}_1) - G_0^{AA}(\mathbf{r}-\mathbf{n}_2) = 0 \\ zG^{AA}(\mathbf{r}) - G^{BA}(\mathbf{r}+\mathbf{n}_1) - G^{BA}(\mathbf{r}+\mathbf{n}_2) - G^{BA}(\mathbf{r},z) = \delta_{\mathbf{r},0} \ . \end{aligned} \tag{A.10}$$

In fact, matrix elements at an arbitrary site $G_0^{\alpha,\beta}(\mathbf{r})$ may be found by recursion relations involving those closer to the origin, i.e. $G_0^{\alpha,\beta}(\mathbf{r}')$ with $\mathbf{r}' \leq \mathbf{r}$.

For $E < 1$ and $z$ just below the real axis, the analytic continuation of the Green function involves a number of steps. One must take the negative square root for $A$ in Eq. (A.3) but keep the positive square root of $B$ and $C$. Define $K'(B^2)$ and $E'(B^2)$ respectively as the complete elliptic integrals given in Eq. (A.5) but with the complementary modulus of $B^2$, i.e. $K'(B^2) = K(1-B^2)$ and $E'(B^2) = E(1-B^2)$. The complete elliptic integrals in Eq. (A.5) must be then analytically continued in the following way

$$\begin{aligned} K(B^2) \rightarrow \ & K(B^2) - 2iK'(B^2) \\ E(B^2) \rightarrow \ & E(B^2) - 2i\left[K'(B^2) - E'(B^2)\right] \ . \end{aligned} \tag{A.11}$$

In the text we require the asymptotic form for $G_0^{AA}(0)$ and $G_0^{BA}(0)$ as $E \rightarrow 0$:

$$G_0^{AA}(0) \sim \frac{z(i\pi + 2\ln(z/3))}{\sqrt{3}\pi} \qquad G_0^{BA}(0) \sim \frac{1}{3}\left(\frac{z^2(i\pi + 2\ln(z/3))}{\sqrt{3}\pi} - 1\right) \tag{A.12}$$

These asymptotic forms are compared to the exact results in Figure A.1(a).

For large $|\mathbf{r}|$ and small $z$ one can find the asymptotic behaviour of $G_0^{AA}(\mathbf{r})$ and $G_0^{BA}(\mathbf{r})$ in the following way. Define the momentum at one of the Dirac nodes as $\mathbf{Q} = (\frac{2\pi}{3}, -\frac{2\pi}{3})$. For $z \ll 1$ and $\mathbf{r} \gg 1$, the dominant contribution to the integral (A.2) is from the region around $\mathbf{Q}$ and the spectrum $|f_{\mathbf{q}}|$ can be approximated as linear in this limit. Let $\mathbf{q} = \pm\mathbf{Q} + \mathbf{p}$, then

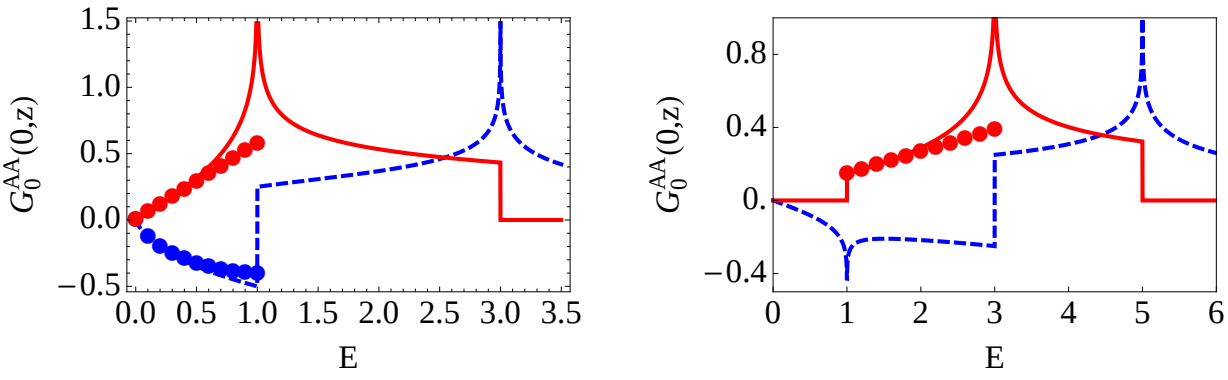
$$\begin{aligned} G_0^{AB}(\mathbf{r}) \simeq & \frac{\sqrt{3}}{2}\int\left(\frac{-(\mathbf{p}_x + i\mathbf{p}_y)e^{i(-\mathbf{Q}.\mathbf{r}-\mathbf{p}.\mathbf{r})}}{z^2 - \frac{3}{4}\mathbf{p}^2} + \frac{(\mathbf{p}_x - i\mathbf{p}_y)e^{i(\mathbf{Q}.\mathbf{r}-\mathbf{p}.\mathbf{r})}}{z^2 - \frac{3}{4}\mathbf{p}^2}\right)\frac{\sqrt{3}}{2}\frac{d^2p}{4\pi^2} \\ = & -\frac{3i}{2}\int\frac{\mathrm{Im}\left[(\mathbf{p}_x + i\mathbf{p}_y)e^{-i\mathbf{Q}.\mathbf{r}}\right]}{z^2 - \frac{3}{4}\mathbf{p}^2}e^{-i\mathbf{p}.\mathbf{r}}\frac{d^2p}{4\pi^2} \\ = & \frac{2zi}{\sqrt{3}\pi}K_1[\frac{i2rz}{\sqrt{3}}]\sin(\mathbf{Q}.\mathbf{r} - \theta) \end{aligned} \tag{A.13}$$

where $\theta$ is the angle between $\mathbf{r}$ and the x axis and $K_1$ is first order modified Bessel function of the second kind. Similarly, it can be shown that

$$G_0^{BA}(\mathbf{r}) \simeq \frac{2zi}{\sqrt{3}\pi}K_1[\frac{i2rz}{\sqrt{3}}]\sin(\mathbf{Q}.\mathbf{r} + \theta) \tag{A.14}$$

$$G_0^{AA}(\mathbf{r}) \simeq -\frac{2z}{\sqrt{3}\pi}K_0[\frac{i2rz}{\sqrt{3}}]\cos(\mathbf{Q}.\mathbf{r}) \ , \tag{A.15}$$

where $K_0$ is the zeroth order modified Bessel function of the second kind.




(a) (b)

Figure A.1: a) Red solid line - $\mathrm{Im}[G_0^{AA}(0)]$; blue dashed line - $\mathrm{Im}[G_0^{AA}(0)]$, dots - asymptotic approximation at small z. Plots were obtained using Mathematica and with $z = E - 10^{-8}i$. b) Solid lines as in (a) but in the gapped phase with $J_x = J_y = 1$ and $J_z = 3$. Dots are the asymptotic approximation to the imaginary part when $E \geq \Delta$.

## A.2 Gapped phase

The Green function in the gapped phase and for arbitrary $z$ not on the real axis can be calculated in a similar manner, although the variables $A, B$ and $C$ depend on all three parameters $J_x, J_y$ and $J_z$. In section 3.4.1 we require the density of states for low energy states in the gapped phase. This can be found by considering the site diagonal Green function $G_0^{AA}(0)$. In the gapped phase we obtain

$$A = \frac{2}{\sqrt{(J_x + J_y - J_z - z)(J_x - J_y + J_z - z)(J_x - J_y - J_z + z)(J_x + J_y + J_z + z)}}$$

$$B = \sqrt{\frac{16 J_x J_y J_z z}{(J_x + J_y - J_z - z)(J_x - J_y + J_z - z)(J_x - J_y - J_z + z)(J_x + J_y + J_z + z)}}$$

$$G_0^{AA}(0,z) = \begin{cases} \dfrac{zAK}{\pi} & E > J_z \\ -\dfrac{zAK}{\pi} & J_z > E \end{cases} \tag{A.16}$$

Evaluating the Green function at complex energy $z = E - i\epsilon$, the density of states is given by $\rho(E) = \lim_{\epsilon \to 0} \frac{1}{\pi} \mathrm{Im}\left[G_0^{AA}(0)\right]$. For low lying degrees of freedom, with energy close to

the band edge $\Delta = J_z - J_x - J_y$, the density of states is approximately

$$\rho(E) \simeq \begin{cases} \dfrac{-\Delta\left[E(4\log[2] - \pi(J_z-1)) + \pi(J_z-1)(J_z(9+J_z^2-6J_z)-2)\right]}{16\pi(J_z-1)(\Delta J_z)^{3/2}} & E > \Delta \\ 0 & \Delta > E \end{cases} . \tag{A.17}$$

In Figure A.1(b) we plot the Green function $G_0^{AA}(0)$ and the approximation used to obtain Eq. (A.17).

The Green function for the gapped phase at real energies $z$ small compared to the gap can be found by a perturbative expansion in $j_x$ and $j_y$. Let $\mathbf{r} = n_1\mathbf{n}_1 + n_2\mathbf{n}_2$ and $f_{\mathbf{q}} = (J_z + J_x e^{iq_1} + J_y e^{iq_2})$

$$\begin{aligned} G_0^{AB}(\mathbf{r}) &= \int \frac{f_{\mathbf{q}}}{z^2 - |f_{\mathbf{q}}|^2} e^{-i\mathbf{q}.\mathbf{r}} \frac{d^2\mathbf{q}}{4\pi^2} \\ &\simeq -\int \frac{1}{f_{\mathbf{q}}^*} e^{-i\mathbf{q}.\mathbf{r}} \frac{d^2\mathbf{q}}{4\pi^2} = -\int J_z^{-1}\left(1 + j_x e^{-iq_1} + j_y e^{-iq_2}\right)^{-1} e^{-i\mathbf{q}.\mathbf{r}} \frac{d^2q}{4\pi^2} \\ &= (-1)^{|n_1|+|n_2|+1} J_z^{-1}\ j_x^{|n_1|}\ j_y^{|n_2|} \binom{|n_1|+|n_2|}{|n_1|} \qquad n_1, n_2 \le 0,\ 0 \text{ otherwise} \end{aligned} \tag{A.18}$$

$$G_0^{BA}(\mathbf{r}) \simeq (-1)^{n_1+n_2+1} J_z^{-1}\ j_x^{n_1}\ j_y^{n_2} \binom{n_1+n_2}{n_1} \qquad n_1, n_2 \ge 0,\ 0 \text{ otherwise.} \tag{A.19}$$

The Green function evaluated between sites on the same sublattice can be found in an analogous manner. We find

$$\begin{aligned} G_0^{AA}(\mathbf{r}) \simeq (-1)^{|n_1|+|n_2|+1} \frac{z}{J_z^2}\ j_x^{|n_1|}\ j_y^{|n_2|} \times \left[\sum_{k_1,k_2=0}^{\infty} \binom{|n_1|+|n_2|+k_1+k_2}{|n_1|+k_1} \binom{k_1+k_2}{k_1}\ j_x^{2k_1}\ j_y^{2k_2}\right] \\ \text{for } \mathrm{sgn}(n_1) = \mathrm{sgn}(n_2) \end{aligned}$$

$$\begin{aligned} G_0^{AA}(\mathbf{r}) \simeq (-1)^{|n_1|+|n_2|+1} \frac{z}{J_z^2}\ j_x^{|n_1|}\ j_y^{|n_2|} \times \left[\sum_{k_1,k_2=0}^{\infty} \binom{|n_1|+k_1+k_2}{|n_1|+k_1} \binom{|n_2|+k_1+k_2}{|n_2|+k_1}\ j_x^{2k_1}\ j_y^{2k_2}\right] \\ \text{for } \mathrm{sgn}(n_1) \neq \mathrm{sgn}(n_2) \end{aligned} \tag{A.20}$$

For $\mathbf{r} = 0$ and for asymptotically small $z$, Eq. (A.16) gives, to leading order in $z$,

$$G_0^{AA}(0) \simeq \frac{-z}{J_z^2\sqrt{(1 - j_x^2 - j_y^2)^2 - 4j_x^2\ j_y^2}} \tag{A.21}$$

# Appendix B

# Effective moment of a single vacancy in the gapless phase and flux free sector

## B.1 $T = 0, \mathbf{h} = (0, 0, h), h \ll J$

In this section we find the change in energy $\mathcal{E}(\mathbf{h})$ of a system with a single vacancy, in the gapless phase, in the flux free sector and at zero temperature, as a function of field. We recall Eq. (4.6) and Eq. (4.10) calculated in section 4.2 and valid for $\mathbf{h} = (0, 0, h)$

$$\mathcal{E}(h) = \frac{1}{2\pi i} \oint \mathcal{E}(z, h) dz \tag{B.1}$$

$$\mathcal{E}(z, h) = h^2 [g(z) - z\partial_z g(z)]/[z - h^2 g(z)] \ . \tag{B.2}$$

For small $h$, the dominant contribution to the integral in Eq. (B.1) will come from the region of small $z$ and we can use the asymptotic form for $g(z)$:

$$\begin{aligned} g(z) \sim & \quad -\frac{\nu^2}{z\lambda(i\pi + 2\ln(\mu z))} \\ -z\partial_z g(z) \sim & \quad g(z) \end{aligned} \tag{B.3}$$

We then find

$$\begin{aligned} \mathcal{E}(h) = & \quad \mathrm{Re}\left[ -\frac{1}{2\pi i} 2 \int_{0-i\epsilon}^{\infty - i\epsilon} \frac{-2h^2\nu^2}{h^2\nu^2 + z^2\lambda(i\pi + 2\ln(\mu z))} dz \right] \\ = & \quad \int_{-\infty}^{\infty} \frac{-2h^2\nu^2\mu\lambda e^{-t}}{(h^2\nu^2\mu^2 e^{-2t} + 2\lambda t)^2 + \lambda^2\pi^2} dt \quad \text{where } \mu z = e^t \end{aligned} \tag{B.4}$$

The dominant contribution to this integral comes from the region around the minimum of the denominator. We define this minimum as $R$, define $t = R + t'$ and expand around

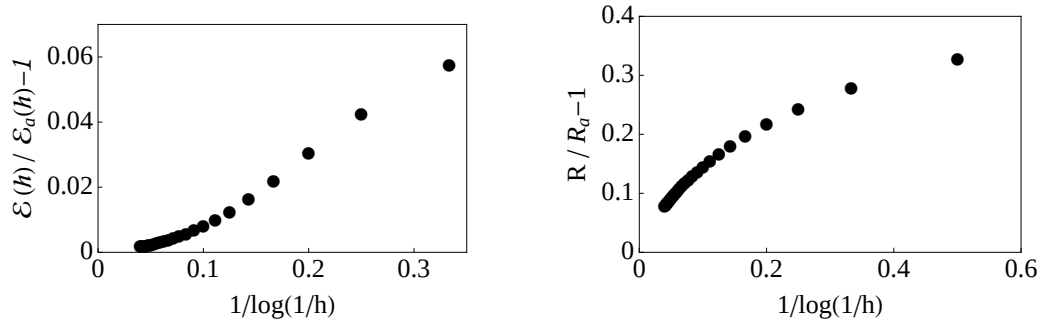



Figure B.1: a) Comparison of the numerical integration of Eq. (B.4) with the asymptotic solution Eq. (B.7). b) Comparison of $R$ with its asymptotic form $R_a$

$t' = 0$. The minimum satisfies $h^2\nu^2\mu^2 e^{-2R} + 2\lambda R = 0$ and has solutions

$$R_n = \frac{1}{2} W_n \left[ -\frac{h^2\mu^2\nu^2}{\lambda} \right] , \tag{B.5}$$

where $W$ is the Lambert W function (sometimes called the Product Logarithm). For real coefficients, there are two real solutions: the principle branch $W_0$ and the branch $W_{-1}$. $\mathcal{E}(h)$ is found by summing over both solutions, however, the solution for $W_{-1}$ is very much greater than that for $W_0$, which we therefore ignore. Hence

$$\mathcal{E}(h) \simeq \int_{-\infty}^{\infty} \frac{-2h^2\nu^2\mu e^{-R_{-1}}}{\lambda(4(1+2R_{-1})^2 t'^2 + \pi^2)} dt' = \frac{h\sqrt{-2R_{-1}}}{(1+2R_{-1})} \sqrt{\frac{\nu^2}{\lambda}} \tag{B.6}$$

For later calculations it will be helpful to define a quantity that is equal to this asymptotic form for $\mathcal{E}(h)$:

$$\mathcal{E}_a(h) \equiv \frac{h\sqrt{-2R_{-1}}}{(1+2R_{-1})} \sqrt{\frac{\nu^2}{\lambda}} \tag{B.7}$$

For small $h$, the leading order term in the series solution to the $W_{-1}$ branch is $R_{-1} \simeq R_a \equiv \frac{1}{2}\ln[h^2\mu^2\nu^2/\lambda]$. In Figure B.1 we analyse the precision of Eq. (B.6) and the asymptotic form for $R_{-1}$ at small $h$. Both are found to be asymptotically exact as $h \to 0$. Finally, the magnetisation $m_z = -\partial_h \mathcal{E}(h)$ is

$$m_z \simeq \sqrt{\frac{\nu^2}{-2R_a\lambda}} = \sqrt{\frac{\nu^2}{\lambda \ln[\lambda/h^2\mu^2\nu^2]}} \simeq \sqrt{\frac{\nu^2}{2\lambda \ln[1/h]}} \tag{B.8}$$

## B.2 Finite $T, \mathbf{h} = (0, 0, h), h \ll J$

We now consider the magnetisation at finite temperature, where the magnetisation is found by taking the derivative of the free energy with respect to $h$ rather than the ground state

energy:

$$\begin{aligned} m(T,h) = &\quad T\partial_h \ln(\mathcal{Z}) = T\partial_h \ln\left[\mathrm{Tr}\,\exp\left(-\frac{1}{T}\sum_{\mathbf{q}} S_{\mathbf{q}}(2a^\dagger_{\mathbf{q}}a_{\mathbf{q}}-1)\right)\right] \\ = &\quad T\partial_h \ln\left[\mathrm{Tr}\prod_{\mathbf{q}}\exp\left(-\frac{S_{\mathbf{q}}}{T}(2a^\dagger_{\mathbf{q}}a_{\mathbf{q}}-1)\right)\right] = T\partial_h \ln\left[\prod_{\mathbf{q}} 2\cosh\left(\frac{S_{\mathbf{q}}}{T}\right)\right] \\ = &\quad \frac{T}{2\pi i}\partial_h \oint \frac{\mathcal{E}(z,h)}{z}\ln\left[2\cosh\left(\frac{z}{T}\right)\right]dz \end{aligned} \tag{B.9}$$

The function $\frac{1}{\pi}\mathrm{Im}[\mathcal{E}(z,h)z^{-1}] = \rho(z,h)$ is the field dependent density of states and has two maxima given by the $0^{\text{th}}$ and $\text{-}1^{\text{th}}$ branch in Eq. (B.5): $R_0$ and $R_{-1}$. Unlike in the $T=0$ case, we must consider both branches in the calculation of $m(T,h)$. We define the energy at which the main contributions to the integral occur as

$$\begin{aligned} z_{-1} = &\quad \frac{e^{-R_{-1}}}{\mu} = \quad h\nu\sqrt{\frac{1}{-2\lambda R_{-1}}} \simeq \qquad h\nu\sqrt{\frac{1}{2\lambda\ln[1/h]}} \\ z_0 = &\quad \frac{e^{-R_0}}{\mu} = \quad h\nu\sqrt{\frac{1}{-2\lambda R_0}} = \quad \frac{\nu}{\sqrt{\nu^2+\lambda^2}}\left(1+O(h^2)\right) \end{aligned} \tag{B.10}$$

### B.2.1 Magnetisation for $z_{-1} \ll T$

In a similar manner to the calculation of $m(h, T=0)$, the integral in Eq. (B.9) may be recast as

$$m(h,T) = -T\partial_h \mathrm{Re}\left[\frac{i}{\pi}\int_{0-i\epsilon}^{\infty-i\epsilon}\frac{\mathcal{E}(z,h)}{z}\ln\left[2\cosh(z/T)\right]dz\right] \tag{B.11}$$

Since $z_{-1} \ll T$ one can approximate $\ln\left[2\cosh(z/T)\right] \simeq \ln[2] + z^2/2T^2$ in this region. This is also a good approximation for the contribution from the region around $z_0$ since the integral

will be cut off at an energy for which $z/T \sim 1$.

$$\mathrm{Re}\left[\frac{i}{\pi}\int_{0-i\epsilon}^{T-i\epsilon}\frac{\mathcal{E}(z,h)}{z}\left(\ln[2]+\frac{z^2}{2T^2}\right)dz\right]=\int_{-\infty}^{\ln(\mu T)}\frac{-2h^2\nu^2\lambda e^{-2t}}{(h^2\nu^2\mu^2e^{-2t}+2\lambda t)^2+\lambda^2\pi^2}\frac{e^{2t}}{2T^2}dt \tag{B.12}$$

$$\simeq\frac{1}{2T^2}\int_{-\infty}^{\infty}\frac{-2h^2\nu^2}{\lambda(4(1+2R_{-1})^2t^2+\pi^2)}dt+\frac{1}{2T^2}\int_{R_{-1}}^{\ln(\mu T)}\frac{-2h^2\nu^2}{\lambda(4(1+2R_0)^2t^2+\pi^2)}dt \tag{B.13}$$

$$\simeq-\frac{h^2\nu^2}{2T^2(1+2R_{-1})\lambda}-\left[\frac{h^2\nu^2}{2T^2\pi(1+2R_0)\lambda}\tan^{-1}\left(\frac{2t(1+2R_0)}{\pi}\right)\right]_{R_{-1}}^{\ln(\mu T)} \tag{B.14}$$

$$=-\frac{h^2\nu^2}{2T^2\lambda}\left[\frac{1}{(1+2R_{-1})}-\frac{1}{(1+2R_0)}\left(\frac{1}{2(1+2R_0)\ln(\mu T)}-\frac{1}{2R_{-1}(1+2R_0)}\right)\right] \tag{B.15}$$

$$\simeq\frac{h^2\nu^2}{4T^2\lambda\ln(\mu T)} \tag{B.16}$$

In the second part of (B.12) we have dropped the constant term ln[2] since an integral over the field dependent density of states must be a constant, independent of $h$ and will not affect the magnetisation: $\int\rho(z,h)dz=$ const. We have also made the substitution $\mu z=e^t$. In (B.16) we have used $(1+2R_0)\simeq 1$ and $|R_{-1}|\gg|\ln(\mu T)|$. The approximate integrand (B.13) is compared with the full integrand $\mathcal{E}(z,h)z^{-1}\left(\ln[2\cosh(z/T)]-\ln[2]\right)$ in Figure B.2.

Thus, for $z_{-1}\ll T$ we find

$$m(h,T)\simeq\frac{h\nu^2}{2T\lambda\ln(1/\mu T)} \tag{B.17}$$

### B.2.2 Magnetisation for $T\ll z_{-1}$

In this parameter regime the integral

$$\mathrm{Re}\left[\frac{i}{\pi}\int_{0-i\epsilon}^{\infty-i\epsilon}\frac{\mathcal{E}(z,h)}{z}\ln\left[2\cosh(z/T)\right]dz\right] \tag{B.18}$$

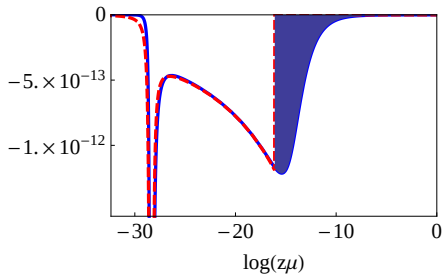



Figure B.2: Plot of $\mathcal{E}(z,h)z^{-1}\ln[\cosh(z/T)]$ - solid blue curve, and the integral (B.13) - dashed red line. Here, $T = \exp(-15)$ and $h = \exp(-25)$ such that $R_{-1} = -28.37$, $R_0 = -6\times10^{-24}$ and $\ln(\mu T) = -16.1$. The dependence of the shaded region on $T$, not accounted for in the approximation Eq. (B.13), gives a higher order correction to the leading order term Eq. (B.16).

may be approximated as

$$\simeq \mathrm{Re}\left[\frac{i}{\pi}\int_{0-i\epsilon}^{\infty-i\epsilon}\frac{\mathcal{E}(z,h)}{z}\left(z/T+e^{-2z/T}\right)dz\right] \tag{B.19}$$

$$= \frac{h\sqrt{-2R_{-1}}}{T(1+2R_{-1})}\sqrt{\frac{\nu^2}{\lambda}} - \int_0^\infty \frac{2h^2\nu^2 z\lambda e^{-2z/T}}{(h^2\nu^2+z^2\lambda 2\ln(\mu z))^2+z^4\lambda^2\pi^2}dz \tag{B.20}$$

$$\simeq \frac{h\sqrt{-2R_{-1}}}{T(1+2R_{-1})}\sqrt{\frac{\nu^2}{\lambda}} - \int_0^\infty \frac{2z\lambda e^{-2z/T}}{h^2\nu^2}dz = \frac{h\sqrt{-2R_{-1}}}{T(1+2R_{-1})}\sqrt{\frac{\nu^2}{\lambda}} - \frac{\lambda T^2}{2h^2\nu^2} \tag{B.21}$$

$$\tag{B.22}$$

Therefore

$$m(h,T) \simeq \sqrt{\frac{\nu^2}{2\lambda\ln[1/h]} - \frac{\lambda T^3}{h^3\nu^2}} \tag{B.23}$$

## B.3 $T = 0, \mathbf{h} = (h_x, h_y, h_z), h \ll J$

We now consider a field in a general orientation and outline the steps necessary for the calculation of $\mathcal{E}(h)$. The defining equation for $\mathcal{E}(z,h)$ is

$$\mathcal{E}(z,h) = z\sum_{\mathbf{r}\neq r_v}\sum_{\mathbf{r}',\mathbf{r}''} G(0,\mathbf{r},\mathbf{r}')T(\mathbf{r}',\mathbf{r}'')G(0,\mathbf{r}'',\mathbf{r}) \tag{B.24}$$

The $T$ matrix is now $6\times6$ and the summation over $\mathbf{r}'$ and $\mathbf{r}''$ is over all six sites $\mathbf{r}_1, \mathbf{r}_2, \mathbf{r}_3, \mathbf{r}_x, \mathbf{r}_y$ and $\mathbf{r}_z$ labelled in Figure B.3. For ease of notation in this section we define $G_{jk} = G(h = 0, r_j, r_k)$. $\mathcal{E}(z,h)$ is now a much more complicated function than that found for a field with a single non-zero component in section B.1. Nevertheless, we will show here that it reduces

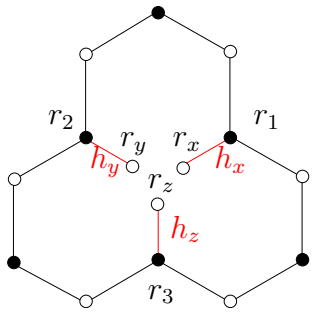



Figure B.3: Reproduction of Figure B.3(c), included here for ease of reference.

in the limit of small $|\mathbf{h}|$ to an analytically tractable expression from which one can calculate the ground state energy as a function of field. $\mathcal{E}(z,h)$ has a numerator:

$$\begin{aligned}
&h_x^2\left(-(G_{11}-G_{12})^2(G_{11}+2G_{12})h_y^2h_z^2+(G_{11}^2-G_{12}^2)(h_y^2+h_z^2)z-G_{11}z^2\right)\\
&+\sum_r -zh_x^2G_{r,r_1}G_{r_1,r}\left((G_{11}^2-G_{12}^2)h_y^2h_z^2-G_{11}(h_h^2+h_z^2)z+z^2\right)\\
&+\sum_r -zh_x^2h_y^2G_{r,r_1}G_{r_2,r}G_{12}\left((G_{12}-G_{11})h_z^2+z\right)\\
&+\sum_r -zh_x^2h_z^2G_{r,r_1}G_{r_3,r}G_{12}\left((G_{12}-G_{11})h_y^2+z\right)\\
&+\text{cyclic permutations}
\end{aligned} \tag{B.25}$$

and denominator

$$(G_{11}-G_{12})^2(G_{11}+2G_{12})h_x^2h_y^2h_z^2-(G_{11}^2-G_{12}^2)(h_x^2h_y^2+h_y^2h_z^2+h_z^2h_x^2)z+G_{11}(h_x^2+h_y^2+h_z^2)z^2-z^3 \tag{B.26}$$

The following identities greatly simplify the above expressions

$$\begin{aligned}
\sum_r G_{r,r_1}G_{r_1,r} &= -\partial_z G_{11} & G_{12} &= G_{13}=G_{23}\\
\sum_r G_{r,r_1}G_{r_2,r} &= -\partial_z G_{12} & \sum_r G_{r,r_1}G_{r_3,r} &= -\partial_z G_{12}
\end{aligned} \tag{B.27}$$

Performing the sum over cyclic permutations, combining the final two lines and using these simplifications, we find that the numerator is:

$$\begin{aligned}
&-3(G_{11}-G_{12})^2(G_{11}+2G_{12})h_x^2h_y^2h_z^2+2(G_{11}^2-G_{12}^2)(h_x^2h_y^2+h_y^2h_z^2+h_z^2h_x^2)z\\
&+z\partial_z G_{11}\left[3(G_{11}^2-G_{12}^2)h_x^2h_y^2h_z^2-2G_{11}(h_x^2h_y^2+h_y^2h_z^2+h_z^2h_x^2)z+(h_x^2+h_y^2+h_z^2)z^2\right]\\
&+2zG_{12}\partial_z G_{12}\left[3(G_{12}-G_{11})h_x^2h_y^2h_z^2+(h_x^2h_y^2+h_y^2h_z^2+h_z^2h_x^2)z\right]-G_{11}(h_x^2+h_y^2+h_z^2)z^2\ .
\end{aligned} \tag{B.28}$$

Collecting together terms that are the same order of magnitude in $\mathbf{h}$, the above is equal to

$$3h_x^2h_y^2h_z^2\left(G_{11}-G_{12}\right)\left(-(G_{11}^2-2G_{12}^2)+\frac{z}{2}\partial_z(G_{11}^2-2G_{12}^2)+G_{12}(-G_{11}+z\partial_zG_{11})\right)$$
$$+2z(h_x^2h_y^2+h_y^2h_z^2+h_z^2h_x^2)\left((G_{11}^2-G_{12}^2)-\frac{z}{2}\partial_z(G_{11}^2-G_{12}^2)\right)-\mathbf{h}.\mathbf{h}z^2\left(G_{11}-z\partial_zG_{11}\right) \tag{B.29}$$

The Green function elements above may be evaluated by using the methods laid out in Appendix A. It can be shown that for small $|\mathbf{h}|\ll 1$ only the O($\mathbf{h}.\mathbf{h}$) pieces from the numerator and denominator contribute and we find

$$\mathcal{E}(z,h)\simeq\mathbf{h}.\mathbf{h}\frac{G_{11}-z\partial_zG_{11}}{z-\mathbf{h}.\mathbf{h}G_{11}}\equiv\mathbf{h}.\mathbf{h}\frac{g(z)-z\partial_zg(z)}{z-\mathbf{h}.\mathbf{h}g(z)}\ , \tag{B.30}$$

where we have made the connection with the function $g(z)\equiv G_{11}$ defined in section 4.2. The magnetisation can then be found by the same method outlined in section B.1.

# Appendix C

# Effective moment of a single vacancy in the gapless phase and ground state flux sector

## C.1 $T = 0, h = (0, 0, h), h \ll J$

As before, we seek $\mathcal{E}(\mathbf{h})$ for $\mathbf{h} = (0, 0, h)$ but now in the ground state flux sector, where fluxes are attached to vacancy plaquettes. In Figure 4.4 we saw that $g(z) \sim i\zeta$, with $\zeta$ a positive constant. For small fields, the magnetisation will be affected only by the low energy degrees of freedom, which are characterised by this functional form for $g(z)$. We therefore introduce a high energy cut off $\Delta = O(J)$ on the allowed energy levels, the choice of which has no effect on $\mathcal{E}(h)$:

$$\begin{aligned}
\mathcal{E}(h) = & \frac{1}{2\pi i}\oint \frac{h^2(g(z) - z\partial_z g(z))}{z - h^2 g(z)} dz \sim \mathrm{Re}\left[\frac{i}{\pi}\int_{0-i\epsilon}^{\Delta - i\epsilon} \frac{h^2 i\zeta}{z - h^2 i\zeta} dz\right] \\
= & \int_0^{\Delta} \frac{-h^2\zeta z}{\pi(z^2 + h^4\zeta^2)} dz = \frac{h^2\zeta}{2\pi}\left(2\log(h^2\zeta) + \log(\Delta^2 + h^4\zeta^2)\right) \\
\simeq & \frac{h^2\zeta \log(h^2\zeta)}{\pi}
\end{aligned} \tag{C.1}$$

The magnetistion is thus

$$m(h) \sim \frac{2h\zeta \log(1/h^2\zeta)}{\pi} \tag{C.2}$$

## C.2 Finite $T, h = (0, 0, h), h \ll J$

Using the results of section B.2, the magnetisation at finite temperature $T$ is given by

$$m(T, h) = T\partial_h \ln(\mathcal{Z}) = T\partial_h \frac{1}{2\pi i}\oint \frac{\mathcal{E}(z, h)}{z} \ln[2\cosh(z/T)] dz \tag{C.3}$$

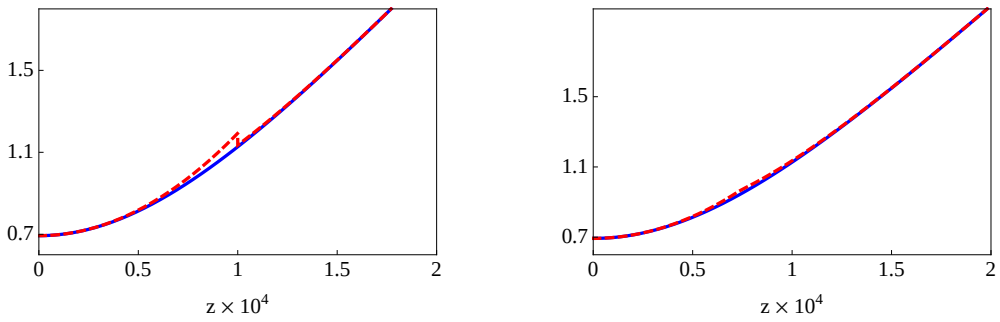



Figure C.1: a) Blue line - $\ln[2\cosh(z/T)]$ for $T = 10^-4$. Red dashed line - $\ln[2] + z^2/2T^2$ for $z < T$ and $z/T + \exp -2z/T$ for $T < z$. b) A better approximation can be made by using a different cross over scale. Lines as for (a) but now with the cross over scale of $0.75T$. This choice does not qualitatively effect the resulting magnetisation.

In Eq. (C.1) one can see that the field sets an energy scale $z_0 \sim h^2\zeta$. In the following calculation of $\ln(\mathcal{Z})$ we separate the integral into a high and low temperature regions, $z/T < 1$ and $1 < z/T$ respectively, and use a series expansion for $\ln[2\cosh(z/T)]$ in each regime. In Figure C.1 we demonstrate that the approximation used is good.

$$\begin{aligned}
\ln[\mathcal{Z}] \sim & \frac{1}{\pi}\int_0^{\Delta} \frac{\zeta h^2}{\zeta^2 h^4 + z^2} \ln[2\cosh(z/T)]dz \\
\simeq & \frac{1}{\pi}\int_0^{T} \frac{\zeta h^2}{\zeta^2 h^4 + z^2}\left(\ln[2] + \frac{z^2}{2T^2}\right)dz + \frac{1}{\pi}\int_T^{\Delta} \frac{\zeta h^2}{\zeta^2 h^4 + z^2}\left(\frac{z}{T} + e^{-2z/T}\right) \\
= & \frac{\ln[2]}{\pi}\left[\tan^{-1}\left(\frac{z}{h^2\zeta}\right)\right]_0^T + \frac{h^2\zeta}{2\pi T^2}\left[z - h^2\zeta\tan^{-1}\left(\tfrac{z}{h^2\zeta}\right)\right]_0^T \\
& + \tfrac{h^2\zeta}{2\pi T}\left[\ln[z^2 - h^4\zeta^2]\right]_T^{\Delta} + \frac{1}{\pi}\int_T^{\Delta} \frac{\zeta h^2}{\zeta^2 h^4 + z^2} e^{-2z/T}
\end{aligned} \tag{C.4}$$

In the high temperature limit, i.e. for $z_0/T = h^2\zeta/T << 1$, we find

$$\begin{aligned}
\ln[\mathcal{Z}] \sim & \frac{h^2\zeta\ln(1/T)}{\pi T} + O\left(\frac{h^2\zeta}{T}\right) + \text{ const} \\
m(T,h) \sim & \frac{2h\zeta\ln(1/T)}{\pi} + O(2h\zeta)
\end{aligned} \tag{C.5}$$

In the low temperature limit, $1 \ll z_0/T = h^2\zeta/T$, we have instead

$$\begin{aligned}
\ln[\mathcal{Z}] \sim & \frac{h^2\zeta\ln(1/h^2\zeta)}{\pi} + O\left(\frac{T}{h^2\zeta}\right) \\
m(T,h) \sim & \frac{2h\zeta\ln(1/h^2\zeta)}{\pi} + O\left(\frac{-T^2}{h^3}\right)
\end{aligned} \tag{C.6}$$

.

# Appendix D

# Calculation of the local density of states on a semi-infinite cylinder

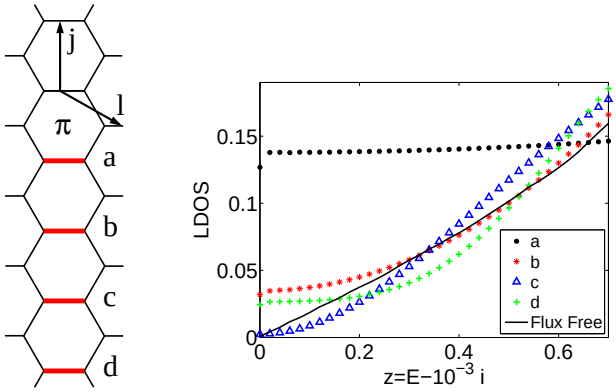



Figure D.1: Reproduction of Figure 4.4, included here for ease of reference. a) The LDOS is evaluated for the sites 'a-d' indicated on an infinite cylinder, periodic in direction **j**, with circumference 1502 lattice units. The flux string, as indicated by thick, red lines, is also in direction **j**. The second flux is taken half way round the cylinder. b) The local density of states. Note that, in particular, the LDOS remains non-zero at site 'a' as $E \to 0$, in the presence of flux. For comparison we include the LDOS for the flux free system.

This appendix provides details of a numerical method for calculating the Green function and hence local density of states for a hexagonal lattice in the presence of a flux. As outlined in chapter 6, it was also our best hope of obtaining an analytic solution to the Green function in the presence of a flux, though our attempts remain unfruitful. The LDOS is related to the Green function evaluated at complex energy $z = E - i\epsilon$:

$$\mathrm{LDOS}(z) = \lim_{\epsilon \to 0} \frac{1}{\pi} \mathrm{Im}\left[G_F^{AA}(\mathbf{r}, \mathbf{r})\right] \tag{D.1}$$

A particularly efficient way of numerically finding $G_F(\mathbf{r},\mathbf{r})$ for a semi-infinite system is by solving the defining Green function equations on two half infinite cylinders and matching at the boundary, where we include the flux string. We define Green functions on the left and right half cylinders as $G^{\alpha\beta}_{F,L}(j,l)$ and $G^{\alpha\beta}_{F,R}(j,l)$ respectively, where the sublattice indices $\alpha$ and $\beta$ are now explicitly included and $(j,l)$ indicate the location of the unit cell as measured from the origin. The unit vectors in directions $\hat{\mathbf{j}}$ and $\hat{\mathbf{l}}$ are shown in Figure D.1(a). For a cylinder of circumference $w$, they have Fourier transforms:

$$G^{\alpha,\beta}_{F,L}(j,l) = \frac{1}{w}\sum_k \widetilde{G}^{\alpha,\beta}_{F,L}(k,l) \qquad G^{\alpha,\beta}_{F,R}(j,l) = \frac{1}{w}\sum_k \widetilde{G}^{\alpha,\beta}_{F,R}(k,l)\ , \tag{D.2}$$

where in this section, the tilde denotes functions in the reciprocal space of $j$. The defining Green function equations on the left and right hand sides (LHS, RHS) are identical

$$\begin{aligned} z\widetilde{G}^{AA}_{F,L(R)}(k,l) - \widetilde{G}^{BA}_{F,L(R)}(k,l) - (1+e^{ik})\widetilde{G}^{BA}_{F,L(R)}(k,l+1) &= 0 \\ z\widetilde{G}^{BA}_{F,L(R)}(k,l) - \widetilde{G}^{AA}_{F,L(R)}(k,l) - (1+e^{-ik})\widetilde{G}^{AA}_{F,L(R)}(k,l-1) &= 0 \end{aligned} \tag{D.3}$$

but have different conditions on the allowed values of $k$ that ensure we find only decaying solutions: the LHS has $|2\cos(k/2)| < 1$ and the RHS has $|2\cos(k/2)| > 1$. The fluxes are introduced at the origin and half way around the cylinder by a function $\eta(j)$, where

$$\eta(j) = \begin{cases} 1 & 0 \le j \le w/2 \\ -1 & w/2+1 \le j \le w-1 \end{cases}\ , \tag{D.4}$$

and the solutions are matched on the boundary, where the Green function satisfies the following coupled equations

$$\begin{aligned} \frac{1}{w}\sum_k e^{ikj}\left[\widetilde{G}^{AA}_{F,R}(k,0) - (1+e^{ik})\widetilde{G}^{BA}_{F,R}(k,1) - \eta(j)\widetilde{G}^{BA}_{F,L}(k,0)\right] &= \delta_{j,0} \\ \frac{1}{w}\sum_k e^{ikj}\left[\widetilde{G}^{BA}_{F,L}(k,0) - (1+e^{-ik})\widetilde{G}^{AA}_{F,L}(k,-1) - \eta(j)\widetilde{G}^{AA}_{F,R}(k,0)\right] &= 0\ . \end{aligned} \tag{D.5}$$

The solution $\widetilde{G}^{\alpha,\beta}_{F,L(R)}(k,l)$ and hence $G^{\alpha,\beta}_{F,L(R)}(j,l)$ can be found numerically by solving Eq. (D.5). If the system has circumference $w = 3L+1$ or $w = 3L+2$ then there are no exact zero energy states and $|2\cos(k/2)| \neq 1$. We therefore find $G^{\alpha,\beta}_{F,L(R)}(j,l)$ for a cylinder with circumference $3L+2$ and show the resultant LDOS for sites close to the origin in Figure D.1(b). The results have converged for a circumference $w = 1502$.

# Bibliography


[1] I Affleck. Quantum spin chains and the Haldane gap. *J. Phys. Condens. Matter*, 1(19):3047, 1989.

[2] I. Affleck, D. Gepner, H. J. Schulz, and T. Ziman. Critical behaviour of spin-s Heisenberg antiferromagnetic chains: analytic and numerical results. *J. Phys. A*, 22(5), 1989.

[3] I. Affleck, T. Kennedy, E. H. Lieb, and H. Tasaki. Rigorous results on valence-bond ground states in antiferromagnets. *Phys. Rev. Lett.*, 59(7):799–802, Aug 1987.

[4] F. Alet and E. S. Sørensen. Magnetization profiles and NMR spectra of doped Haldane chains at finite temperatures. *Phys. Rev. B*, 62(21):14116–14121, Dec 2000.

[5] H. Alloul, J. Bobroff, M. Gabay, and P. J. Hirschfeld. Defects in correlated metals and superconductors. *Rev. Mod. Phys.*, 81(1):45, Jan 2009.

[6] T. Ami, M. K. Crawford, R. L. Harlow, Z. R. Wang, D. C. Johnston, Q. Huang, and R. W. Erwin. Magnetic susceptibility and low-temperature structure of the linear chain cuprate $Sr_2CuO_3$. *Phys. Rev. B*, 51(9):5994–6001, Mar 1995.

[7] P. W. Anderson. The Resonating Valence Bond State in La2CuO4 and Superconductivity. *Science*, 235(4793):1196–1198, 1987.

[8] F. Anfuso and S. Eggert. Knight shifts around vacancies in the 2D Heisenberg model. *Phys. Rev. Lett.*, 96(1):017204, Jan 2006.

[9] H Asakawa and M Susuki. Finite-size corrections in the XXZ model and the Hubbard model with boundary fields. *J. Phys. A*, 29:225, 1996.

[10] A. Auerbach. *Interacting Electrons and Quantum Magnetism*. Springer, 1994.

[11] G. Baskaran, Saptarshi Mandal, and R. Shankar. Exact results for spin dynamics and fractionalization in the Kitaev model. *Phys. Rev. Lett.*, 98(24):247201, Jun 2007.

[12] R. J. Baxter. Spontaneous staggered polarization of the f-model. *J. Stat. Phys.*, 9:145–182, 1973.

[13] H Bethe. Zur theorie der metalle. *Zeitschrift fr Physik A Hadrons and Nuclei*, pages 205–226, 1931.

[14] R. N. Bhatt and P. A. Lee. Scaling studies of highly disordered spin-$\frac{1}{2}$ antiferromagnetic systems. *Phys. Rev. Lett.*, 48(5):344–347, Feb 1982.

[15] C. Bloch. Sur la theéorie des perturbations des états liés. *Nuclear Physics*, 6:329–347, 1958.

[16] N. Bulut, D. Hone, D. J. Scalapino, and E. Y. Loh. Static vacancies on a 2D Heisenberg spin-$\frac{1}{2}$ antiferromagnet. *Phys. Rev. Lett.*, 62(18):2192–2195, May 1989.

[17] L. D. Carr and M. T. Lusk. Defect engineering: Graphene gets designer defects. *Nat. Nano.*, 5:316–317, May 2010.

[18] A. H. Castro Neto, F. Guinea, N. M. R. Peres, K. S. Novoselov, and A. K. Geim. The electronic properties of graphene. *Rev. Mod. Phys.*, 81(1):109–162, Jan 2009.

[19] J. Chaloupka, G. Jackeli, and G. Khaliullin. Kitaev-Heisenberg model on a honeycomb lattice: Possible exotic phases in iridium oxides $A_2IrO_3$. *Phys. Rev. Lett.*, 105(2):027204, Jul 2010.

[20] R. Corless, G. Gonnet, D. Hare, D. Jeffrey, and D. Knuth. On the Lambert W function. *Advances in Computational Mathematics*, 5:329–359, 1996.

[21] K. Damle and S. Sachdev. Spin dynamics and transport in gapped one-dimensional Heisenberg antiferromagnets at nonzero temperatures. *Phys. Rev. B*, 57(14):8307–8339, Apr 1998.

[22] J. Das, A. V. Mahajan, J. Bobroff, H. Alloul, F. Alet, and E. S. Sørensen. Comparison of $S = 1$ and $S = \frac{1}{2}$ impurities in the Haldane chain compound $Y_2BaNiO_5$. *Phys. Rev. B*, 69(14):144404, Apr 2004.

[23] S. Dell'Aringa, E. Ercolessi, G. Morandi, P. Pieri, and M. Roncaglia. Effective actions for spin ladders. *Phys. Rev. Lett.*, 78(12):2457–2460, Mar 1997.

[24] J. des Cloizeaux and J. J. Pearson. Spin-wave spectrum of the antiferromagnetic linear chain. *Phys. Rev.*, 128(5):2131–2135, Dec 1962.

[25] L.-M. Duan, E. Demler, and M. D. Lukin. Controlling spin exchange interactions of ultracold atoms in optical lattices. *Phys. Rev. Lett.*, 91(9):090402, Aug 2003.

[26] S. Eggert and I. Affleck. Impurities in $S = \frac{1}{2}$ Heisenberg antiferromagnetic chains: Consequences for neutron scattering and knight shift. *Phys. Rev. Lett.*, 75(5):934–937, Jul 1995.

[27] S. Eggert, I. Affleck, and M. D. P. Horton. Néel order in doped quasi-one-dimensional antiferromagnets. *Phys. Rev. Lett.*, 89(4):047202, Jul 2002.

[28] S. Eggert, I. Affleck, and M. Takahashi. Susceptibility of the spin-$\frac{1}{2}$ Heisenberg antiferromagnetic chain. *Phys. Rev. Lett.*, 73(2):332–335, Jul 1994.

[29] P. Esquinazi, D. Spemann, R. Höhne, A. Setzer, K.-H. Han, and T. Butz. Induced magnetic ordering by proton irradiation in graphite. *Phys. Rev. Lett.*, 91(22):227201, Nov 2003.

[30] F. H. L. Essler. The supersymmetric $t-J$ model with a boundary. *J. Phys. A*, 29:6183, 1996.

[31] X.-Y. Feng, G.-M. Zhang, and T. Xiang. Topological characterization of quantum phase transitions in a spin-$\frac{1}{2}$ model. *Phys. Rev. Lett.*, 98(8):087204, Feb 2007.

[32] D. S. Fisher. Random antiferromagnetic quantum spin chains. *Phys. Rev. B*, 50(6):3799–3821, Aug 1994.

[33] H. Frahm and A. A. Zvyagin. The open spin chain with impurity: an exact solution. *J. Phys. Condens. Matter*, 9:9939, 1997.

[34] S. Fujimoto. Spinless impurities and Kondo-like behavior in strongly correlated electron systems. *Phys. Rev. B*, 63(2):024406, Dec 2000.

[35] S. Fujimoto and S. Eggert. Boundary susceptibility in the spin-$\frac{1}{2}$ chain: Curie-like behavior without magnetic impurities. *Phys. Rev. Lett.*, 92(3):037206, Jan 2004.

[36] R. Gade. Anderson localization for sublattice models. *Nuclear Physics B*, 398(3):499 – 515, 1993.

[37] M. Gell, D. N. Duhl, and A. F. Giamei. *Superalloys*, chapter - The development of single crystal superalloy turbine blades, pages 205–214. TMS, 1980.

[38] O. Golinelli, Th. Jolicoeur, and R. Lacaze. Finite-lattice extrapolations for a Haldane-gap antiferromagnet. *Phys. Rev. B*, 50(5):3037–3044, Aug 1994.

[39] M. Greven, R. J. Birgeneau, Y. Endoh, M. A. Kastner, B. Keimer, M. Matsuda, G. Shirane, and T. R. Thurston. Spin correlations in the 2D Heisenberg antiferromagnet $Sr_2CuO_2Cl_2$: Neutron scattering, monte carlo simulation, and theory. *Phys. Rev. Lett.*, 72(7):1096–1099, Feb 1994.

[40] M. Greven, R. J. Birgeneau, and U. J. Wiese. Monte carlo study of correlations in quantum spin ladders. *Phys. Rev. Lett.*, 77(9):1865–1868, Aug 1996.

[41] R. B. Griffiths. Magnetization curve at zero temperature for the antiferromagnetic Heisenberg linear chain. *Phys. Rev.*, 133(3A):A768–A775, Feb 1964.

[42] F. D. M. Haldane. Continuum dynamics of the 1-D Heisenberg antiferromagnet: Identification with the O(3) nonlinear sigma model. *Physics Letters A*, 93(9):464 – 468, 1983.

[43] F. D. M. Haldane. Nonlinear field theory of large-spin Heisenberg antiferromagnets: Semiclassically quantized solitons of the one-dimensional easy-axis Néel state. *Phys. Rev. Lett.*, 50(15):1153–1156, Apr 1983.

[44] J. M. Hill, D. C. Johnston, and L. L. Miller. Decomposition of the spin-$\frac{1}{2}$ Heisenberg chain compound $Sr_2CuO_3$ in air and water: An EPR and magnetic susceptibility study of $Sr_2Cu(OH)_6$. *Phys. Rev. B*, 65(13):134428, Mar 2002.

[45] Kaj H. Höglund and Anders W. Sandvik. Impurity effects at finite temperature in the two-dimensional S=$\frac{1}{2}$ Heisenberg antiferromagnet. *Phys. Rev. B*, 70(2):024406, Jul 2004.

[46] Kaj H. Höglund and Anders W. Sandvik. Edge effects in the two-dimensional spin- $\frac{1}{2}$ Heisenberg antiferromagnet. *Phys. Rev. B*, 79(2):020405, Jan 2009.

[47] T Horiguchi. Lattice Green's functions for the triangular and honeycomb lattices. *J. Math. Phys*, 13(9):1411–1419, 1972.

[48] J. Hubbard. Electron Correlations in Narrow Energy Bands. *Proceedings of the Royal Society of London. Series A. Mathematical and Physical Sciences*, 276(1365):238–257, 1963.

[49] G. Jackeli and G. Khaliullin. Mott insulators in the strong spin-orbit coupling limit: From Heisenberg to a quantum compass and Kitaev models. *Phys. Rev. Lett.*, 102(1):017205, Jan 2009.

[50] Y.J. Kim, M. Greven, U.-J. Wiese, and R.J. Birgeneau. Monte Carlo study of correlations in quantum spin chains at non-zero temperature. *Eur. Phys. J. B*, pages 291–297, 1998.

[51] A. Yu. Kitaev. Fault-tolerant quantum computation by anyons. *Annals of Physics*, 303(1):2 – 30, 2003.

[52] A. Yu. Kitaev. Anyons in an exactly solved model and beyond. *Ann. Phys*, 321:2, 2006.

[53] K. M. Kojima, J. Yamanobe, H. Eisaki, S. Uchida, Y. Fudamoto, I. M. Gat, M. I. Larkin, A. Savici, Y. J. Uemura, P. P. Kyriakou, M. T. Rovers, and G. M. Luke. Site-dilution in the quasi-one-dimensional antiferromagnet $Sr_2Cu_{1-x}Pd_xO_3$ : Reduction of Néel temperature and spatial distribution of ordered moment sizes. *Phys. Rev. B*, 70(9):094402, Sep 2004.

[54] C. Lhuillier. Frustrated Quantum Magnets. *ArXiv Condensed Matter e-prints*, February 2005.

[55] E. Lieb, T Schultz, and D. Mattis. Two soluble models of an antiferromagnetic chain. *Annals of Physics*, 16(3):407 – 466, 1961.

[56] E. H. Lieb. Two theorems on the Hubbard model. *Phys. Rev. Lett.*, 62(10):1201–1204, Mar 1989.

[57] E. H. Lieb. Flux phase of the half-filled band. *Phys. Rev. Lett.*, 73:2158–2161, 1994.

[58] A. W. W. Ludwig, M. P. A. Fisher, R. Shankar, and G. Grinstein. Integer quantum hall transition: An alternative approach and exact results. *Phys. Rev. B*, 50(11):7526–7552, Sep 1994.

[59] K. B. Lyons, P. A. Fleury, J. P. Remeika, A. S. Cooper, and T. J. Negran. Dynamics of spin fluctuations in lanthanum cuprate. *Phys. Rev. B*, 37(4):2353–2356, Feb 1988.

[60] E. Majorana. Teoria simmetrica dell'elettrone e del positrone. *Il Nuovo Cimento (1924-1942)*, 14:171, 1937.

[61] B. M. McCoy. Spin correlation functions of the $X-Y$ model. *Phys. Rev.*, 173(2):531–541, Sep 1968.

[62] P. Mendels, X. Labouze, G. Collin, and H. Alloul. 3d antiferromagnetic ordering in cuprates: A Kosterlitz-Thouless transition. *Physica C: Superconductivity*, 185-189(Part 2):1191 – 1192, 1991.

[63] A. Messiah. *Quantum Mechanics*, volume 2. North Holland publishing company, 1965.

[64] A. Micheli, G. K. Brennen, and P. Zoller. A toolbox for lattice-spin models with polar molecules. *Nat. Phys.*, 2(5):1745–2473, 2006.

[65] G. Misguich. Quantum spin liquids. *ArXiv Condensed Matter e-prints*, September 2008.

[66] R. Moessner and S. L. Sondhi. Resonating valence bond phase in the triangular lattice quantum dimer model. *Phys. Rev. Lett.*, 86(9):1881–1884, Feb 2001.

[67] N. Motoyama, H. Eisaki, and S. Uchida. Magnetic susceptibility of ideal spin-$\frac{1}{2}$ Heisenberg antiferromagnetic chain systems, $Sr_2CuO_3$ and $SrCuO_2$. *Phys. Rev. Lett.*, 76(17):3212–3215, Apr 1996.

[68] O. Motrunich, K. Damle, and D. A. Huse. Particle-hole symmetric localization in two dimensions. *Phys. Rev. B*, 65(6):064206, Jan 2002.

[69] C. Nayak, S. H. Simon, A. Stern, M. Freedman, and S. Das Sarma. Non-abelian anyons and topological quantum computation. *Rev. Mod. Phys.*, 80(3):1083–1159, Sep 2008.

[70] K. Nomura and M. Yamada. Thermal bethe-ansatz study of the correlation length of the one-dimensional $S = \frac{1}{2}$ Heisenberg antiferromagnet. *Phys. Rev. B*, 43(10):8217–8223, Apr 1991.

[71] K. S. Novoselov, A. K. Geim, S. V. Morozov, D. Jiang, Y. Zhang, S. V. Dubonos, I. V. Grigorieva, and A. A. Firsov. Electric Field Effect in Atomically Thin Carbon Films. *Science*, 306(5696):666–669, 2004.

[72] J. J. Palacios, J. Fernández-Rossier, and L. Brey. Vacancy-induced magnetism in graphene and graphene ribbons. *Phys. Rev. B*, 77(19):195428, May 2008.

[73] S. H. Pan, E. W. Hudson, K. M. Lang, H. Eisaki, S. Uchida, and J. C. Davis. Imaging the effects of individual zinc impurity atoms on superconductivity in $Bi_2Sr_2CaCu_2O_{8+\delta}$. *Nature*, 403:746–750, 2000.

[74] V. M. Pereira, F. Guinea, J. M. B. Lopes dos Santos, N. M. R. Peres, and A. H. Castro Neto. Disorder induced localized states in graphene. *Phys. Rev. Lett.*, 96:036801, 2006.

[75] Vitor M. Pereira, J. M. B. Lopes dos Santos, and A. H. Castro Neto. Modeling disorder in graphene. *Phys. Rev. B*, 77(11):115109, Mar 2008.

[76] N. M. R. Peres, F. Guinea, and A. H. Castro Neto. Electronic properties of disordered two-dimensional carbon. *Phys. Rev. B*, 73(12):125411, Mar 2006.

[77] A. Ralko, M. Ferrero, F. Becca, D. Ivanov, and F. Mila. Zero-temperature properties of the quantum dimer model on the triangular lattice. *Phys. Rev. B*, 71(22):224109, Jun 2005.

[78] K. S. Raman, R. Moessner, and S. L. Sondhi. SU(2)-invariant spin-$\frac{1}{2}$ Hamiltonians with resonating and other valence bond phases. *Phys. Rev. B*, 72(6):064413, Aug 2005.

[79] D. S. Rokhsar and S. A. Kivelson. Superconductivity and the quantum hard-core dimer gas. *Phys. Rev. Lett.*, 61(20):2376–2379, Nov 1988.

[80] S. Sachdev and M. Vojta. Quantum impurity in an antiferromagnet: Nonlinear sigma model theory. *Phys. Rev. B*, 68(6):064419, Aug 2003.

[81] A. W. Sandvik, E. Dagotto, and D. J. Scalapino. Nonmagnetic impurities in spin-gapped and gapless Heisenberg antiferromagnets. *Phys. Rev. B*, 56(18):11701–11709, Nov 1997.

[82] R. R. P. Singh, M. E. Fisher, and R. Shankar. Spin-$\frac{1}{2}$ antiferromagnetic xxz chain: New results and insights. *Phys. Rev. B*, 39(4):2562–2567, Feb 1989.

[83] J. Sirker, N. Laflorencie, S. Fujimoto, S. Eggert, and I. xs Affleck. Chain breaks and the susceptibility of $Sr_2Cu_{1-x}Pd_xO_{3+\delta}$ and other doped quasi-one-dimensional antiferromagnets. *Phys. Rev. Lett.*, 98(13):137205, Mar 2007.

[84] F. Tedoldi, R. Santachiara, and M. Horvatić. $Y_{89}$ NMR imaging of the staggered magnetization in the doped haldane chain $Y_2BaNi_{1-x}Mg_xO_5$. *Phys. Rev. Lett.*, 83(2):412–415, Jul 1999.

[85] C. C. Tsuei and J. R. Kirtley. Pairing symmetry in cuprate superconductors. *Rev. Mod. Phys.*, 72(4):969, Oct 2000.

[86] X.-G. Wen. Quantum orders and symmetric spin liquids. *Phys. Rev. B*, 65(16):165113, Apr 2002.

[87] F. Wilczek. Majorana returns. *Nat Phys*, 5, Sep 2009.

[88] A. J. Willans, J. T. Chalker, and R. Moessner. To be published.

[89] A. J. Willans, J. T. Chalker, and R. Moessner. Disorder in a quantum spin liquid: Flux binding and local moment formation. *Phys. Rev. Lett.*, 104(23):237203, Jun 2010.

[90] Congjun Wu, Daniel Arovas, and Hsiang-Hsuan Hung. Γ-matrix generalization of the Kitaev model. *Phys. Rev. B*, 79(13):134427, Apr 2009.

[91] S. Yang, S.-J. Gu, C.-P. Sun, and H.-Q. Lin. Fidelity susceptibility and long-range correlation in the Kitaev honeycomb model. *Phys. Rev. A*, 78(1):012304, Jul 2008.

[92] H. Yao and S. A. Kivelson. Exact chiral spin liquid with non-abelian anyons. *Phys. Rev. Lett.*, 99(24):247203, Dec 2007.

[93] H. Yao, S.-C. Zhang, and S. A. Kivelson. Algebraic spin liquid in an exactly solvable spin model. *Phys. Rev. Lett.*, 102(21):217202, May 2009.